THE HYDRAULICS OF NEAR-BOUNDARY FLOW AND SEDIMENT TRANSPORT IN RIVER CHANNELS

Shaghayegh Attar

A Thesis

In the Department

of

Building, Civil and Environmental Engineering

Presented in Partial Fulfillment of the Requirements

For the Degree of

Doctor of Philosophy (Civil Engineering)

Concordia University

Montreal, Quebec, Canada

April 2013

CONCORDIA UNIVERSITY

SCHOOL OF GRADUATE STUDIES

This is to certify that the thesis prepared

By: **Ms. Shaghayegh Attar**

Entitled: **The Hydraulics of Near-boundary Flow and Sediment Transport in River Channels**

and submitted in partial fulfillment of the requirements for the degree of

DOCTOR OF PHILOSOPHY (Civil Engineering)

complies with the regulations of the University and meets the accepted standards with respect to originality and quality.

Signed by the final examining committee:

Dr. Reza Soleymani _____ Chair

Dr. Jueyi Sui _____ External Examiner

Dr. George Vatistas_____ External to Program

Dr. Amruthur Ramamurthy_____ Examiner

Dr. Zhi Chen _____ Examiner

Dr. Samuel Li _____ Thesis Supervisor

Approved by _____
Chair of Department or Graduate Program Director

_____2013 _____
Dean of
Faculty of Engineering and Computer Science

ABSTRACT

The hydraulics of near-boundary flow and sediment transport in river channels

Shaghayegh Attar, Ph.D.
Concordia University, 2013

This research has contributed to an improved understanding of near-bed flow in rivers and the advancement of modelling flow and sediment transport in multiple dimensions. The understanding and prediction of the hydraulic behaviour of river channels are essential to water resources development and river-engineering activity planning. River flow features turbulence and complicated velocity distribution, especially near the bed. An ice cover typically presents in northern rivers during the winter and influences the flow underneath; this further complicates the velocity distribution. The problem of flow near the boundaries (the bed and ice) is notoriously difficult to tackle because of strong velocity shear, multiple length and associated time-scale motions and bed sediment movement. In spite of previous research efforts focusing on the problem, many issues are still unresolved.

This study has resolved the issue with respect to the link between near-bed flow and flow-induced bed shear stress in a computationally efficient manner. The research work consists of (a) derivation of hydraulic parameters necessary for describing and modelling the velocity field and (b) prediction of the bed shear stress τ_b and resultant sediment transport along the riverbed (bedload). In part (a), a large volume of winter observations of water velocity from ice-covered Canadian rivers have been obtained. Assume that the velocity distribution between the bed and ice can be described as a two-layer system. Multi-parameter regression analyses are performed on the observations, yielding a

function with two exponents and one coefficient as hydraulic parameters. These parameters reveal the relative importance of the bed and ice's influence on velocity distribution. The function describes the vertical distribution of velocity. Its practical significance includes convenient estimates of winter discharge, which is expensive and extremely difficult to measure in the field. The observations have also been analysed to produce energy and momentum coefficients. These coefficients are rarely available but are necessary input to one-dimensional flow predictions. Additionally, part (a) includes the development of a mathematical model based on the boundary layer theory and application of it to the bed-influenced layer of ice-covered river flow for determining the drag coefficient. The concept of drag coefficient is widely used to give dynamic condition at the riverbed for predicting flow in three dimensions. Part (b) deals with the key issue of τ_b for bedload computations. An existent multi-layer hydrodynamics model has been extended to explore methods useful to link τ_b to near-bed flow. Such a link will improve computational efficiency. The model is applied to flow over gravel river dunes – a case of complicated velocity distributions. The model results of velocity and τ_b are shown to agree well with acoustic Doppler velocimeter measurements from flume experiments. The predicted τ_b values are used to compute fractional transport rates of non-uniform sediments over the dunes. For bedload modelling, the logarithmic law is shown to provide an appropriate link between near-bed flow and τ_b; this law should be applied to velocities at a wall distance of approximately 300. When using the multi-layer modelling approach, one should allow a minimum of five layers to resolve the velocity structure from the bed to the wall distance.

ACKNOWLEDGMENT

It is with immense gratitude that I acknowledge the continuous support and help of my supervisor, Dr. Samuel Li. His guidance, patience, enthusiasm and his scientific advice in all the time of research are greatly appreciated.

Very special thanks to Dr. A. S. Ramamurthy and Dr. G. Vatistas, members of my advisory committee for their valuable comments and support during the course of my research. Additionally, I would like to thank the other committee members, Dr. Z. Chen and Dr. J. Sui for their time and their advice.

Thanks also to my friends and colleagues for their support and encouragement throughout the hard times of my study.

My deepest gratitude goes to my parents, Monir and Hossein, for their unflagging love and support in every step of my life; they have been my best friends, mentors and supporters and words cannot express my love, respect and appreciation to them. Also, I would like to thank my brother, Shafagh, for being so understanding and caring.

Last, but not least, I would like to thank my husband Mehdi for his understanding and love. His endless support and encouragement was in the end what made this dissertation possible.

CONTRIBUTIONS OF AUTHORS

This doctorate research thesis uses the manuscript-based format. The contributions of authors are clarified in the following:

(1) Chapter 3 is a paper by S. ATTAR and S.S. LI (2012) published in the Canadian Journal of Civil Engineering, Vol. 39, No. 3, pp. 334-338.

Attar has contributed to data analysis, result discussion and the preparation of tables, figures and manuscript text. Li plays the role of supervision and quality control.

(2) Chapter 4 is a paper by S. ATTAR and S.S. LI (2012, in press) to appear in the Journal of River Research and Applications, DOI: 10.1002/rra.2611.

Attar has contributed to data analysis, result discussion and the preparation of tables, figures and manuscript text. Li plays the role of supervision and quality control.

(3) Chapter 5 is a manuscript by S. ATTAR and S. S. LI, which has been submitted to Earth Surface Processes and Landforms in February 2013, Manuscript ID: ESP-13-0045.

Attar has contributed to method development, computational coding and testing, result interpretation and the preparation of tables, figures and manuscript text. Li plays the role of supervision and quality control.

(4) Chapter 6 is a manuscript by S. ATTAR and S. S. LI, which has been submitted to the International Journal of Sediment Research in March 2013, Manuscript ID: IJSRC-S-B-00056.

Attar has contributed to method development, computational coding and testing, result interpretation and preparation of tables, figures and manuscript text. Li plays the role of supervision and quality control.

TABLE OF CONTENT

LIST OF FIGURES

List of Tables

Nomenclature

A	flow area (m^2)	58
A_b	cross-sectional area of the bed above a reference datum (m^2)	32
A_L	constant of bedload unit step in Einstein-type equations	32
A_m	horizontal turbulent momentum mixing coefficient (m^2/s)	87
b	channel width (m)	84
B	top width of ice-covered river cross section (m)	55
	channel width (m)	128
C	constant (= 5.5)	63
C_s	sectionally-averaged sediment concentration	32
	constant ($0.1 < C_s < 0.24$)	88
C_D	drag coefficient	55
d	sediment particle diameter (mm)	28
	distance of a point from the riverbed or ice cover underside (m)	62
D	distance between the riverbed/ice and the point where $u = U_m$ (m)	62
	vertical distance from the reference level (m)	101
d_o	average depth (m)	128
d_{50}	median sediment grain size (mm)	29
d_i	particle diameter of size class i (mm)	34
d_m	average diameter of bed material or $\Sigma\ p_i\ d_i$ (mm)	34
d_t	water depth at the dune trough (m)	128
D_i	grain size of the i'th fraction (mm)	126
D_{sm}	mean grain size of the sediment mixture (mm)	126
f	log of streamwise velocity or $\ln(v)$	44
F_i	horizontal mixing term (m/s^2)	87
	volume percentage of each fraction	126
F_r	Froude number	85
F_s	volume percentage of sands of the sediment mixture	126
g	gravitational acceleration (m/s^2)	34
h	average depth of flow (m)	84
H	mean depth of ice-covered river cross section (m)	55
	average depth of grid element (m)	89
h_b	distance between the riverbed and ice-cover underside (m)	60
h_i	thickness of the ice cover (m)	60
IM	x-direction grid dimension	129

i_b	fraction of bed materials of given grain size	32
i_s	fraction of bedload of given grain size	32
JM	y-direction grid dimension	129
k_o	parameter related to per-unit width discharge q	42
k_s	average roughness height (m)	94
K_1	constant of sediment grain area	32
K_2	constant of sediment particle volume	32
K_3	constant of time scale	32
Kb	z-direction grid dimension	129
K_m	vertical turbulent momentum mixing coefficient (m^2/s)	87
L	turbulence macro-scale (m)	87
L'_{st}	normalised length of the separation streamline	123
m_b	parameter associated with riverbed friction	42
m_i	parameter associated with ice friction	42
N	number of size fractions	34
P	pressure (N/m^2)	61
p_i	percentage of size class i of bed materials	34
P_r	probability of erosion	32
q	water discharge per unit width ($m^3/s.m$)	28
Q	water discharge (m^3/s)	55
$q^{\cdot}$	flow rate in weight per unit time and width (kg/s/m)	29
$q^{\cdot}{}_s$	bed load rate in weight per unit time and width (kg/s/m)	29
q_b	bedload rate for non-uniform materials (fractions)	34
q_{bi}	volumetric fractional transport rate per unit width of channel ($m^3/s/m$)	126
q_{cr}	discharge at incipient motion ($m^3/s/m$)	29
q_s	volume amount of bed load per unit width ($m^3/s/m$)	27
Q_s	volumetric sediment discharge (m3/s)	32
Re	Reynolds number	41
R_h	hydraulic radius (m)	29
s	specific weight of sediment (= 2.65)	126
S	channel slope	28
s_0,s_1,s_2,s_3	coefficients	123
s_o	channel bed slope	129
S_{ij}	mean flow strain rate (s^{-1})	88
S_m	stability function	87

$S(x)$	separation streamline	123
t	time (s)	87
T	simulation time period (s)	129
t_r	ramping period (s)	129
u	streamwise flow velocity (m/s)	58
U	cross-sectionally averaged streamwise velocity (m/s)	58
u_*	friction velocity (m/s)	96
u_b	instantaneous velocity (m/s)	28
	streamwise velocity of the layer nearest a solid boundary (m/s)	63
u_{bi}	velocity components nearest the dune surface (i = 1,2,3) (m/s)	88
u_i	velocity component in the x_i direction (x_1, x_2, x_3) (m/s)	87
u_n	point velocity at an elementary area's centre (m/s)	59
u_t	velocity component tangential to the dune surface (m/s)	95
U_m	maximum velocity (m/s)	60
U_o	free-stream velocity (m/s)	95
$\bar{u}$	layer-averaged velocity (m/s)	90
$\overline{U}$	depth-average velocity (m/s)	90
v	streamwise flow velocity (m/s)	40
V	cross-sectionally averaged velocity (m/s)	41
v_s	velocity of sediment layer in duBoys equations (m/s)	27
v_τ	friction velocity defined as $(\tau_b/\rho)^{1/2}$ (m/s)	62
w	vertical component of the Reynolds-averaged velocity (m/s)	61
w_i^*	fractional transport function	123
x_1	intermediate variable or ln (y/Y)	44
x_2	intermediate variable or ln(1-y/Y)	44
x_1,x_2,x_3	Cartesian coordinates, the same as (x, y, z)	87
x_d	detachment point	123
x_{rt}	reattachment point	123
y	vertical distance from the ice underside (m)	42
	normal distance from the surface (m)	95
Y	total depth of flow (m)	42
y^+	wall distance	94
y_n	normal distance to the bed (m)	123
z_o	parameter related to roughness elements (m)	89

Greek

α	leeside angle of a dune (degree)	80
	energy coefficient	55
α_{rt}	slope of the separation streamline (degree)	123
β	momentum coefficient	55
β_o	log of roughness height or $\ln(k_o)$	44
β_1	reciprocal of a parameter associated with ice fractional effect or $1/m_i$	44
β_2	reciprocal of a parameter associated with bed fractional effect or $1/m_b$	44
χ	characteristic sediment coefficient ($m^6/N^2.s$)	27
χ"	new characteristic sediment coefficient ($m^6/N^2.s$)	28
δ	dune height (m)	80
Δ	grid size in the horizontal (m)	88
ΔA_n	flow area of n'th elementary area (m^2)	59
Δh_b	bottom layer thickness (m)	89
Δx	x-direction grid resolution (m)	129
Δy	y-direction grid resolution (m)	129
Δy_i	width of the elementary area (m)	60
Δz	layer thickness (m)	129
Δz_i	height of the elementary area (m)	58
ε	layer thickness in duBoys-type equations (m)	27
	error element	44
	intermediate variable or U_m/U-1	61
ϕ	ratio of the bed shear stress to the reference shear stress	123
Φ_*	intensity of bedload transport	32
γ	specific weight of water (N/m^3)	28
γ_s	specific weight of sediment (N/m^3)	28
η	length scale of turbulence near the riverbed (m)	76
	water surface level (m)	88
κ	von Karman constant (= 0.41)	63
λ	dune length (m)	80
μ	bed form factor	34
ν	kinematic viscosity of water (m^2/s)	41
ν_T	eddy viscosity (m^2/s)	62
θ	Shields parameter	85
θ_{cr}	critical mobility parameter based on the averaged diameter (d_m)	34

θ_i	mobility parameter of size class i	34
ρ	density of water (kg/m^3)	32
	bed porosity	32
ρ_s	density of sediments (kg/m^3)	32
σ	sigma coordinate or $(x_3 - \eta)/(H + \eta)$	89
τ_b	bed shear stress (N/m^2)	27
τ_{bi}	bed shear stress in the x_i direction (i = 1, 2, 3) (N/m^2)	88
τ_c	critical shear stress (N/m^2)	27
τ_{ri}	reference shear stress of i'th sediment fraction (N/m^2)	126
τ_{rm}	reference shear stress for the mean grain size (N/m^2)	126
τ^*_{rm}	dimensionless reference shear stress	126
τ_{xx}	specific Reynolds shear stress (N/m^2)	61
τ_{xz}	specific Reynolds shear stress (N/m^2)	61
ω	fall velocity (m/s)	32
ξ	normalised distance away from detachment point	123
ξ_i	correction parameter of size class i	34
Ψ	flow intensity	32

Chapter 1

Introduction

1.1 Background

There is a redundancy of rivers in Canada and many other countries. River flows are important for many reasons: They supply drinking water; they are habitats for many aquatic species and organisms on the earth; they support waterway transportation; they provide agricultural irrigation. On the other hand, river flows can cause such problems as flooding and pollutant spreading, with potentially disastrous consequences. River research and applications have attracted attention from researchers and practising engineers for a long period of time. Among the most important and challenging topics are physical processes that govern turbulent flow and the transport of bed sediments in river channels.

Some of the issues related to sediment transport are highlighted below. Sediment deposition can reduce the capacity and life span of reservoirs in a river-reservoir system. Over time, sediments extend upstream and immerse the surrounding lands, while the flowing water, with sediments lost in the reservoir, erodes downstream channels. These processes will significantly reduce the efficiency of reservoirs in terms of flood control, power generation and sediment detention (Wu, 2008). Floods have been one of the most significant disasters that rivers can cause. They often have undesirable, serious consequences on public safety, the aquatic environment and economic well-being.

Sediment transport in river channels and associated bed erosion due to floods or high flow are a great concern. Bed erosion can undermine hydraulic structures such as bridge piers, weirs and river dykes. In fact, erosion has been one of the most common causes of bridge failures (Richardson and Davis, 2001). Impediment to ship navigation is another common problem associated with sediment transport. In many cases, it is necessary to dredge to maintain navigation channels. Thus, it is important to study river flow and interconnected sediment transport, and more importantly to develop the capacity to predict flow and sediment behaviour.

River flow and sediment transport are among the most complex and least understood processes in nature (Wu, 2008). The problem of turbulent river flow and sediment transport is even more complicated when rivers are covered with ice. As is the case in Canada and other northern countries, almost all the rivers are covered with ice during the winter time. This condition makes it more difficult for river researchers and engineers to obtain reliable estimates of sediment transport rate. Such estimates are essential to effective reservoir operation and management, proper channel maintenance, and efficient

functioning of control-structures. For examples, river ice can cause a blockage of inlets to power station cooling systems (Wadhams, 2002), damage to river engineering structures, ice jams (Beltaos, 2001; Prowse, 1990) and river floods (Calkins, 1986).

From the hydraulic point of view, the presence of ice in rivers inevitably causes significant changes to the flow field; it alters velocity profiles, shear stress distributions and turbulent mixing characteristics. In alluvial rivers, the bed is usually covered by bed forms (three-dimensional, highly irregular bed surface features), and there is a complex interaction between flow properties and bed sediments (Best, 1993; Muller and Gyr, 1986). The effects of ice will make this interaction even more complicated (Lau and Krishnappan, 1985); resultant radical changes in bed shear stress will alter the rate of bedload transport (sediment transport over the channel bed).

In summary, the problem of turbulent flow and sediment transport in rivers is poorly understood. There is an urgent need to improve the understanding of the interaction between the lowing water and bed sediments, and to further develop analysis and modelling tools that are useful for quantifying river sediment transport and resultant morphological changes. This need has motivated the present doctoral thesis investigation.

1.2 Objectives

This doctorate thesis focuses on the structure of flow in rivers under open water and ice-covered conditions, the link between near-bed flow and bed shear stress, and the transport of bed sediments driven by the bed shear stress. The specific objectives are:

1) to improve the understanding and predictions of the vertical structure of flow velocity in river channels through a combination of analysing flow observations

from ice-covered river channels and efficient numerical modelling of flow over gravel dunes in river channels.

2) to investigate the parameterisation of flow structure in order to enable simplified numerical modelling of turbulent river flow. The parameterisation covers the case of modelling ice-covered river flows in one and more dimensions and the case of flow separation associated with dunes in river channels.
3) to explore appropriate methods for predicting the bed shear stress from near-bed flow structures, with verification for the case of ice-covered rivers and the case of flow over gravel dunes in river channels.
4) to develop modelling techniques for predicting sediment transport along the riverbed (bedload) over gravel dunes in river channels.

These objectives have been formulated based on a review of the literature about turbulent river flow and sediment transport in rivers. Details about the review are given in Chapter Two. The achievement of the objectives mentioned above will contribute to an improved understanding of near-bed flow hydraulics and the advancement of modelling river flow and sediments in multiple dimensions.

1.3 Scope of the work

This doctorate research has the fundamental aim of advancing our understanding of the dynamics in the loose boundary layer of an alluvial river channel. Its importance and relevance to river engineering and management have been highlighted in this introductory chapter. Also, four specific objectives to be reached have been established. The remaining parts of this thesis consist of six chapters, each providing details about subtasks to be performed and methodologies to be used in order to reach the objectives. The contents to follow provide a description of each chapter and serves as bridging text between chapters.

Chapter 2 provides a comprehensive review of the literature about river flows under open water and ice-covered conditions as well as the transport of sediments in open channels. The review covers data acquisition and analysis, theoretical formulations, modelling techniques and strategies for result verification. This chapter begins with discussion about the velocity structure of river flow followed by the parameterisation of the velocity structure for simplified numerical predictions of turbulent river flow. Attention is given to the simple condition of a fixed channel bed. Then discussion is given to the predictions of bed shear stress from near-bed velocity structure over the complex condition of bed features. Finally, attention is given to sandy bedforms and then gravel bedforms.

In addition, the comprehensive review in Chapter 2 covers the predictions of bed sediment transport driven by bed shear stress. Comments about the advantages and disadvantages of classical bedload formula are provided. More importantly, discussion is given to the transport of uniform sediments and a sediment mixture of different grain

sizes, and to the effects of complexity in terms of bed geometry (a flat bed vs. wavy bedforms) on sediment transport. The main purpose of Chapter 2 is to relate this doctorate research to the previous studies on river flows and sediment transport.

Chapter 3 describes the subtasks to be performed, along with appropriate methodologies, in order to derive an analytical function for the vertical structure of ice-covered river flow velocity. This is part of objective 1 listed in Section 1.2. It is reasonable to assume that the distribution has a two-layer structure. Such a structure can be described by a function containing three parameters: two exponents and one coefficient. The independent variable of the function is the vertical distance from the channel bed. Physically, these exponents represent the frictional effects of ice and the river bed, whereas the coefficient is related to per unit width of discharge. One appropriate way to determine the function is a multi-parameter regression analysis. To ensure relevance, the analysis must be based on field measurements. For this reason, a large volume of winter measurements of flow velocity from Canadian rivers covered by ice has been obtained. The overall mean values for the three parameters can be determined, which allow us to propose a new velocity profile function useful for ice-covered rivers under conditions similar to the Canadian rivers.

Chapter 3 is also intended to discuss the advantages of the newly derived function, including its simplicity in comparison to the logarithmic law of the wall, continuity and differentiability between ice and the river bed. It can be argued that since field measurements of water velocity from ice-covered rivers are extremely difficult and expensive to make, the function is a good alternative for different purposes, including

estimates of winter discharge in ungauged ice-covered rivers, and estimates of bed shear stress in numerical models for ice-covered river hydraulics.

Depending on their applications, modelling studies for ice-covered rivers may be intended to provide cross-sectionally averaged (or one-dimensional) flow field, depth-averaged (or two-dimensional) flow field or distributed (or three-dimensional) flow field. Accordingly, Chapter 4 introduces three hydraulic parameters: the energy correction coefficient α, the momentum correction coefficient β, and the drag coefficient c_D. The coefficients α and β are needed in one-dimensional modelling of river flow on the basis of the energy and momentum principles, respectively, whereas the coefficient c_D is useful for two- and three-dimensional modelling. The coefficients α and β are to be determined using the same winter measurements of flow velocity from Canadian rivers as in Chapter 3. We shall follow the definitions of α and β given in standard hydraulics texts, and assess the empirical relationships for the coefficients suggested by Chow (1959). It will be interesting to investigate variations in α and β over the winter season as well as their seasonal averages and to bring up to date the literature values for the two coefficients.

With regards to the determination of the drag coefficient c_D, two different approaches will be considered in Chapter 4: One is based on the turbulent boundary layer theory, and the other is the quadratic law for friction. The boundary layer theory ought to be applied to the lower layer of the two-layer structure that has been dealt with in Chapter 3. The quadratic drag law approach needs to use near-bed streamwise flow velocities as input. The drag coefficient may be used to parameterise the frictional effects of the ice underside and the river bed on river flow in hydrodynamic - morphological modelling for rivers. Objective 2 (the first case) as listed in Section 1.2 will be reached by completing

the tasks described in Chapter 4. In addition, this chapter will present the results of bed shear stress and associated turbulence length scale in the boundary layer as determined from the velocity measurements and explain the implications of distributed bed shear stresses in modelling river hydraulics using the multi-layer approach. Objective 3 (the first case) listed in Section 1.2 will be achieved.

Chapter 5 serves to exemplify the use of a three-dimensional hydrodynamics model to accomplish Objectives 1 and 3 listed in Section 1.2, with regard to predictions of the flow structure and bed shear stress over gravel dunes. This chapter has two main purposes. The first purpose is to obtain predictions of near-bed flow over fixed dunes and verify the predictions by comparing them with and available laboratory measurements. The second purpose is to establish a link between near-bed flow and bed shear stress useful for bedload calculation.

In Chapter 5, an existing 3-D hydrodynamics model (ECOMSED) is to be extended to obtain predictions of the bed shear stress along the dune wavelength. The extension involves the development of an appropriate approach to bed shear stress estimations, meaning theoretical formulations, coding and validation. Validation strategies include comparisons of model results with the acoustic Doppler velocimeter measurements of three-dimensional flow velocity and turbulent shear stress over periodic gravel dunes. It is important to use hydraulic and geometric conditions in the model consistent with the laboratory experiments. Chapter 5 will demonstrate the advantages of the multi-layer approach to quantify the link between near-bed flow and bed shear stress. The use of σ-layers transforms the wavy dune surface and free surface into coordinate planes. The link will be used to obtain reliable estimates of bed shear stress. This treatment maintains high

computational efficiency in numerical modelling of sediment transport and morphological change.

The longitudinal development of flow over a large number of consecutive dunes using relatively coarse grids will be demonstrated in Chapter 5. The results are dynamic equilibrium solutions for given hydraulic conditions and dune geometry. The results from Chapter 5 provide boundary conditions for flow and bedload modelling in Chapter 6. Chapter 6 will focus on detailed distributions of near-bed flow over the dune length using fine grids and fractional transport rates for a sediment mixture of sands and gravel over dunes.

Chapter 6 has two main purposes. The first is to complete objective 2 listed in Section 1.2, in association with the parameterisation of eddy motions within the flow separation zone expected in the leeside of dunes. The suitability of previously proposed formulations will be assessed. The modelling strategy with flow separation parameterisation is not only suitable for applications to field conditions but also effective to avoid uncertainties associated with complicated turbulent modelling techniques. This strategy along with refined grid resolutions for a shortened model channel will reduce computational efforts and improve efficiency.

The second purpose of Chapter 6 is to predict fractional bedload transport rates for a sediment mixture of sands and gravel using surface-based techniques. A sediment mixture of sands with grain sizes in the range of 0.25 to less than 2 mm and gravel with grain sizes in the range of 2 to 10 mm will be used. With these bedload predictions, we accomplish objective 4 listed in Section 2.1. The bed shear stress over dunes will be determined using the link between near-bed flow and bed shear stress obtained in Chapter

5. For bedload predictions, we will consider three different flow discharges in the channel and compare the predicted transport rates.

Chapter 2

Literature review

This chapter provides a comprehensive review of the literature about

(1) velocity structures of turbulent flow in rivers,

(2) field methods for river flow,

(3) numerical modelling of river flow,

(4) near-bed flow and bedforms in river channels,

(5) bed shear stress and sediment bedload transport.

Listed above are the interconnected contents of the entire thesis and research program. Since this thesis uses the manuscript-based format, additional review of the literature about specific aspects of the flow and bedload problem is covered in the introduction of Chapters 3 to 6.

2.1 Velocity structure of ice-covered river flow

Flow velocity in natural rivers varies in time and space. In general, the spatial variations are the most significant near solid boundaries like the channel bed and sidewalls. In the context of Canadian rivers, an ice cover typically presents in the rivers during the winter time; it causes significant changes to the velocity structure of water flow beneath the solid boundary.

The river-ice process can be divided into three phases: 1) ice-cover formation, 2) ice-cover growth, and 3) ice-cover removal. River ice can form in two types: border ice and frazil ice (Brayall, 2011). Border ice usually forms in slow flow rivers where turbulence is low in the water column. It grows horizontally out from the riverbanks and can cover the entire water surface. Its thickness increases with decreasing air temperature. Frazil ice is small ice particles with shapes of small discs or needles. They mainly form in fast flow rivers with high turbulence. These small particles are in suspension but can easily adhere to each other and rise to the water surface (frazil pans). In the field, various ice cover combinations have been observed (Ashton, 1986) under the local conditions river channel geometry and flow velocity.

Along with border ice, frazil ice increases surface ice thickness, and growth continues during the freeze-up. The presence of an ice cover on the top of the water-surface layer in a channel approximately doubles the wetted perimeter of the channel, increases the depth of flow and reduces the depth-averaged flow velocity (Sayre and Song, 1979; Lau and Krishnappan, 1981). The equivalent ice-covered flows have a larger flow depth than open-channel flows by about 15-30% (Lau and Krishnappan, 1981).

In the spring, when air temperature gradually increases above zero, ice cover begins to impair and the third phase initiates. The breakup can be thermal, when air temperature rises gradually, or dynamic, when ice sheets break into fractions due to a rise in water level. These fractions can run with water and accumulate into an ice jam, which is perhaps the most troublesome river ice problem. More details about the river ice process and ice jam formation can be found in Ashton (1979, 1986) and Shen (2003).

In open river channels with a flat bed, the vertical structure of flow velocity is thought to follow the logarithmic law or power law. In ice-covered rivers, however, the logarithmic law is not valid through the whole depth of flow (Lau and Krishnappan, 1981). Observations show that velocity profiles followed the logarithmic law for about 60% of the flow depth and the application of this law to ice-covered rivers led to overestimates of velocity near the location of velocity maximum (Lau, 1982). It is important to note that in both Lau and Krishnappan (1981) and Lau (1982), observations used are from simplified laboratory experiments of ice-covered channel flow. In nature, ice-covered rivers are much more complicated in terms of ice condition, channel geometry and velocity distribution.

Conventionally, the vertical structure of flow velocity in ice-covered rivers is described by the two-power law (Larsen, 1969; Uzuner, 1975). The law appears to fit experimental data of flow velocity reasonably well under simple geometric conditions (Sayre and Song, 1979; Teal et al., 1994), but it is inadequate for describing ice-covered bend flows with an ice jam formed in a curved flume (Urroz and Ettema, 1994).

2.2 Measured methods of ice-covered river flow

Discharge in river channels is a fundamental variable, and various methods for determining it have been developed. Making detailed measurements of flow velocity at a river section of interest will give the most reliable results. However, this is costly and difficult especially in the case of ice-covered rivers. To reduce measurement efforts, the so-called two-point velocity method has been used as the standard procedures for stream gauging of ice-covered flows. This method estimates the depth-average velocity in a stream-section vertical as the average of the point velocities located at 20% and 80% of the flow depth below the ice cover underside instead of using the whole profile.

Although the velocities at 20% and 80% of the flow depth may deviate significantly from the overall average velocity but the average of these two velocities is very close to the actual depth-averaged velocity, the difference being about 2% (Lau, 1982). The accuracy of two point-velocity measurements was confirmed by generating velocity profiles numerically using two-power law, and the existing error of 2% can be reduced by introducing a coefficient of 0.98 (Teal et al., 1994).

The two-point method was disputed by Walker (1994) on the basis of field measurements from 13 stations located across the United States. Walker (1994) examined the validity of different methods for calculating discharge in ice-covered rivers through the large volume of winter measurement of flow velocity. Inaccuracy of the two-point method was mainly due to the strong effect of ice roughness on the velocity measured at the upper position. Walker (1994) suggested single-point method by measuring point velocity at 50% of the flow depth. Traditionally, using the single-point method, the

depth-averaged velocity is calculated by multiplying the point velocity at 50% or 60% of the flow depth (D) below the ice-cover underside by a coefficient.

A value of 0.88 for the coefficient has widely been used to convert 50% D point-velocity to depth-averaged velocity (Rantz 1982). However, adjustment coefficients should be established for each station (Walker, 1994; Walker and Wang, 1997), resulting in nearly unbiased discharge measurements across the stream flow-gauging network.

The so-called velocity index method was developed for calculating discharge from single-point field measurements of the maximum velocity at a given ice-covered river section, as discussed in Healy and Hicks (2004). This is a relationship between cross-sectionally-averaged velocity and maximum point-velocity of the cross-section. By measuring the maximum velocity at a single point, one determines the average velocity using the derived relationship. The problem is a lack of prior knowledge about the location of the maximum velocity. In Morse et al. (2005), a systematic comparison among various velocity index formulations has identified their limitations and uncertainties for discharge calculations, and with respect to the maximum-velocity location, the central part of the ice-covered river section in question has been recommended.

2.3 Numerical modeling of velocity structures

Depth-averaged flow models for river applications are relatively simple to use and require less data for input and verification, but they provide no information about the vertical structure of flow velocity. Moreover, classical depth-averaged models can encounter difficulties in handling non-hydrostatic pressure (Steffler and Jin, 1993). An

improvement from depth-averaged models has been made by using the so-called multi-layer modelling techniques, in which the whole flow field is divided into a number of streamwise flow layers under the assumption that the vertical distributions of flow quantities within each of the layers are nearly uniform.

Lai and Yen's (1993) classical multi-layer model solved the Reynolds_averaged equations for each layer directly. Like the previous classical multi-layer models, it was assumed that the vertical distributions of flow quantities within a layer are nearly uniform. The classical multi-layer modelling has been improved by using multi-layer averaged momentum equations containing both effective stress and Boussinesq terms (Xia and Jin, 2006). The multi-layer averaged momentum models in Xia and Jin (2006, 2007) were limited to consideration of one dimension and a straight open channel with a fixed bed. Interestingly, the models give velocity and pressure distributions within individual layers. Although the models have produced results in good agreement with flume data for overfall flow, they are inadequate for simulating flow over bedforms.

Moreover, there is an issue with respect to the determination of the water surface elevation and the thickness of each layer in a multi-layer model. The way to determine them affects the accuracy of flow predictions. Some researchers (Morvan *et al*., 2002; Nicholas and Smith, 1999) have suggested the use of a rigid lid as an approximation for the water surface, as summarised in Rameshwaran and Naden (2004) and Demuren (1993). The rig lid approximation is not valid in the consideration of open channel flow on the reach scale. With respect to layer thickness, the interfaces between adjacent layers throughout the entire water column except the top layer were explicitly predetermined in Xia and Jin (2006). An improvement was proposed in Xia and Jin (2007) by allowing the

interfaces to be defined implicitly and their locations to change in space and time for unsteady flow. Under steady flow conditions, the interfaces are consistent with streamlines, the net mass exchanges at all interfaces become zero, and the governing equations are reduced to the classical depth-averaged equations. A direct approach was proposed by Rameshwaran and Naden (2004) who accounted for the water surface elevation by stretching or compressing the vertical mesh based on the pressure distribution at the free surface. The advantage is that the water surface elevation can be simulated without introducing and solving additional equations, making it easier to be incorporated into general CFD code.

Natural river channels have complicated geometry. Predictions of turbulent free-surface flow in a meandering channel were reported in Rameshwaran and Naden (2004). In their study, turbulent fluctuations are treated using the k-ε model, and the governing equations are solved numerically using finite-volume techniques. They concluded that the simulated bed shear stress is sensitive to how the water surface is treated when it varies spatially.

A number of different treatments of the water surface have been discussed in the literature: assumed planner surface (PS), free surface treatment (FST), and the porosity method (PM). In the PM method, the water surface is accounted for by changing the discharge through the layer of surface cells according to the deviation of the pressure on the fixed lid. The PS and FST methods are a direct approach in which the water surface elevation is calculated based on pressure distribution at the surface.

In Rameshwaran and Naden (2004), the measured streamwise velocity contours were shown to be distorted near the free surface with the maximum velocity below the free

surface, the simulations did not capture that features. Perhaps there is a need to use more sophisticated turbulence closure schemes in order to capture the anisotropy effect of turbulence associated with secondary flow in meandering channels. Using a three-dimensional time-averaged CFD model, Ferguson *et al*. (2003) investigated the connection of recirculation eddies with the downstream flow in a meandering channel.

All the modelling studies described above have ignored sediment transport. An additional review of the literature about flow modelling is covered in the introduction of Chapters 4 and 6.

2.4 Near-bed flow and its interaction with bed sediment

When the applied shear stresses at the riverbank and riverbed exceed certain threshold values, the bank and bed sediments may begin to move; the transport of sediments results in different bedforms and river channel shapes. Such a river channel is referred to as an alluvial river channel. Reliable predictions of the bed shear stress are the key to successful calculations of sediment transport in a river channel.

A numerical study by Lau and Krishnappan (1981) compared free-surface and ice-covered flows in terms of the bed shear stress and turbulent eddy viscosity. The conclusion is that the equivalent ice-covered flows have a smaller bed shear stress and a smaller eddy viscosity than free surface flows. This conclusion is supported by an experimental study (Lau and Krishnappan, 1985) of the effects of an ice cover on the dynamics of flow and sediment transport. The experimental data covers bedform, frictional characteristics and sediment transport for equivalent free-surface and ice-covered flows; the data indicates that (a) sediment transport rates in the presence of a

floating cover are much smaller than the free-surface flow values even though the changes in the friction velocity are not large, and (b) although the changes in transport rate are large, for the same discharge and bed slope, the presence of a top cover does not have a significant effect on the bed form characteristics.

Using a 2-D model, Yoon et al. (1996) simulated the flow in a dune-bed channel with a free-floating ice cover and investigated how the growth of ice during the winter affects the principal hydraulic parameters of an open channel. There is a 16% increase of the mean flow depth in comparison to open channel flow, and the flow near the dune bed remains unchanged with the presence of the ice cover. Reportedly, the model results are consistent with experimental data.

Ice covers were shown to increase the dune length and decrease the dune steepness in Smith and Ettema (1997). This is in contrary to the observations made by Lau and Krishnappan (1985) and Yoon et al. (1996). There is a very complex interaction between turbulent boundary layer structure and bed sediments, resulting in different bedforms in rivers. The most common bedforms in alluvial rivers are ripples and dunes. They have significant effects on the flow field, sediment flux and the bed morphology (Best, 1993; Muller and Gyr, 1986).

2.4.1 General features of bedforms

For sandy-bed rivers, morphologists have defined three typical regimes: lower, transitional and upper transport regimes, each containing certain groups of bedforms. In the literature, there are different classifications of the bedforms in each regime. van Rijn (1993) classified the bed features as follow:

Lower transport regime (Figures 2.1A-C): consequent of flat bed, ripples, dunes and bars.

- Transitional regime(Figure 2.1D): washed-out dunes and sand waves
- Upper transport regime (Figures 2.1E-H): flat mobile bed and anti-dune sand waves which are characterized by a dominating suspended load transport.

As illustrated in Figure 2.1C, dunes have a length scale much larger that the depth of flow. They have a length of some tens of centimetres to a few metres in laboratory flumes and small streams, and a few hundred metres in larger rivers; their crest height ranges from centimetres to metres (Kennedy, 1969; Robert, 2003). They can form in cases where the flow velocity and the amount of sediment transport are higher relative to the case of ripples.

Ripples are triangular shape bedforms whose wave lengths are almost always less than 50 cm and wave heights are less than 10 cm (Figure 2.1A). Ripples may form on the stoss side of dunes (Figure 2.1B).

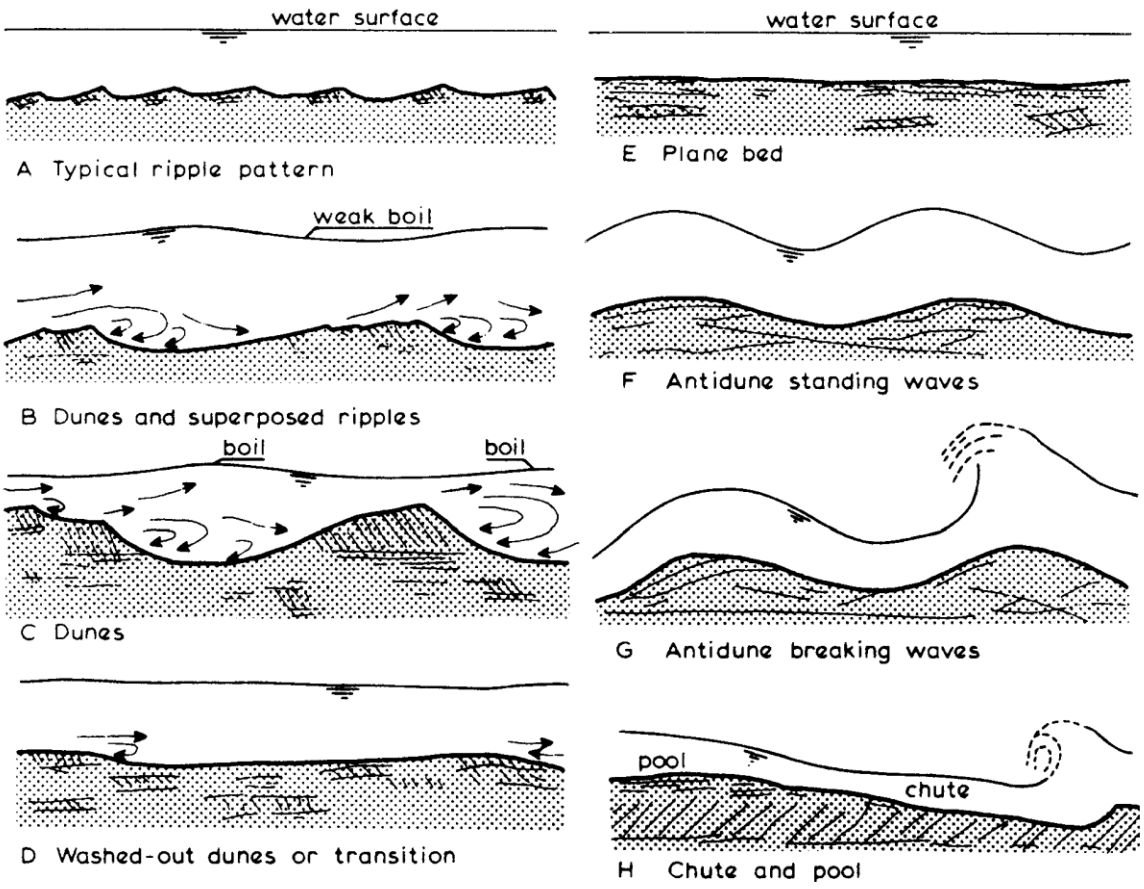

Figure 2-1. Bedform types in alluvial rivers according to Simons and Richardson (1966) (modified from van Rijn, 1993).

Field and experimental measurements of flow velocity from river channels with dune bedforms show that micro-turbulent events originate at the channel bed and produce upwelling on the free surface, known as kolks and boils (Matthes, 1947; Jackson, 1976). Kolks are twisting upward while shedding downstream; if strong enough, they reach the free surface, burst and form boils (Figure 2.1C). At increasing flow velocity, bedforms are washed out and a new regime will form. The upper transport regime is associated with supercritical flow (Figures 2.1E-H).

Anti-dunes can form in a shallow and rapid flow. They tend to migrate upstream until they disappear (Figures 2.1F-G). Chute and pools can form in a very steep channel when there is a large amount of sediment from upstream (Figure 2.1H). The flow is supercritical in a chute path; when reaching a pool, the flow can be subcritical or supercritical.

Riverbed sediments can be sands, gravel or a sediment mix of sands and gravel. Accordingly, sand dunes, gravel dunes or sands-gravel dunes form in rivers. Since flow structures and sediment transport characteristics depend on bed materials, sand dunes and gravel dunes are discussed separately in the following.

2.4.2 Sand dune geometry and dynamics

One would like to be able to predict the dimensions of dunes. Allen (1968) related the dimensions of sand dunes to the depth of flow. Raudkivi (1998) suggested that the maximum crest height of sand dunes is related to the depth of flow. Other researchers (Gill, 1971; Fredsoe, 1982; Yalin, 1972 and van Rijn, 1982) associated the dimensions of sand dunes with the bed shear stress.

Since 1990, extensive experimental investigations have been carried out regarding the interaction between dune bedform and flow (Bennett and Best, 1996; Lyn, 1993; Nelson et al., 1993; Kadota and Nezu, 1999; Venditti and Bennett, 2000), sediment bedload (McLean et al., 1999), suspended load (Venditti and Bennett, 2000) and vortex characteristics (Kadota and Nezu, 1999). The results show complex dune bedform patterns, turbulence characteristics and mean flow features. The main findings are as follows: Qualitatively speaking, the flow over a dune can be divided into five different

zones (Figure 2.2); the separation zone and shear layer are considered to be important sources for turbulence production, with the maximum turbulent kinetic energy occurring around the separation zone and the maximum shear stress over the crest and just downstream of the reattachment point.

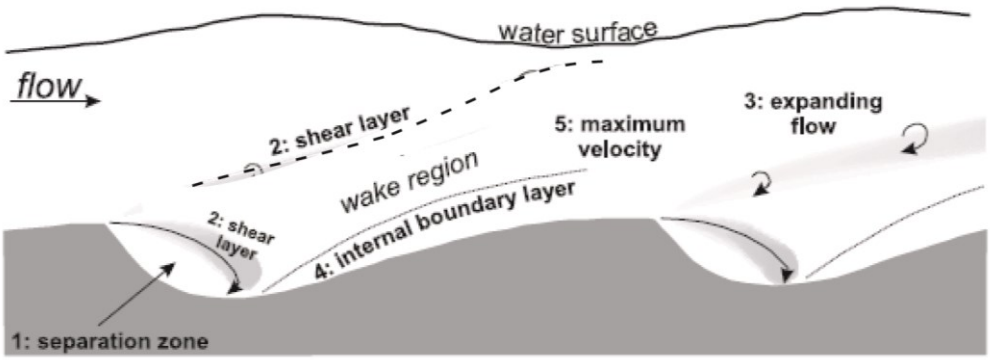

Figure 2-2. A schematic diagram of two-dimensional dunes and delineation of flow zones (modified from from Best, 2005).

Turbulent flow over fixed sand dunes was investigated experimentally by Mierlo and de Ruiter (1988), producing detailed measurements of flow velocity. Turbulent flows over dunes and associated morphological evolutions have also been investigated by means of numerical modelling. These modelling studies include direct numerical simulations (Shimizu et al., 2001), large eddy simulations (Stoesser et al., 2008; Yue et al., 2006) and solutions to the Reynolds-averaged Navier-Stokes equations (Yoon and Patel, 1996). Some researchers (Giri and Shimizu, 2006; Shimizu et al., 2009; Niemann et al., 2011) have considered the transport of sands for the initiation and evolution of bedform. These models are impractical to implement on the field scale (Giri and Shimizu, 2006; Rameshwaran et al., 2011) because they incur excessively high computational

costs. Besides, they require a large amount of input data which are not available in most cases. This inevitably limits their applications.

Sand dunes can grow and move across a gravel layer and subsequently diminish, as observed in the field by Carling et al. (2000). They proposed a six-stage conceptual model to describe the evolution of coarse sands dunes moving across a pavement of gravel. The height of large dunes is precluded by hydraulic constraints, notably a depth limitation. Wilbers and ten Brinke (2003) proposed some power relationships, which use Shield's mobility parameter to predict dune dimensions, migration and bedload transport. We caution that these models and relationships are empirical and site-specific.

2.4.3 Gravel dune geometry and dynamics

According to an early study by Shinohara and Tsubaki (1959), in gravel-bed laboratory flumes and small-scale channels, the most common bed features are mega-ripples and dunes. Recently, field observations (Carling, 1996; Carling and Shvidchenko, 2002; Kleinhans, 2001; Radecki-Pawlik et al., 2006; Wilbers and ten Brinke, 2003) and laboratory observations (Kleinhans, 2001; Carling et al., 2005) confirm the existence of gravel dunes and mixed sands-gravel dunes. However, the topic of gravel dune geometry and dynamics has not been explored adequately.

The formation of sands or gravel dunes was thought to depend on mainly flow discharge (Radecki-Pawlik et al., 2006) on the basis of a case study of a mixed sands-gravel bed river. The results indicate that at low discharge only sands dunes can form, and as discharge increases, sands-gravel dunes begin to develop, with bed features shorter, steeper and flatter than classical dunes. Wilbers and ten Brinke (2003) observed

that the growth and decay of gravel dunes depend on sediment grain size in addition to flow strength. For example, at the same flood discharge, dunes form more easily on fine sediments, whereas in coarser bed, dune growth may be retarded further as a result of armouring of the top layer of the bed. These observations were made from sandy-bed rivers and from mixed sands-gravel bed river reaches. Carling (1996) disputed the observations of Wilbers and ten Brinke (2003); based on a field study, Carling (1996) argued that sediment grain size is not a major control preventing dune-growth in coarse sediment. We can see uncertainties in the results about gravel dunes.

Dune development, specifically, the historic sorting of grain sediments on the leeside of dunes and selective deposition in dune troughs, strongly affects sediment transport and deposition in sand-gravel rivers (Kleinhans, 2001).

2.5 Bed shear stress and bed sediment transport

Critical shear stress is an important concept in bedload calculations. In gravel-bed rivers, the critical shear stress depends more on relative than absolute grain size (Ashworth and Ferguson, 1989). The question is whether the relative size effects can reduce the selectivity process. Ashworth and Ferguson (1989) showed that as shear stress rises toward the critical and beyond, size-selective entrainment moves individual particles from surface layer. This implies that a higher shear stress will lead to nearly equal mobility of small and large particles.

Sediment transport in rivers is known to have significant effects on flow characteristics, cause deposition and erosion at the riverbed and hence bring about changes in channel geometry. The presence of a floating ice cover in river channels

appears to increase flow depth, decrease bulk flow velocity, increase dune length, and significantly decrease bedload transport, as observed in the flume experiments (Smith and Ettema, 1997). They suggested that sediment transport relationships developed for open-water flow are applicable to ice-covered flow provided they are used in conjunction with estimates of actual bed shear stress.

There are three types of sediment bedload equations: duBoys type, Schoklitsch type and Einstein type. They are intended for calculating bedload under steady and unsteady conditions. The transport of sediments in a steady, uniform flow is defined as the amount of sediments that can be carried by the flow without net erosion or deposition when a sufficient amount of bed materials is available. Although this idealised condition has rarely been observed in any natural rivers, it is constructive to examine such a simple case. Most of the bedload equations are empirical or semi-empirical and therefore should be used under conditions of hydraulics parameters and sediment materials similar to those under which the equations were developed.

2.5.1. duBoys-type of bedload equations

The earliest bedload equation was proposed by duBoys (1879, cited in Graf, 1984), who assumed that sediment particles are moving along the bottom in layers, where their velocities vary linearly in the downward direction. The bedload equation (see Graf, 1984, p. 125) is given by

$$q_s = \chi \tau_b [\tau_b - \tau_c] \tag{2.1}$$

This relationship is based on the concept of excess shear stress; the relationship has been widely used. The parameter χ in equation (2.1) is defined as

$$\chi = \frac{\varepsilon v_s}{2\tau_c^2} \tag{2.2}$$

where ε is the layer thickness and v_s is a velocity of sediment layer.

Bedload equations that contain the excess shear stress, i.e. τ_b-τ_c or τ_b/τ_c is classified as the duBoys-type of equations. As summarised in Graf (1984), a number of river sediment researchers such as Straub (1935), Zeller (1963, cited in Graf, 1984) and O'Brein et al. (1933) tried to correct the wrong assumption of sliding layers by determining the characteristic sediment coefficients (χ) in equations (2.1) and (2.2) based on sediment grain diameter.

Shields (1936) first applied modern fluid mechanics concepts and considered more influence factors to derive a historically important bedload model equation. The equation is of the form

$$\frac{q_s \gamma_s}{q S \gamma} = 10 \frac{\tau_b - \tau_c}{(\gamma_s - \gamma) d} \tag{2.3}$$

This equation has allowed for all effective factors in a compact manner.

Another duBoys-type bedload equation was suggested by Kalinske (1947), which emphasised the important effects of turbulence mechanism on the flow and bedload motion. The average rate of sediment motion is expressed as

$$q_s = (\frac{\pi d^3}{6})(\frac{\rho_k}{\pi d^2/4})\overline{[u_b - (u_b)_{cr}]} \tag{2.4}$$

The first part of the right hand side of the equation refers to the volume of a single sediment grain, the second part represents the number of sediment grains in motion, and the third part is the average velocity at which sediment grains move.

2.5.2 Schoklitsch-type of bedload equations

This type of bedload equations is based on the so-called critical discharge. They are easier and more practical to use. The reason is that it is relatively easy to obtain river discharge than shear stress. On the basis of laboratory experiments, Schoklitsch (1930) suggested the following equation

$$q_s = \chi'' S^k (q - q_{cr}) \tag{2.5}$$

where χ'' is a new characteristic sediment coefficient.

Subsequently, Schoklitsch (1934, 1943, cited in Graf, 1984) derived two more formulae using the same concept; the latter (in metric units) is given by

$$\dot{q}_s = 2500 S^{3/2}(q - q_{cr}) \tag{2.6}$$

For sediments with specific gravity of 2.65, the author defined the critical discharge as

$$q_{cr} = \frac{0.6d^{3/2}}{S^{7/6}} \tag{2.7}$$

Meyer-Peter et al. (1934, cited in Graf, 1984) derived the first empirical relation for uniform grains of sand, barite and lignite. For sandy-bed rivers, they proposed a bedload equation (in metric units) of the form

$$0.4\frac{\dot{q}^{2/3}}{d} = \frac{\dot{q}^{2/3} S}{d} - 17 \tag{2.8}$$

As an extension to the above bedload transport equation, Meyer-Peter et al. (1948) presented an empirical equation for a sediment mixture of different grain sizes, given by

$$\frac{\gamma R_h (\frac{k}{k'})^{3/2} S}{d_{50}} - 0.047(\gamma_s - \gamma) = 0.25\sqrt[3]{\rho}\frac{(\dot{q}_s')^{2/3}}{d} \tag{2.9}$$

where d_m is the median grain size of the mixture, and $(\frac{k}{k'})^{3/2} S$ is part of the total energy slope S. This part is due to the grain resistance S'; it is responsible for bedload motion. The bedload rate $\dot{q}_s'$ (in under-water weight per unit time and width) is given by $\dot{q}_s' = \dot{q}_s(\gamma_s - \gamma)/\gamma_s$.

2.5.3 Einstein-type of bedload equations

This type of bedload equations avoids the difficult definition of incipient motion. The key concept behind Einstein's (1942) bedload equation is that the rate of sediment transport depends on turbulent flow fluctuations rather than the average value of exerted forces on

sediment grains. The incipient motion of sediment grains is expressed in terms of probability.

Einstein (1942) established three empirical relationships between the bed and moving bedload. The main idea was that the rate of deposition per unit area depends on the transport rate of sediments as well as the probability at particular time and space that hydrodynamic forces allow sediment grains to deposit. However, the rate of erosion depends on the number and properties of grains and the probability that instantaneous hydrodynamic lift force is large enough to move the grains (Yang, 1996, p. 100; Graf, 1984, p. 140).

In Einstein (1942), the bedload equation is for an equilibrium condition, meaning that the rate of deposition is equal to the rate of erosion. The resulting bedload equation in Einstein (1942, 1950) is given by

$$\frac{\dot{q}_s \, i_s}{A_L \, K_2 \, \gamma_s \, d^4} = \frac{i_b \, p_r}{K_1 \, K_3 \, d^2} \sqrt{\frac{g(\rho_s - \rho)}{d \, \rho}} \tag{2.10}$$

where A_L is a constant of bedload unit step, K_2 is the constant of particle volume, i_b is the fraction of bed materials of a given grain size, K_1 and K_3 are constants of grain area and time scale, respectively, and P_r is the probability of erosion.

In general form, the Einstein's bedload equation can be written as

$$\Phi_* = f(\Psi) \tag{2.11}$$

where Φ_* is the intensity of bedload transport, and Ψ is the flow intensity. Einstein (1950) replaced Φ_* and Ψ with analytical relationships which enable the formula to consider non-uniformity of bed materials.

2.5.4 Sediment transport modelling for uniform bed materials

Recently, numerical simulations of bed level changes associated with transport of sediments have attracted the attention of modelling researchers. It is necessary to simulate these changes for realistic predictions of flow characteristics. In this regard, some research efforts have been made in the past, as discussed in El kadi Abderrezzak and Paquier (2009). Examples include the development and application of one-dimensional models such as HEC6 (Thomas and Prashum, 1977), CCHE1D (Wu and Vieira, 2002), CONCEPTS (Langendoen *et al*., 2001) and GSTAR-1D (Yang *et al*., 2004). These models consider updating the cross-sectional geometry at each time step by moving the entire cross section (or only the points below the water surface) up or down by a certain distance in correspondence to the predicted deposition or erosion. This modelling method was also used by Lopes and Falcon (1999), Langendoen *et al*. (2002), Catella *et al*. (2005), and El Kadi Abderrezzak *et al*. (2008) in their numerical studies of sediment transport.

El Kadi Abderrezzak and Paquier (2009) suggested that the choice of methods for computing cross-sectional changes in the lateral direction has rarely been justified in one-dimensional models. This is due to a lack of measurements for comparison. Using an explicit finite difference method, the authors proposed a one-dimensional model for simulating unsteady flow and non-equilibrium sediment transport in an open channel.

The evolution of bed topography is governed by a sediment continuity equation, written for one single grain diameter as

$$\frac{\partial Q_s}{\partial x} + (1-\rho)\frac{\partial A_b}{\partial t} + \frac{\partial (AC_s)}{\partial t} = 0 \tag{2.12}$$

where Q_s is the volumetric sediment discharge, A_b is cross-sectional area of the bed above a reference datum, C_s is the section-averaged sediment concentration, and ρ is the bed porosity.

El Kadi Abderrezzak and Paquier (2009) made a number of assumptions to simplify equation (2.12) to

$$\frac{\partial Q_s}{\partial x} + (1-\rho)\frac{\partial A_b}{\partial t} = 0 \tag{2.13}$$

When using equation (2.13), they assumed that the sediment transport Q_s is the sum of bedload and suspended, making it difficult to distinguish bedload from suspended load when both exist in nature. The model was applied to simulate the morphological changes of the Ha!Ha! River (Quebec) after a dyke failure. There are some discrepancies between the simulated and surveyed geometries. The mode of transport as bedload and suspended load is approximately indicated by the ratio of fall velocity (ω) to shear velocity (u_*), $2 \prec \omega / u_* \prec 6$ defined as bedload and $\omega/u_* < 0.6$ as suspended load (Raudkivi, 1998, p.135).

A number of investigators have studied sediment transport in open channels of complex geometry such as meandering and sharply curved channels. Using three-dimensional CFD code, Olsen (2003) computed the formation of meandering channel. The code used is based on the finite volume method on unstructured grids and the *k*-ε model for turbulence closure. Olsen (2003) suggested that the CFD code has advantage of directly simulating the meandering process as opposed to introducing simplifications. However, the work suffers from two significant limitations: (a) it assumes fixed water surface throughout the computation, and (b) the bed materials are sands of uniform size.

Zeng *et al*. (2008) simulated the flow as well as sediment transport (bedload and suspended load) in a sharply curved channel. The authors claimed that this was the first work of computing fully 3D flow over a movable channel bed. They used finite difference methods to cast the governing partial differential equations on curvilinear grids.

Some researchers tried to simulate the flow over more complex bed topography. Sinha *et al*. (1998) carried out 3D simulations of flow in a natural river. They solved RANS equations with standard k-ε turbulent closure. The set of RANS equations is not closed due to the appearance of velocity fluctuation correlation terms. To close these equations some turbulence models on the level of zero-, one- or two- equations need to be introduced (Wu, 2008). The k-ε turbulence closure is a widely used two-equation model. The equations were written on boundary fitted curvilinear coordinates in conjunction with a multi-block approach to delineate mid-channel islands. Calculations were carried out for the flow through a 4-km stretch of the Columbia River. However, the water surface elevation was determined as a rigid-lid three-dimensional mesh. The elevation height was pre-calculated and given to the program as a fixed value.

2.5.5 Sediment transport modelling for non-uniform bed materials

All the simulations mentioned above have assumed that the bed materials are uniform. However, in natural rivers, the bed materials are typically in different grain sizes. The effects of the non-uniformity of bed materials were considered in Einstein (1950), Egiazaroff (1965), Samaga et al. (1986), and Ribberink (1987), as summarized in van Rijn (1993). Conceptually, one divides bed materials of different grain sizes into a

number of fractions, each containing sediment grains of a small size range. For each of the frictions, one applies the existent formulae with necessary corrections incorporated. One of these corrections allows for the non-uniformity effect of the bed material. This is necessary because coarser grains are less mobile than finer grains.

On the other hand, coarser grains are more exposed to the flowing water than finer grains; the coarser grains are like a shelter for the finer ones. As a correction factor, one increases the critical shear stress of the finer grains and decreases the critical shear stress for the coarser grains. Meyer-Peter and Mueller (1948) obtained bedload transport rate for non-uniform materials by integrating over all the fractions as

$$q_b = 8(\gamma_s - 1)^{0.5} g^{0.5} \sum_{i=1}^{N} p_i d_i^{1.5} (\mu\theta_i - \xi_i\theta_{cr})^{1.5} \tag{2.14}$$

where N represents the total number of size fractions.

Realistic simulations of sediment transport require the consideration of non-uniformity of bed materials. According to Parker *et al*. (1982) and Parker and Klingeman (1982), the coarsening of the surface layer of gravel-bed rivers during the equilibrium or near equilibrium sediment transport can act to increase the mobility of coarse particles at the expense of fine particles.

With reference to field data and by including the concept of hiding, Parker (1990) developed a surface-based model that can be applied to both equilibrium and disequilibrium condition. The quantification of hiding allows for both differential transports of grains of varying sizes, and at the same time the formation of a mobile armour. Wilcock and Crowe (2003) presented a direct, nonlinear relation between sand content and sediment transport rate. Their model is surface-based transport, based on

comprehensive coupled observations of flow, sediment transport and bed-surface grain size distributions. Their results indicate that increasing the sand content in gravel-bed channels lead an increase in transport rate, as illustrated in Figure 2.3.

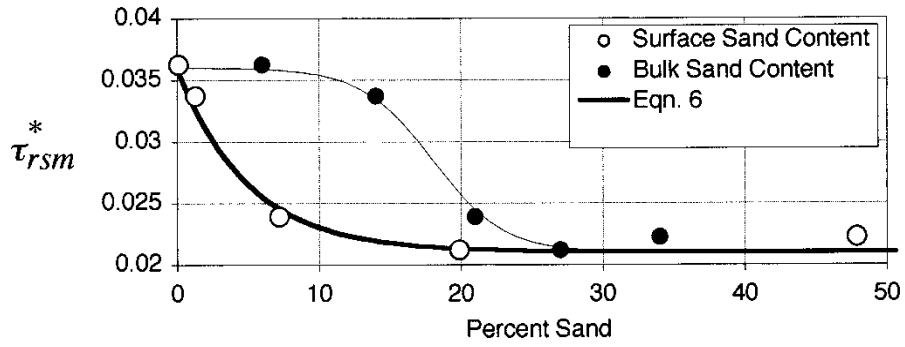

Figure 2-3. Variation of Shields parameter τ^*_{rsm} with changing sand content. The Shields parameter represents a dimensionless critical shear stress (adopted from Wilcock and Crowe, 2003).

In order to use either Parker's (1990) or Wilcock and Crowe's (2003) model, it is necessary to know the surface size distribution. However, to apply Parker's (1990) relation, all sand and finer materials should be removed from the sample when determining the grain fractions. The output from this model is prediction of bedload transport of gravel and coarser size only. The transport model of Wilcock and Crow (2003) is capable of predicting mixed sand and gravel sediments.

Klaassen (1992) examined the effects of non-uniform and uniform sandy bed materials on dune geometry. The author showed that the height and length of dunes of non-uniform materials are, respectively, 20% and 50% larger than those of uniform material dunes. The bedload transport rate is also approximately 50% higher for non-uniform bed materials compared to uniform bed materials.

To improve modelling accuracy, Lane *et al*. (2004) proposed to use regular, blocked, structured grids to represent gravel-bed rivers in high-resolution three-dimensional CFD simulations, without recourse to boundary-fitted coordinates. This is to avoid numerical diffusion and instability. However, a disadvantage in connection with using structured grids is that the computational cost is high in reach-scale applications.

A search of the literature shows some well-referenced numerical models such as FLUENT (http://www.fluent.com), FAST3D (Zhu, 1992), and ECOMSED (HydroQual, 2002) used as tools for simulating open channel flow in one to three dimensions. Dargahi (2004) used Fluent (general purpose CFD code) to study the characteristics of flow in a river bifurcation. Numerical results were obtained from solving the RNG k-ϵ equations, together with a non-equilibrium wall function and the sediment continuity equation. The results of sediment transport patterns at the river bifurcation were investigated by solving the sediment continuity equation in a short-term period. The reason of choosing a short period of time was that flow discharge remained constant during this period.

Bui and Rutschmann (2010) improved the model FAST3D in order to calculate flow and non-equilibrium transport of graded sediments in open channel under unsteady flow conditions. FAST3D uses multi-layer techniques. The full RANS equations are solved numerically using finite-volume methods on adaptive, non-staggered grids. The k-ε equations are used for turbulence closure. Their results showed that without the consideration of non-equilibrium sediment transport, the model could not produce realistic results under strong unsteady flow conditions. Note that the graded sediments considered have grain sizes limited to the range of sands.

Mekonen and Dargahi (2007) used the model ECOMSED to simulate flow and sediment transport in a 1-km reach of the sandy River Klaraven. The authors made an improvement to the advection scheme and river roughness parameterization. They also attempted to add bedload transport and update the depth of flow as the riverbed evolved.

Wu *et al*. (2000) incorporated the transport of suspended and bedload into the model FAST3D. In calculations of the flow field, they assumed that the flow is not influenced by the presence of sediments. This assumption is not valid for long-term simulations.

Chapter 3

Data-fitted velocity profiles for ice-covered rivers

Summary: A two-layer analytical function for the vertical distribution of water velocities in ice-covered rivers is obtained from a multi-parameter regression analysis. This analysis uses velocity profiles measured from Canadian rivers covered with ice during the winter. The function contains a coefficient and two exponents. The exponents are associated with the frictional effects of the ice and riverbed, respectively, whereas the coefficient is related to the per-unit-width discharge. The ranges of values for the three parameters have been determined. It is shown that the two-layer function is satisfactory for describing the velocity distribution. Velocity profiles reconstructed using the

parameter values are acceptable. Since it is difficult and expensive to obtain field measurements of water velocities from ice-covered rivers, the analytical function is a good alternative for such purposes as estimating winter discharges in such rivers. Also, the function can easily be incorporated into numerical models for simulating ice-covered river hydraulics.

3.1 Introduction

The study of ice-covered river (IR) flows is important for such purposes as determining winter discharges. Figure 3.1 shows an example of how streamwise flow velocities are distributed in space at an IR section. Due to the great complexity, the velocity distributions are poorly understood (Ettema, 2002). The purpose of this study is to determine a functional form suitable for describing the velocity distributions. A multi-variable regression analysis is performed using winter measurements of flow velocities from 26 IRs (Table 3.1). The function will be useful, especially when site-specific data are unavailable, and can possibly be incorporated into numerical models for IR flow simulations.

Previously, Lau (1982) numerically simulated IR flow and suggested that the logarithmic law gave overestimates of velocities over a large portion of the depth near the location of velocity maximum. Urroz and Ettema (1994) experimentally investigated the flow field associated with an ice jam formed in a curved flume, and reported that the two-layer hypothesis was not useful for ice-covered bend flows. Healy and Hicks (2004) discussed a velocity index method for calculating discharge from single-point field measurement of the maximum velocity at a given IR section. The problem is that we have

no prior knowledge about the location of the maximum velocity. By systematically comparing various velocity index formulations, Morse *et al*. (2005) identified their limitations and uncertainties for discharge calculations. With respect to the maximum-velocity location, they recommended the central part of the IR section in question. Previous studies have not dealt with any vertical structure of water velocity.

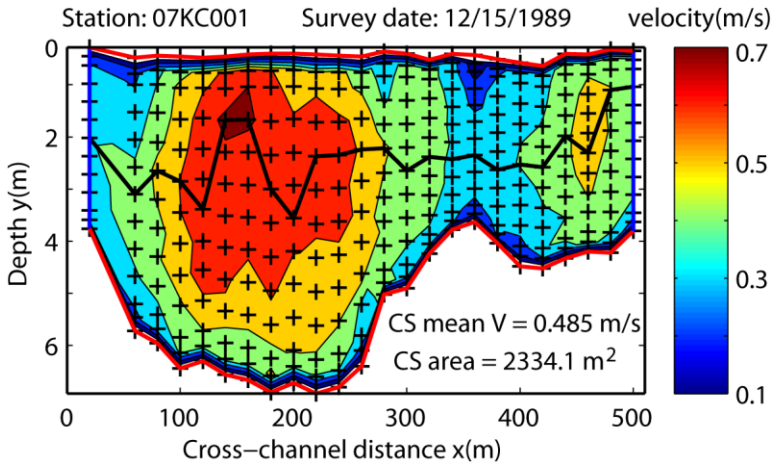

Figure 3-1. Contours of streamwise velocities measured at the '+' locations at the Peace River section. The thick, black curve connects points of the maximum velocity of 24 vertical profiles. The ice cover is between the top edge of the contour region and zero depth.

In the study, the IR sections used (Table 3.1) were surveyed up to three times in winter months of 1989-1991 (Walker and Wang, 1997) (see details in Appendix B). The surveys each produced 22-25 vertical profiles of streamwise velocity over the channel width (Figure 3.1); each profile contained velocities at 11 distinct depths (Figure 3.2). All the IR sections have a width much larger than the mean depth. With the exception of the Peace River, all have a per-unit-width discharge q in the range of 0.3–0.6 m^2/s. Thus, the

effect of secondary flow is negligible and the flow is roughly one-dimensional. During the survey periods, the flows were turbulent, with the Reynolds number $Re > 1.0\times10^6$ ($Re = VR_h/\nu$, where V is the cross-sectionally averaged velocity, R_h is the hydraulic radius and ν is the kinematic viscosity of water).

Table 3-1. A list of IR sections, showing hydraulic parameters and regression coefficients. The values represent the averages from all available surveys. The IR reaches are relatively straight

River name and province	Station ID	Discharge (m^3/s)	Bed slope	Mean depth (m)	Width (m)	k_o (m/s)	m_i	m_b	R^2
Salmon R., NB	01AN002	12	No data	0.7	34	1.00	4.93	3.36	0.92
S.W. Miramichi R., NB	01BO001	51	No data	2	92	0.50	7.39	3.59	0.88
R. John, NS	01DO001	2	No data	0.3	21	0.78	8.17	8.52	0.85
Kaministiquia R., ON	02AB006	43	0.0001	1.4	90	0.54	6.01	4.10	0.91
Saugeen R., ON	02FC002	29	0.000035	1.5	35	0.97	5.55	2.89	0.93
Nith R., ON	02GA038	1.5	No data	0.4	20	0.47	6.76	4.54	0.88
Burnt R., ON	02HF003	10	0.00004	1.9	32	0.29	5.48	3.20	0.84
Eels Cr.,ON	02HH001	1.94	0.00003	0.55	22	0.34	5.08	3.78	0.89
Moira R., ON	02HL005	2.22	0.00003	0.7	20	0.29	7.70	2.95	0.89
Salmon R., ON	02HM003	4.73	0.00002	1.7	40	0.13	5.47	2.45	0.90
Upper Humber R., NF	02YL001	64	No data	1.4	100	0.63	7.58	2.79	0.94
Terra Nova R., NF	02YS005	25	No data	2	67	0.34	7.19	2.61	0.91
Groundhog R., ON	04LD001	86	0.00034	2.9	148	0.34	4.66	3.50	0.82
Oldman R., AB	05AA023	2.33	0.0038	0.25	34	0.78	7.14	2.94	0.96
Red Deer R., AB	05CE001	18	0.00035	0.98	96	0.56	7.64	2.79	0.92
N. Saskatchewan R., SK	05GG001	116	No data	1.25	255	0.73	10.51	3.75	0.93
Ou'Appelle R., SA	05JF001	1.14	No data	0.4	15	0.32	6.25	5.70	0.84
Beaver R., AB	06AD006	2.69	0.00021	1.1	46	0.51	7.14	2.36	0.96
Pembina R., AB	07BC002	12	0.0001	0.7	74	0.47	6.25	3.23	0.94
Halfway R., BC	07FA006	7.4	0.0008	0.54	39	0.84	5.96	2.77	0.93
Litle Smoky R., AB	07GH002	11.5	0.00094	0.8	78	0.37	9.02	3.22	0.91
Peace R., NWT	07KC001	1111	No data	4.5	525	0.69	9.22	5.44	0.85
Yellowknife R., NWT	07SB002	24	0.00001	3	72	0.19	5.92	3.55	0.81
Fraser R., BC	08KA005	32	No data	1.3	95	0.45	6.37	3.25	0.95
Takhini R. YT	09AC001	14	No data	1.4	46	0.59	5.96	3.12	0.91
Yukon R., YT	09AH001	246	0.0004	2.5	145	1.49	7.06	3.69	0.93

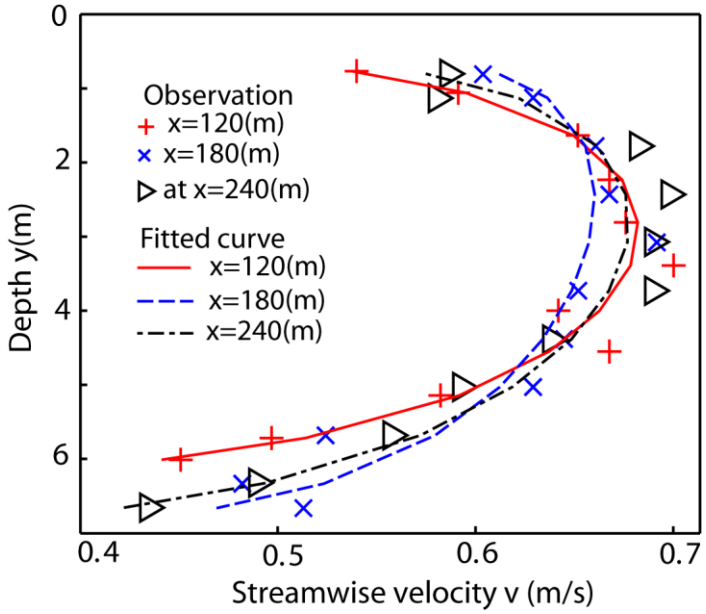

Figure 3-2. Data fitted velocity profiles at three x locations of the Peace R. section (see Figure 3.1).

3.2 Method

Following Uzuner (1975), we describe the streamwise velocity v as a function of depth y measured downward from the ice underside (Figure 3.1):

$$v = k_{\circ}\left(y/Y\right)^{1/m_i}\left(1-y/Y\right)^{1/m_b} \tag{3.1}$$

where k_o is a parameter related to q, Y is the total depth, and m_i and m_b are parameters associated with ice and riverbed frictional effects, respectively. Equation (3.1) is the so-called the two-power law; $v = 0$ at $y = 0$ (ice underside) and $y = Y$ (riverbed), and reaches the maximum somewhere between *0* and *Y*. This law assumes dynamically non-interactive ice and riverbed. The shape of the velocity profile depends on m_i and m_b. Once k_o, m_i and m_b are determined, the depth-averaged velocity $\bar{v}$ or q may be obtained by integrating v over y. The result of the integral is the beta function (Spiegel, 2009, p.152),

Here, we determine the three parameters by the least squares regression; we fit a curve given by Equation (3.1) (Figure 3.2, solid curve) to velocity data (Figure 3.2, the symbol '+').

The multiple regression model of the form $\mathbf{f} = \mathbf{X}\boldsymbol{\beta} + \boldsymbol{\varepsilon}$ is used [with the advantage that it allows us to explicitly control many other influence parameters, (Wooldridge, 2009)], where **f** is a column vector with *n* elements, **X** is a matrix that has *n* rows and (*k* + 1) columns, **β** is a column vector that contains (*k* + 1) regression coefficients, and **ε** is the column vector with *n* error elements. The mathematic expressions for these matrixes are

$$\mathbf{f} = \begin{bmatrix} f_1 \\ f_2 \\ . \\ f_n \end{bmatrix} \tag{3.2.a}$$

$$\mathbf{X} = \begin{bmatrix} 1 & x_{11} & . & x_{k1} \\ . & . & . & . \\ 1 & x_{1n} & . & x_{kn} \end{bmatrix} \tag{3.2.b}$$

$$\boldsymbol{\beta} = \begin{bmatrix} \beta_0 \\ \beta_1 \\ . \\ \beta_k \end{bmatrix} \tag{3.2.c}$$

$$\boldsymbol{\varepsilon} = \begin{bmatrix} \varepsilon_1 \\ \varepsilon_2 \\ . \\ \varepsilon_n \end{bmatrix} \tag{3.2.e}$$

We have *n* equal to 11, because the measured velocity profiles always contain 11 data points (Figure 3.1), and *k*+1 equal to 3, which correspond to the total number of parameters in Equation (3.1).

The least squares regression is performed to provide the vector estimator **b** of **β** in which **b** must satisfy $\frac{\partial}{\partial \mathbf{b}}\left[(\mathbf{f}-\mathbf{Xb})'(\mathbf{f}-\mathbf{Xb})\right]=0$. The expression $(\mathbf{f}-\mathbf{Xb})'(\mathbf{f}-\mathbf{Xb})$ is the residual squared sum. The above differentiation means $-2\mathbf{X}'\mathbf{f}+2(\mathbf{X}'\mathbf{X})\mathbf{b}=0$. This gives the general form of the least squares normal equation $(\mathbf{X}'\mathbf{X})\mathbf{b}=\mathbf{X}'\mathbf{f}$. If **X** is of full column rank, **b** can be obtained from $\mathbf{b}=(\mathbf{X}'\mathbf{X})^{-1}\mathbf{X}'\mathbf{f}$. For details of the multiple-regression model, refer to Myers (1990).

When applying the above regression model to the velocity profile given in Equation (3.1), it is appropriate to transform the equation by taking the natural logarithm. The resultant equation is

$$f=\beta_0+\beta_1 x_1+\beta_2 x_2+\varepsilon \tag{3.3}$$

where $f=\ln(v)$, $\beta_0=\ln(k_\circ)$, $\beta_1=1/m_i$, $\beta_2=1/m_b$, $x_1=\ln(y/Y)$, and $x_2=\ln(1-y/Y)$.

These relationships permit the determination of m_i, m_b and k_o values for individual vertical profiles of velocities. The averages of these individual values over the total number of profiles across the width of a river section from a survey are taken as the cross-sectionally averaged values of $k_{o,}$ m_i and m_b.

3.3 Discussion of results

The cross-sectionally averaged k_o, m_i and m_b values may well differ from survey to survey conducted at different times; in other words, they are expected to vary in time through the winter season. In Table 3.1, we present the averaged values, without any distinction of different survey months and years. It is understood that year-to-year variations in ice and hydraulics conditions in the river sections existed. When all the river sections and all the survey periods are taken into account, the overall mean values of k_o, m_i and m_b are 0.56, 6.78 and 3.62, respectively. The corresponding standard deviations are 0.30, 1.40 and 1.29. In the regression analysis of k_o, m_i and m_b in Equation (3.1), the coefficient of determination R^2 has a mean value of 0.90 and a standard deviation of 0.04. For individual profiles, the curve fitting has successfully reproduced the maximum velocities as well as their vertical structures.

For the practical purpose of constructing vertical profiles of velocity in small IRs, for which no velocity data are available, the overall mean values of m_i and m_b may be used as approximations. In fact, this overall m_i value is close to a 1/7 power-law [being valid for the friction-velocity-based Reynolds number in the range of $100 < \frac{u_* y}{\nu} < 1000$, (Hinz, 1975, p. 629)]. In comparison, the riverbed is rougher, and a 1/4 power-law is recommended.

To reveal how k_o varies with q, the k_o values for the 26 sections and all the surveys are combined and sorted according to q. The q values are in the range between 0.06 and 2.45 m^2/s. This range is evenly divided into bins of a 0.01 m^2/s interval. The k_o values belonging to the same bin are averaged and then plotted (Figure 3.3). The added trend line is not meant for extrapolation use. The k_o increases with increasing q, although the k_o

values scatter on both sides of the trend line, in particular for large q values. A combination of the overall mean m_i and m_b values and typical k_o values with channel geometry makes it possible to estimate discharges for IRs.

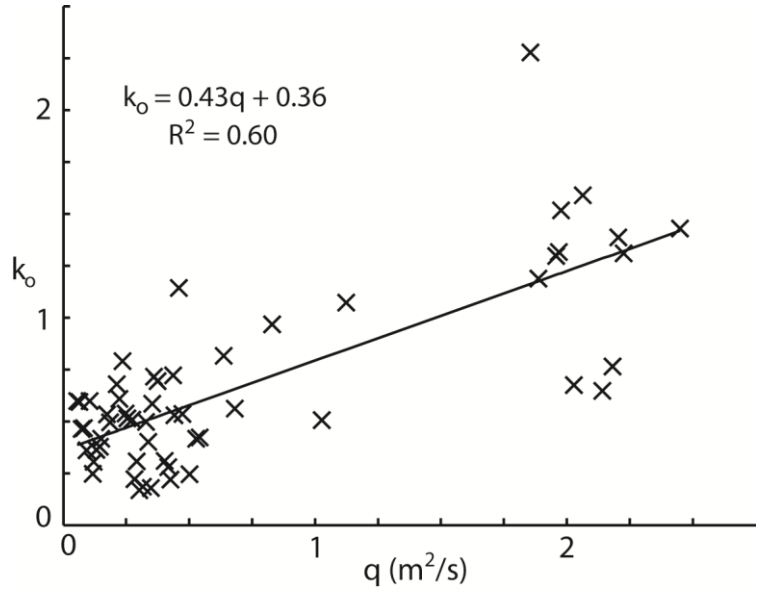

Figure 3-3. Cross-sectionally averaged k_o value varying with q.

Traditionally, bottom roughness coefficients (e.g. Manning's n) are given constant values as approximations under open-channel conditions. Is this approximation still valid for IRs? To answer this question, we combine the m_b values for all the IR sections and all the available surveys, and then sort the values according to survey time (elapsed days) through the winter. For the same elapsed day, the m_b values are averaged and then plotted in Figure 3.4. In like manner, the m_i values are combined, sorted and plotted in the same figure. Interestingly, m_b gradually decreases through the winter time due to the presence of ice covers. Relatively speaking, m_i decreases rapidly in time. IR flows can be subject to stronger frictional effects due to both the riverbed and the ice over the winter time; as a

result, velocity profiles change shape (Equation (3.1)). We declare that the parameter values in Figure 3.4 scatter above and below the added trend lines (low R^2 values), some of which are far off the lines. The scattering is due to the use of a large number of observed velocity profiles from IRs under largely different ice conditions.

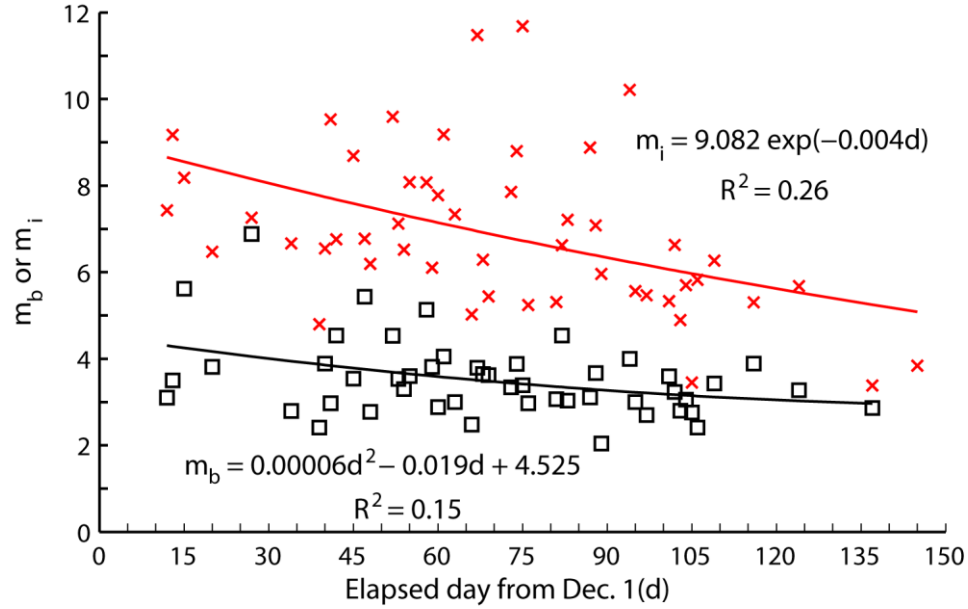

Figure 3-4. Cross-sectionally averaged m_b (□) and m_i (×) values varying through the wintertime.

Based on our calculations (Figure 3.4), frictional effects caused by both the riverbed and the ice cover grow over the winter time. This is a new finding. Stronger friction effects mean higher energy head losses in IR flows. The identification of physical processes responsible for such increasing losses entails detailed measurements of climate and local variables from the channel stations. Since such measurements are not available to this study, it is difficult to identify the physical processes. However, an examination of the field data of ice cover thickness appears to show a trend of growing thickness over the

winter time. This growth tends to decrease the cross sectional area of water flow and hence to increase water velocity shear, particularly near the solid boundaries (the riverbed and ice cover).

In IRs, such important problems as sediment transport (Sayre and Song 1979), channel erosion (Tsai and Ettema 1994) and ice jam (White 2003) have received great attention. The finding that friction effects increase over the winter time has important implications to numerical studies of these problems. If a depth-averaged numerical model based on the concept of friction coefficient is used to predict sediment transport, channel erosion and ice jam, the coefficient should be allowed to increase temporally over the winter time.

In Figure 3.5(a), we show a comparison between computed depth-averaged velocities and the corresponding observed panel velocities for some profiles, which are selected from the central parts of the IRs (Table 3.1). The central parts contain the most signifciant information of flows (Morse *et al*., 2005). The depth-averaged velocities computed using k_o, m_i and m_b values for individual profiles (termed as calibration) match the observations quite well. With m_i and m_b set to 7 and 4 respectively, the computations appear to give depth-averaged velocities larger than the observed values by about 14% (on average). However, the computed and observed values are still well-correlated with a correlation coefficent equal to 0.96. This means that the predicted vertical distributions of streamwise velocities are acceptable.

A comparison between observed and computed discharges for the IRs (Table 3.1) is shown in Figure 3.5(b). The computations are based on the k_o, m_i and m_b values for individual profiles (calibration). If m_i and m_b are set to 7 and 4 respectively, the computed

discharges are higher than the observed discharges by a percentage similar to the computed depth-averaged velocities in comparison with the observed panel velocities (Figure 3.5(a)).

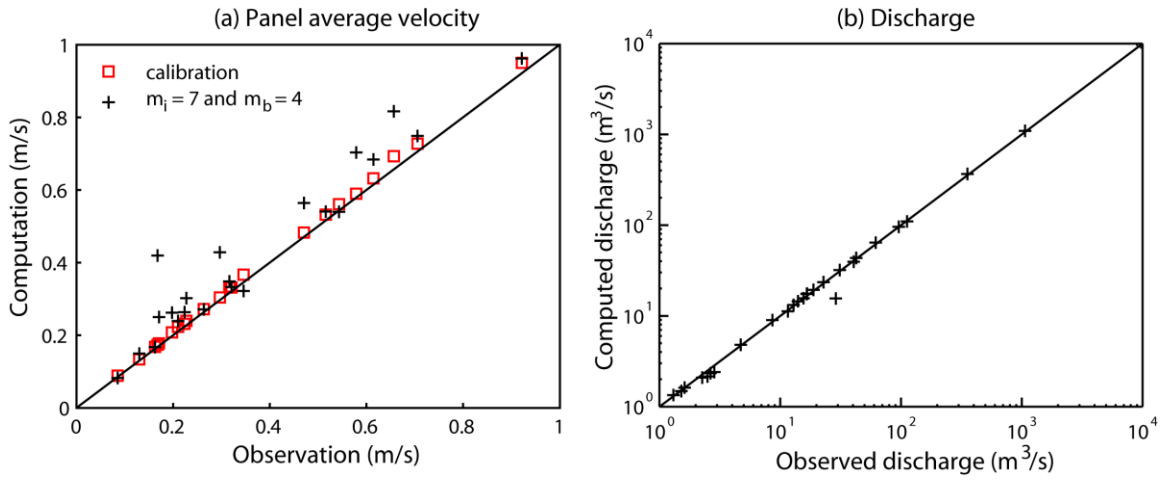

Figure 3-5. Comparisons between (a) observed panel velocities for selected profiles and the corresponding computed depth-averaged velocities; (b) observed and computed per-unit-width discharges for the IR sections (Table 3.1).

3.4 Conclusion

The three parameters k_o, m_b and m_i in the two-power law for ice-covered river flows (Equation (3.1)) have been determined using field measurements of velocity profiles. Both m_i and m_b show a decrease in time through the winter; this decrease corresponds to an increase in frictional effects. If all the river sections and all the available surveys are considered, the overall mean value and standard deviation are, respectively, 6.8 and 1.4 for m_i, and 3.6 and 1.3 for m_b. The parameter m_i has a slightly larger standard deviation than the parameter m_b. The parameter k_o value, after being normalised by the depth-

averaged velocity, may be taken to be 1.84. Thus, we propose a velocity profile function of the form

$$v = k_{\circ}\left(y/Y\right)^{1/7}\left(1-y/Y\right)^{1/4} \tag{3.4}$$

This function is simple relative to the logarithmic law of the wall. Furthermore, it is continuous and differentiable between the ice cover and riverbed; there is no need to consider the flow underneath the ice and the flow above the riverbed as two separate boundary layers. The function would be useful for the purpose of estimating shear stresses near the solid surfaces, given the notorious difficulties in making near-surface velocity measurements.

.

Chapter 4

Momentum, energy and drag coefficients for ice-covered rivers

Summary: A lack of reliable hydraulic parameters has been a main factor hindering the progress in predicting ice-covered river flows; the predictions need input hydraulic parameters such as the energy, momentum, and drag coefficients (α, β and C_D). In this chapter, a large volume of winter measurements of flow velocity collected from 26 ice-covered rivers is analysed in order to determine the coefficients. Using cross-sectionally distributed streamwise velocities, α and β are evaluated directly. They are also derived from empirical relationships. For both the riverbed and ice cover, C_D is evaluated on the basis of turbulent boundary-layer theory and the quadratic law for friction. The results

show that ice-covered river flows feature a number of velocity distributions: a single core of high velocities in the thalweg, a single core of high velocities off the thalweg, and multiple cores of relatively high velocities at the cross section. The velocity distributions are significantly non-uniform. Direct evaluations give overall averages of α = 1.23 and β = 1.08. They represent 22% and 8.3% corrections to the literature values (overestimates). An examination of the velocity distributions reveals that the ratio of the maximum velocity to the cross-sectionally averaged velocity equals 1.356. It is recommended that values of C_D = 0.004±0.0005 and 0.002±0.0005 be used for the riverbed and ice, respectively. This chapter discusses turbulence shear stress and the associated length scale in the boundary layer as well as winter discharges. The results have applications to aquatic ecology, water resources development and flood prevention.

4.1 Introduction

The ice-covered condition of river flows in cold regions in winter harbours relevance to engineering. Potential problems arising from this state include a blockage of inlets to power station cooling systems (Wadhams, 2002), damage to river engineering structures, ice jams (Beltaos, 2001; Prowse, 1990) and river floods (Calkins, 1986) among others. In order to address these issues related to ice-covered rivers in a scientifically sound manner, it is important to be able to predict the flows. This is difficult, partly owing to a lack of reliable hydraulic parameters needed as input for the hydrodynamics predictions.

The hydraulic parameters include the energy coefficient, α, and the momentum coefficient, β (Chow, 1959), which are needed for predictions of (one-dimensional) cross-sectionally averaged flow, the Manning's coefficient, n, or equivalent resistance

coefficients, which are required for predictions of (two-dimensional) depth-averaged flow, and the drag coefficient, C_D (Wu, 2008) for predictions of fully three-dimensional flow. Discussion of the Manning's n for ice-covered rivers can be found in Larsen (1969), Calkins (1986) and Li (2012). The purpose of this study is to obtain good estimates of α, β and C_D, which are not available from previous studies of ice-covered river flows.

For this purpose, one needs distributed flow velocities at ice-covered river cross sections. A review of the literature shows that a formula exists for calculating the distribution of flow velocities across an ice-covered river (Shen and Ackermann, 1980). The calculation has the advantage that only the geometry of the flow area between the ice cover and the riverbed is required as input. However, it gives no information about the vertical distribution of streamwise flow velocities under the ice cover. Both the vertical and horizontal distributions are needed for estimates of α, β, n and C_D. Traditionally, the vertical distribution has been described by the two-power law (Larsen, 1969; Uzuner, 1975). With respect to its validity, some researchers (Sayre and Song, 1979; Teal *et al*., 1994) reported a reasonable fit of flow velocity data to the law. Other researchers (Urroz and Ettema, 1994) suggested that the two-power law is inadequate for describing ice-covered bend flows. According to Lau (1982), the logarithmic law appears to overestimate velocities near the location of velocity maximum. The analyses mentioned above used data from simplified laboratory experiments of ice-covered channel flow. In reality, ice-covered rivers are typically much more complicated in terms of ice condition, channel geometry and velocity distribution. Using field data from ice-covered river cross sections, Attar and Li (2012) obtained a two-power law for describing the vertical

distribution. The use of the velocity distribution formulae may lead to uncertain estimates of α, β and C_D.

In this study, measurements of distributed flow velocities made at ice-covered river cross sections (Walker and Wang, 1997) are used directly. In the remaining part of this chapter, the data source is described (Section 4.2), the methods for analysing the data are introduced (Section 4.3), and the results are presented and discussed (Section 4.4), before conclusions are drawn (Section 4.5).

4.2 Field data

A large volume of winter measurements of streamwise flow velocity were obtained from Water Survey of Canada (more details given in Appendix B). These measurements were made from 26 ice-covered river cross-sections (Table 4.1) in the winter of 1989, 1990 and 1991 (Walker and Wang, 1997). Most of the cross sections were surveyed repeatedly (up to 11 times) in different months of the winter season. The discharges varied from 1 to 10^3 m^3/s (order of magnitude). The mean depths ranged from tens of centimetres to a few metres. All the 26 river cross-sections are wide, with a width larger than the corresponding depth by at least one order of magnitude. Thus, the flows were predominantly in the horizontal direction.

Table 4-1. A summary of the basic hydraulic parameters, including discharge (Q), mean depth (H) and top width (B), for 26 ice-covered river cross sections, along with calculated values for the momentum coefficient (α), energy coefficient (β) and drag coefficient (C_D). The channel-bed slope is presented in Table 3-1.

River name and province	Station ID	Q (m^3/s)	H (m)	B (m)	B/H	α				β				C_D	
						Max	Min	Ave (Eq. 3)	Ave (Eq. 6)	Max	Min	Ave (Eq. 4)	Ave (Eq. 7)	Ice	Riverbed
Oldman R., AB	05AA023	2.3	0.25	34	136	1.41	1.26	1.36	1.31	1.15	1.09	1.12	1.43	0.0023	0.0036
R. John, NS	01DO001	2.0	0.3	21	70	-	-	1.37	1.58			1.12	1.47	0.0023	0.0032
Nith R., ON	02GA038	1.5	0.4	20	50	-	-	1.09	1.76			1.03	1.08	0.0023	0.0043
Ou'Appelle R., SA	05JF001	1.1	0.4	15	38	1.08	1.05	1.07	1.42	1.03	1.02	1.02	1.09	0.0027	0.0025
Halfway R., BC	07FA006	7.4	0.54	39	72	1.40	1.25	1.29	1.34	1.14	1.08	1.10	1.28	0.0028	0.0043
Eels Cr.,ON	02HH001	1.9	0.55	22	40	1.35	1.22	1.27	1.20	1.11	1.08	1.09	1.50	0.0026	0.0072
Salmon R., NB	01AN002	12.0	0.7	34	49	1.14	1.12	1.12	1.53	1.05	1.04	1.04	1.14	0.0030	0.0039
Moira R., ON	02HL005	2.2	0.7	20	29	1.50	1.44	1.47	1.76	1.17	1.15	1.16	1.53	0.0023	0.0068
Pembina R., AB	07BC002	12.0	0.7	74	106	1.08	1.07	1.08	1.82	1.03	1.02	1.03	1.08	0.0027	0.0039
Litle Smoky R., AB	07GH002	11.5	0.8	78	98	1.22	1.17	1.19	1.45	1.08	1.06	1.07	1.23	0.0026	0.0063
Red Deer R., AB	05CE001	18.0	0.98	96	98	1.28	1.21	1.25	1.64	1.10	1.07	1.09	1.26	0.0023	0.0065
Beaver R., AB	06AD006	2.7	1.1	46	42	1.27	1.22	1.24	1.41	1.09	1.08	1.08	1.28	0.0022	0.0048
N. Saskatchewan R., SK	05GG001	116.0	1.25	255	204	1.14	1.11	1.13	1.61	1.05	1.04	1.04	1.16	0.0021	0.0045
Fraser R., BC	08KA005	32.0	1.3	95	73	1.21	1.20	1.20	1.72	1.08	1.07	1.07	1.16	0.0027	0.0052
Kaministiquia R., ON	02AB006	43.0	1.4	90	64	-	-	1.15	1.51	-	-	1.05	1.20	0.0019	0.0037
Upper Humber R., NF	02YL001	64.0	1.4	100	71	2.05	1.22	1.67	1.36	1.31	1.08	1.20	2.18	0.0019	0.0070
Takhini R. YT	09AC001	14.0	1.4	46	33	1.51	1.40	1.45	1.22	1.18	1.15	1.16	1.68	0.0025	0.0040
Saugeen R., ON	02FC002	29.0	1.5	35	23	-	-	1.21	1.53	-	-	1.08	1.15	0.0022	0.0067
Salmon R., ON	02HM003	4.7	1.7	40	24	-	-	1.25	1.18	-	-	1.09	1.22	0.0031	0.0072
Burnt R., ON	02HF003	10.0	1.9	32	17	1.33	1.28	1.30	1.55	1.12	1.10	1.11	1.27	0.0026	0.0040
S.W. Miramichi R., NB	01BO001	51.0	2	92	46	1.33	1.22	1.26	1.47	1.11	1.08	1.09	1.32	0.0023	0.0033
Terra Nova R., NF	02YS005	25.0	2	67	34	1.22	1.16	1.19	1.47	1.08	1.06	1.07	1.20	0.0025	0.0137
Yukon R., YT	09AH001	246.0	2.5	145	58	1.21	1.06	1.12	1.56	1.08	1.02	1.04	1.11	0.0022	0.0032
Groundhog R., ON	04LD001	86.0	2.9	148	51	1.16	1.12	1.14	1.36	1.05	1.04	1.05	1.33	0.0031	0.0039
Yellowknife R., NWT	07SB002	24.0	3	72	24	1.24	1.18	1.21	1.79	1.08	1.06	1.07	1.30	0.0026	0.0051
Peace R., NWT	07KC001	1111.0	4.5	525	117	1.32	1.14	1.21	1.25	1.11	1.05	1.07	1.24	0.0019	0.0022

During the surveys, a river cross section in question was divided across its width into 18 to 30 smaller subsections or strips (Figure 4.1), depending on the width. Within each subsection, a hole was bored through the ice. Then, a Price winter meter was lowered through the hole into the flowing water. The instrument recorded water velocities at eleven depths evenly spaced between the ice cover and the local riverbed (Figure 4.2), producing a vertical profile of streamwise flow velocity. In total, 18 to 30 vertical profiles from each surveyed river section for each survey time are available.

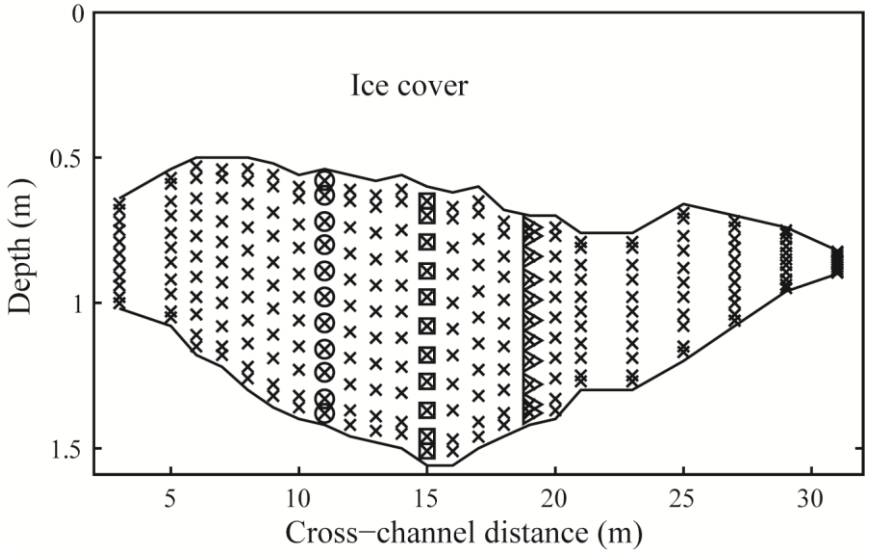

Figure 4-1. The Halfway River (ID = 07FA006; location = 56°15'4"N, 121°37'39"W in British Columbia, Canada) covered with ice of varying thickness measured on March 16, 1990. Beneath the ice cover, the symbol '×' marks the positions of streamwise velocity measurements from 23 smaller vertical strips.

The ice-covered condition of river flow at a sample cross section is shown in Figures 4.1 and 4.2. The ice cover had a maximum, a minimum and an average thickness of 0.82, 0.53 and 0.66 m, respectively; the flow had a maximum depth of 0.94 m (Figure 4.1). As expected, the presence of ice and the riverbed resulted in relatively low velocities near the two solid boundaries (Figure 4.2). Flow velocity increased monotonically with depth below the ice, reached a maximum value at a certain depth closer to the ice than to the riverbed, and then decreased with depth toward the riverbed. These velocity profiles have a relatively simple, two-layer vertical structure. Many of the other velocity profiles (not shown) used in this study have vertical structures much more complicated than that shown in Figure 4.2.

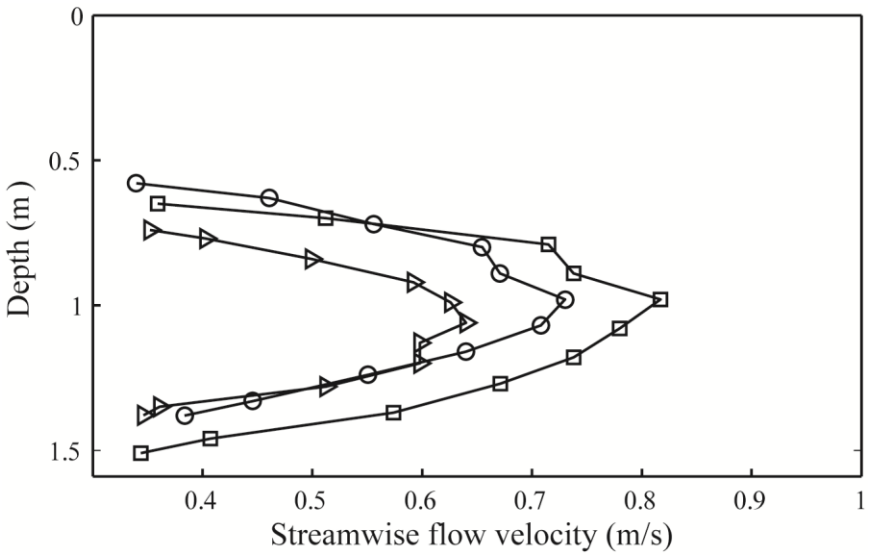

Figure 4-2. Vertical profiles of streamwise velocity measured from the three vertical strips marked by the symbols '○', '□' and 'Δ' in Figure 4.1.

The surveyed river cross sections were selected using a number of criteria: (a) A complete ice cover existed, with no evidence of slush; (b) the river reaches were straight, with minimum longitudinal variations in ice thickness; (c) the bed materials were homogeneous, without complication due to grain size distributions; (d) no obstructions occurred immediately upstream or downstream, which isolated the effects of the ice and riverbed; (e) the sections were fairly uniform, and thus the flow was less complicated. These less complicated conditions justify some simplifications in the analysis of the field data.

4.3 Methods

4.3.1 The energy and momentum coefficients

Let (x, y, z) denote the Cartesian coordinates, in which the x-axis points in the streamwise or along-channel direction, the y-axis in the cross-channel direction, and the z-axis in the vertical direction (Figure 4.3). At a given cross section, the energy and momentum coefficients for cross-sectionally averaged flow are defined as

$$\alpha = \frac{\int\int u(y,z)^3 \, dydz}{U^3 A} \tag{4.1}$$

$$\beta = \frac{\int\int u(x,y)^2 \, dydz}{U^2 A} \tag{4.2}$$

in which u is the streamwise flow velocity, U is the cross-sectionally averaged streamwise velocity, and A is the flow area. In order to evaluate A, U, α and β, one needs data of channel bathymetry, ice-cover thickness and distributed flow velocities.

Since the velocity data to be used for the evaluations are from discrete points at the cross section in question, Equations 4.1 and 4.2 are approximates as summations of the form

$$\alpha = \frac{\sum_n \left(u_n{}^3 \, \Delta A_n \right)}{U^3 \sum_n \Delta A_n} \tag{4.3}$$

$$\beta = \frac{\sum_n \left(u_n{}^2 \, \Delta A_n \right)}{U^2 \sum_n \Delta A_n} \tag{4.4}$$

in which the script n is the nth elementary area of the cross section, $\Delta A_n = \Delta y_i \Delta z_j$, Δy_i and Δz_j are the width and height of the elementary area, respectively, and u_n is the point velocity from the area's centre.

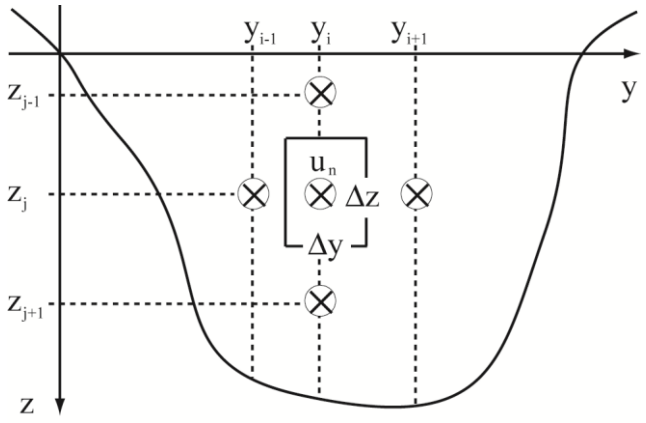

Figure 4-3. A definition diagram of a river cross section, showing an interior elementary area (rectangular box). The symbol '×' marks the positions of streamwise velocity measurements (see Figure 4.1). The *x*-coordinate points in the into-of-paper direction.

Let N denote the total number of vertical profiles of streamwise velocity at the cross section in question. The width and height of an interior elementary area (Figure 4.3) are calculated as $\Delta y_i = (y_{i+1} - y_{i-1})/2$ and $\Delta z_j = (z_{j+1} - z_{j-1})/2$, respectively. For velocity profiles next to the left and right riverbanks, the widths are given by $\Delta y_1 = (y_2 - y_1)/2$ and $\Delta y_N = (y_N - y_{N-1})/2$, respectively. Similarly, for point velocities next to the ice cover and the riverbed, the heights of the element are calculated as $\Delta z_1 = (z_2 - h_i)/2$, and $\Delta z_{11} = (h_b - z_{11}) + (z_{11} - z_{10})/2$, respectively, where h_b = the vertical distance between the riverbed and the ice-cover underside, and h_i = the thickness of the ice cover.

The cross-sectionally averaged velocity in Equations 4.1 and 4.2 is expressed as

$$U = \frac{\iint u(x,y)\,dydz}{\int (h_b - h_i)\,dy} \tag{4.5}$$

The integrals in the equation are approximated as summations in a similar way as in Equations 4.3 and 4.4. Sub-areas where velocity measurements are missing are skipped from calculations. At a given river cross section, the maximum velocity, U_m, for each survey is identified. For the 26 river cross sections listed in Table 4.1, α and β will be estimated directly using Equations 4.3–4.4, on the basis of the field measurements described in the preceding section.

4.3.2 Empirical relationships for the energy and momentum coefficients

Chow (1959) suggested an empirical relationship each for α and β as

$$\alpha = 1 + 3\varepsilon^2 - 2\varepsilon^3 \tag{4.6}$$

$$\beta = 1 + \varepsilon^2 \tag{4.7}$$

where the parameter $\varepsilon = U_m / U - 1$. The empirical relationships are deceptively convenient as the only required input data are U_m and U. In fact, for reliable estimates of these two input quantities, details of the channel geometry as well as distributions of the flow velocity are needed. Values for α and β will be determined from Equations 4.6 and 4.7 and compared with those determined from Equations 4.3–4.4.

4.3.3 Bottom drag coefficient

Consider steady turbulent flow between the ice cover and the riverbed within a vertical subsection or strip (Figures 4.1–4.2). The steadiness approximation is valid over a time scale that is relatively short. The conservation of mass and momentum equations are given by

$$\frac{\partial u}{\partial x} + \frac{\partial w}{\partial z} = 0 \tag{4.8}$$

$$u\frac{\partial u}{\partial x} + w\frac{\partial u}{\partial z} = -\frac{1}{\rho}\frac{\partial p}{\partial x} + \frac{\partial \tau_{xx}}{\partial x} + \frac{\partial \tau_{xz}}{\partial z} \tag{4.9}$$

where w is the vertical component of the Reynolds averaged velocity, p is the Reynolds averaged pressure, ρ is the density of water, and τ_{xx} and τ_{xz} are the specific Reynolds shear stresses.

Within a vertical strip (Figure 4.1), the two solid boundaries, i.e. the ice cover and riverbed, may be taken as parallel flat plates extending infinitely in the x direction. The streamwise velocity u becomes independent of x. The vertical velocity w is zero on the

riverbed and everywhere between the riverbed and the ice cover. As an approximation, the pressure is considered to be constant in the x direction. Note that the shear stress τ_{xx} is not important. Thus, Equation 4.9 is simplifies to

$$\partial \tau_{xz}/\partial z = 0 \qquad \text{or} \qquad \tau_{xz} = \text{constant} \tag{4.10}$$

Under the Boussinesq approximation, the shear stress τ_{xz} is expressed as $\tau_{xz} = (\nu + \nu_T)(\partial u/\partial z + \partial w/\partial x)$, where ν (= 10^{-6} m/s^2) is the molecular viscosity and ν_T is the eddy viscosity. That is to say that the τ_{xz} expression includes both molecular and eddy viscous effects. Since $\partial w/\partial x = 0$, the τ_{xz} expression is simplified to

$$\tau_{xz} = (\nu + \nu_T)\partial u/\partial z \tag{4.11}$$

Let v_τ denote the friction velocity, defined as $v_\tau \equiv (\tau_b/\rho)^{1/2}$, where τ_b is the turbulent shear stress on the riverbed. Equation 4.11 may be rewritten as

$$\left(\nu + \nu_T\right)\frac{du}{dz} = v_\tau^{\,2} \tag{4.12}$$

Note that in the limit of approaching the riverbed or $z \rightarrow h_b$, the turbulent eddy viscosity ν_T vanishes; inclusion of ν in Equation 4.12 ensures consistence with the expression of τ_b.

In order to solve Equation 4.12 for the streamwise velocity u, the concept of turbulence mixing length λ for turbulence closure is used. The eddy viscosity is formulated as $\nu_T = \lambda^2 \left| \partial u/\partial z \right|$. The mixing length is calculated from the model equation of the form $\lambda = \kappa d(1 - d/D)$.

where κ is the von Karman constant (= 0.41), d is the distance of a point of interest from the riverbed or the underside of the ice cover, and D is the distance between the riverbed or the ice cover and the point where u reaches the maximum (Figure 4.2). It can be shown that with the model equations mentioned above for the eddy viscosity and turbulent mixing length, integration Equation 4.12 gives the streamwise velocity as

$$u = \frac{v_\tau}{\kappa} \ln\left(\frac{d}{D-d}\right) + \frac{v_\tau}{\kappa} \ln\left(\frac{v_\tau D}{\nu}\right) + C v_\tau \tag{4.13}$$

where the law of the wall has been imposed as the condition as $d \rightarrow 0$, and C is a constant (= 5.5). Equation 4.13 permits the determination of the bed shear stress implicitly. In a similar manner, the shear stress at the ice cover may be determined.

In three-dimensional modelling of river flows, the water column in the vertical may be partitioned into multiple layers. Let u_b denote the streamwise velocity of the layer nearest to the solid boundary (the riverbed or the underside of the ice cover). In the flow model, the dynamic condition on the bed can be implemented through the use of the drag coefficient as

$$\tau_b = \rho C_D u_b |u_b| \tag{4.14}$$

Realistic values for C_D are necessary for successful flow modelling. In this study, C_D values are estimated as below: First, determine implicitly the friction velocity v_τ using Equation 4.13. Then, calculate the bed shear stress from $\tau_b = \rho v_\tau^2$. Last, determine C_D using Equation 4.14. Note that the functional form of Equation 4.14 is applicable for determining C_D on the riverbed as well as the underside of the ice cover.

4.4 Results

4.4.1 Velocity distribution

At the ice-covered river cross sections listed in Table 4.1, measured streamwise flow velocities feature non-uniform cross-sectional distributions. Roughly speaking, the distributions can be classified into three types of velocity patterns. The first type exhibits a single core of relatively high velocities within the thalweg (Figure 4.4a); the second type also exhibits a single core of relatively high velocities, positioned off the thalweg (Figure 4.4b); the third type contains multiple cores of relatively high velocities (Figure 4.4c).

The velocity pattern shown in Figure 4.4a is based on the velocity profiles made from the Yukon River in January 1990. The January distribution of velocities gives a cross-sectionally averaged velocity of U = 0.85 m/s and a maximum velocity of U_m = 1.29 m/s. The maximum velocity occurred at the location marked by the symbol '+'. A single core of high velocities appeared in the thalweg. The ice cover extended from the zero depth line to the upper edge of the contour region.

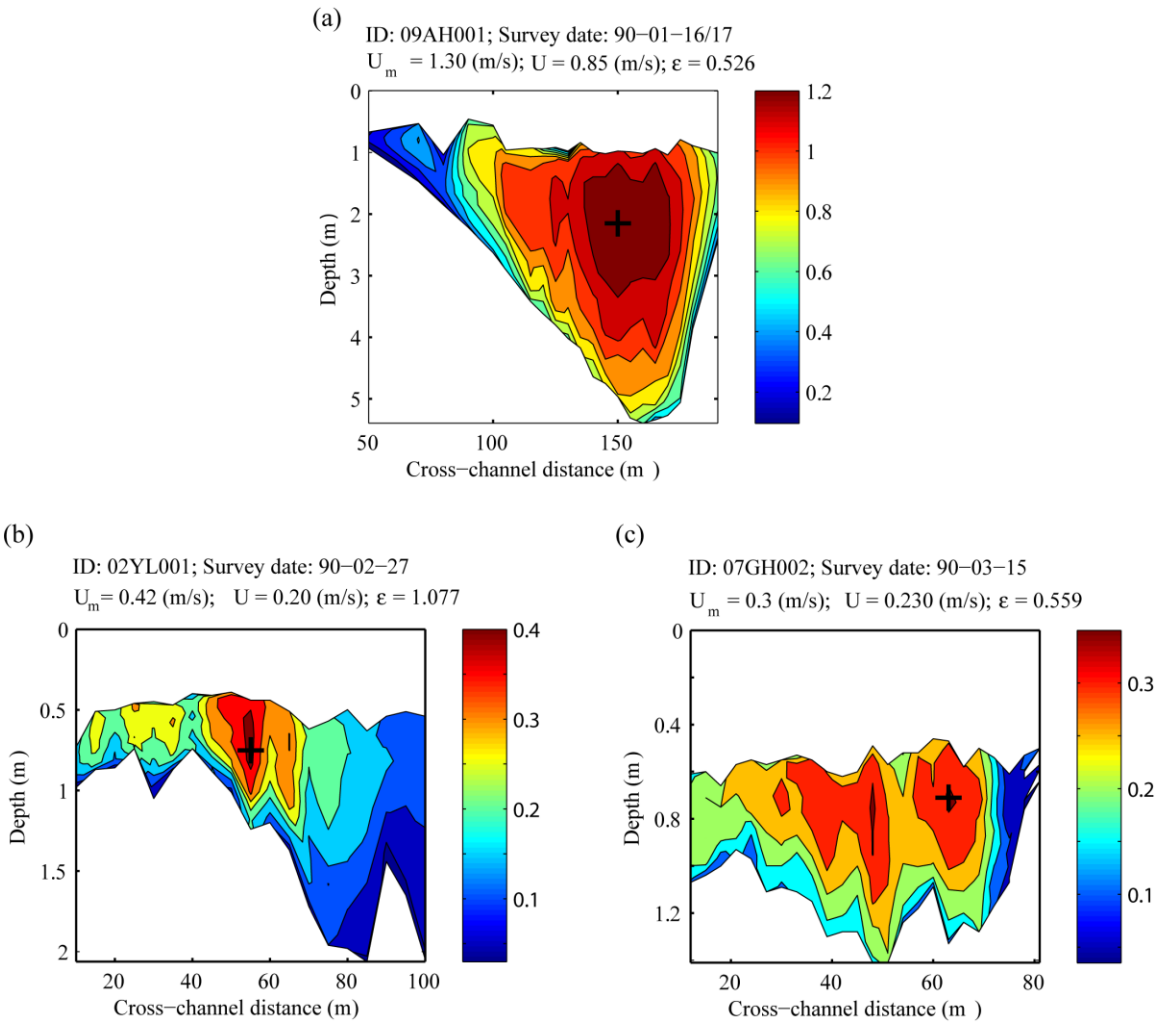

Figure 4-4. Velocity contours showing a single core of high velocities (a) in the thalweg and (b) outside the thalweg, and (c) multiple cores of relatively high velocities.

A comparison of the January flow distribution (Figure 4.4a) to the March flow distribution (not shown) reveals that flow velocities varied significantly from January to March. An examination of the distributions of streamwise velocities at the other river cross sections (most of them not shown) showed significant variations in flow velocities with time, as expected. The ice cover appeared to be more or less uniform across the channel width. On the other hand, it gradually grew in thickness with time. As an approximation, the ice-covered river flows may be treated as being quasi-steady and the ice cover as piecewise flat plates.

4.4.2 The α and β coefficients

In total, 86 surveys were conducted at the 26 river cross sections listed in Table 4.1 (Some of them were surveyed multiple times). Each survey produced an α value (Equation 4.3) and a β value (Equation 4.4). The α and β values versus the survey month/date (No distinction between survey years is made) are shown in Figures 4.5a,b. The α and β coefficients exhibit little fluctuation throughout the course of the winter months. As expected, all the estimated α and β values are larger than unity because of the non-uniform distributions of the measured streamwise flow velocities, and at the same time the β values are smaller than the corresponding α.

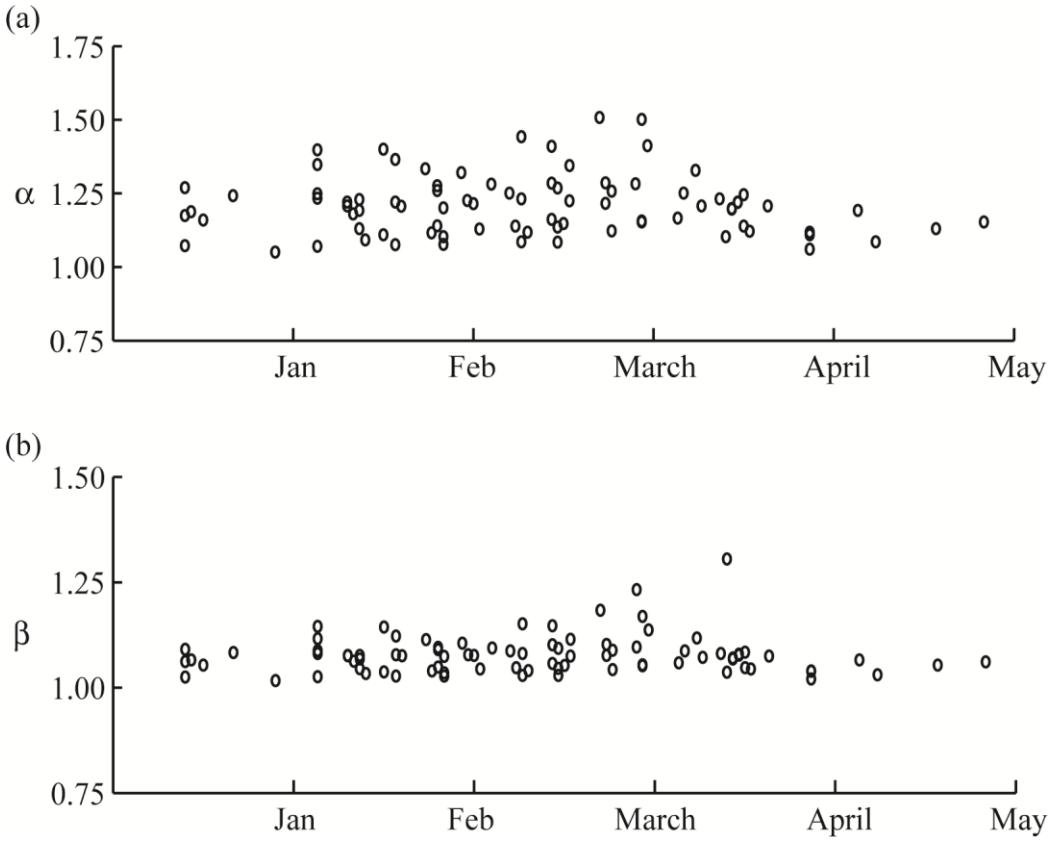

Figure 4-5. Estimates of (a) the α coefficient and (b) the β coefficient versus month/date. No distinct between survey years is made.

When all the river cross sections (Table 4.1) are taken into account, except the Upper Humber River (02YL001), the coefficients are in the range of α = 1.05–1.51, with an overall average of α = 1.23, and in the range of β = 1.02–1.18, with an overall average of β = 1.08. For the Upper Humber River, the highest values for the coefficients are α = 2.05 and β = 1.30, as estimated using velocity measurements from one of the three surveys conducted. This is because the velocity distribution from that particular survey was highly non-uniform. On average, the literature values for α and β (Chow, 1959) are 18% and 8.3%, respectively, higher than the estimated averages for α and β from this study (Table 4.2).

Table 4-2 A comparison of the α and β coefficients determined using different methods.

Methods	α			β		
	Min.	Ave.	Max.	Min.	Ave.	Max.
Definition (Equations 4.3 and 4.4)	1.05	1.23	2.05	1.02	1.08	1.31
Empirical relationships (Equations 4.6 and 4.7)	1.07	1.49	2.00	1.02	1.30	2.88
Chow (1959)	1.20	1.50	2.00	1.07	1.17	1.33

In Table 4.1, the α and β coefficients estimated using Equations 4.3 and 4.4 for the 26 river cross sections (Table 4.1) are summarized, along with a comparison to the values as derived from the empirical relationships (Equations 4.6 and 4.7). Most of the cross sections were surveyed multiple times, which produced more than one value for the coefficients; the range of values for the coefficients was determined. For almost all the individual cross sections, the values are in a narrow range, meaning that the α and β coefficients as determined from survey to survey are consistent to each other. Note that five of the cross sections were surveyed only once; the coefficients obtained are shown as the average values.

When all the river cross sections and all the surveys are taken into account, the overall average values for the coefficients are α = 1.24 and β = 1.08, with a standard deviation of 0.14 and 0.04, respectively. Thus, for the practical purpose of one-dimensional modelling of cross-sectionally averaged flows in ice-covered rivers under hydraulic conditions similar to those in Table 4.1, these overall average values for the coefficients are recommended.

It appears that the use of the empirical relationships (Equations 4.6 and 4.7) leads to overestimates of the α and β coefficients (Table 4.1). The overestimates are up to 30% for α and up to 44% for β, in comparison to the values for the coefficients as determined

using the definition equations (Equations 4.3 and 4.4). The most problematic case is that a river cross section has a very small core of high velocities and therefore the maximum flow velocity at the cross section is much higher than the cross-sectionally averaged flow velocity. An example of such a case is illustrated in Figure 4.4b.

An analysis of the field measurements used in this study gives an overall average value of $\varepsilon = 0.356$ ($\varepsilon = U_m / U - 1$**).** If the empirical relationships (Equations 4.6 and 4.7) are used to calculate the α and β coefficients, one obtains $\alpha = 1.29$ and $\beta = 1.13$, which are close to the overall average values of $\alpha = 1.23$ and $\beta = 1.08$, as determined using the definition equations (Equations 4.3 and 4.4). However, if the ε parameter is calculated individually for the 26 river cross sections and for all the surveys, and the α and β coefficients are calculated using the empirical relationships, the overall average values of the coefficients are as high as $\alpha = 1.49$ and $\beta = 1.30$. This is because the coefficients non-linearly depend on the parameter.

4.4.3 Shear stress

In Figures 4.6a-c, some representative plots of the bottom shear stress τ_b are shown. At the surveyed river cross sections (Table 4.1), τ_b is on the same order of 10^{-1} (N/m^2), except at four of the cross sections. The first exception is river section 09AH001, where τ_b is on the order of 1 (N/m^2) in the central portion of the cross section. The other three river sections are 02HL005, 02HM003 and 07SB002, where τ_b is on the order of 10^{-2} (N/m^2). The reported values for the bottom shear stress τ_b were obtained as follows: First, for a given velocity profile (see Figure 4.2), data of streamwise flow velocity u and corresponding distance d (Equation 4.13) between the local riverbed and the depth of the

maximum velocity were identified. Then, for each pair of u and d data, the friction velocity v_τ was determined by implicitly solving Equation 4.13. Next, the v_τ values for all the pairs of u and d data were averaged to give the friction velocity value for the given velocity profile. Lastly, the bottom shear stress was calculated from $\tau_b = v_\tau^2 \rho$. Thus, by following the calculation steps mentioned above for all the vertical profiles of streamwise velocities measured across the width of a given cross section (Figure 4.1), one obtains the distribution of τ_b across the river width (Figures 4.6a-c).

In a similar manner, the distribution of the shear stress at the underside of the ice cover across the channel width was obtained, using data of flow velocities between the ice and the point where the maximum velocity occurred at a given vertical strip (Figures 4.1 and 4.2). Examples of the results are shown in Figures 4.6d-f for the same cross sections as in Figures 4.6a-c. A comparison between Figures 4.6a and 4.6d shows that the shear stresses near the ice cover are almost twice those near the riverbed. This means that the riverbed was rougher than the ice cover. As a result, the velocity profiles shifted toward the ice, and the locations of the velocity maxima were closer to the ice than to the riverbed. The rougher riverbed gave rise to increased shear stresses near the ice cover. In the case of Figure 4.6e, the riverbed was somewhat rougher than the ice cover. A comparison between Figures 4.6c and 4.6f indicates that the riverbed and the ice cover had more or less the same roughness. Clearly, the hydraulic roughness of the riverbed and the ice cover affect the vertical distribution of streamwise flow velocities.

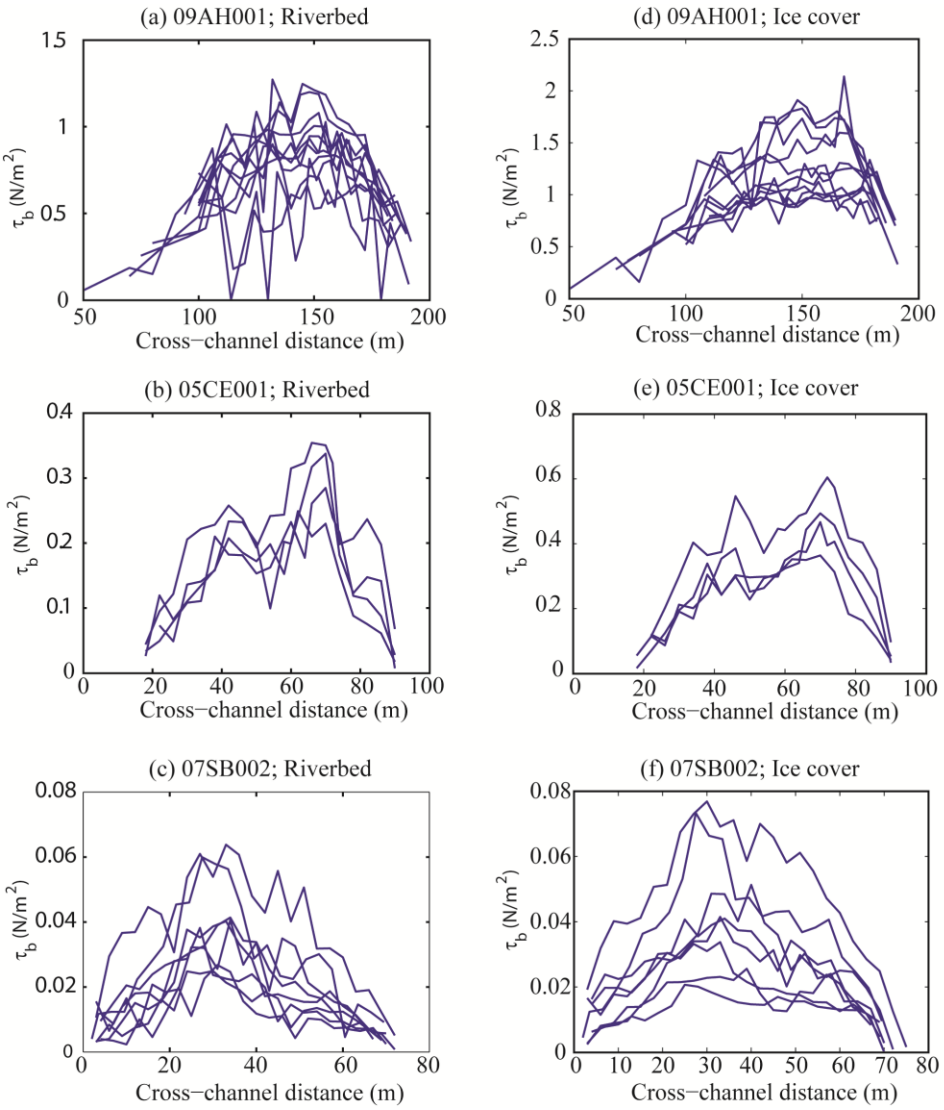

Figure 4-6. Cross-channel distributions of the calculated shear stress on the riverbed (a, b and c) and on the ice cover (d, e and f) for three river cross sections. In each panel, the different curves correspond to surveys conducted on different months/dates.

4.4.4 Drag coefficient

Now, for all the river cross sections (Table 4.1) and for all the surveys, values for the shear stress on the riverbed and ice cover are available for calculating the drag coefficient C_D (Equation 4.14). The required streamwise velocity u_b in the equation is taken as the point velocity nearest to the riverbed/ice cover from each velocity profile (Figures 4.1 and 4.2). The calculated C_D values for the riverbed are shown in Figure 4.7, where each symbol '○' corresponds to a vertical profile of streamwise flow velocity.

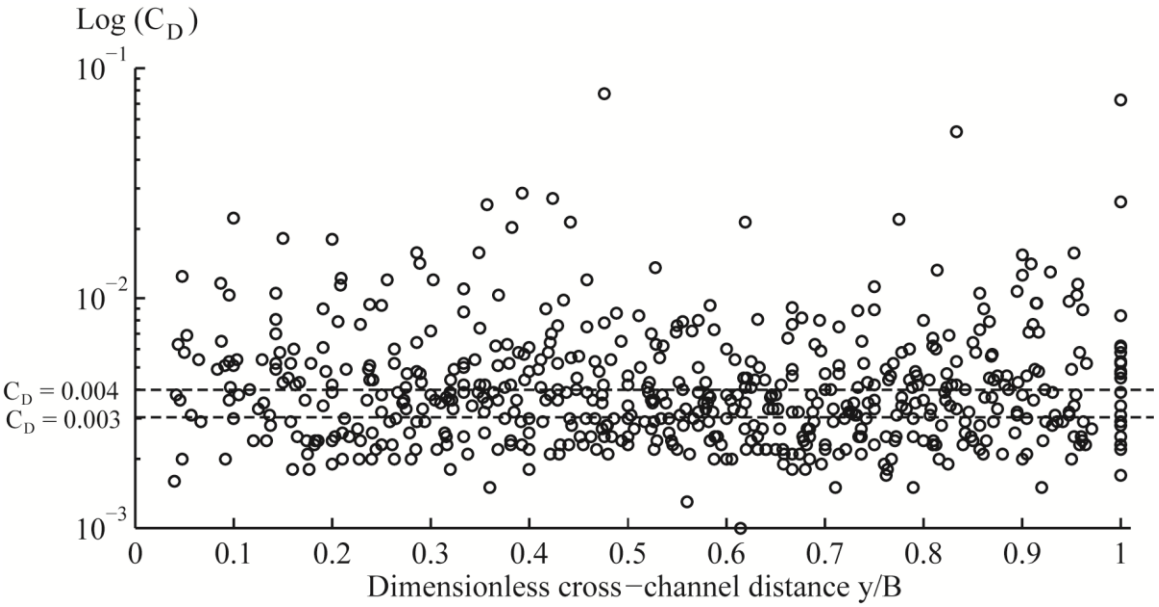

Figure 4-7. Distribution of the bottom drag coefficient values across the width of the river cross sections. All the velocity profiles were used to derive the coefficient. The horizontal axis is normalised by the top width of the individual rivers – that is, the left and right riverbanks of the river sections are all located at distances of 0 and 1 (dimensionless), respectively.

The drag coefficient values appear to scatter in a wide range of values (from 0.001 to 0.1). Simple statistics of the value distribution were carried out using 0.0005 as the interval to sort the coefficient values into different bins. The statistics indicate that C_D in the bin of 0.0035 to 0.004 is the highest in occurrences, followed by C_D in the bins of 0.004 to 0.045, and 0.003 to 0.0035. C_D in the other bins is low in occurrences.

For the ice cover, the distribution of the drag coefficient values is shown as a histogram in Figure 4.8. When all the velocity measurements are taken into account, the coefficient shows peak occurrences in the range of C_D = 0.002–0.0025. The second highest occurrences are in the range of C_D = 0.0015–0.002, followed by the range of C_D = 0.0025–0.003. For individual river cross sections, average values for the drag coefficients for the riverbed as well as the ice cover are listed in Table 4.1.

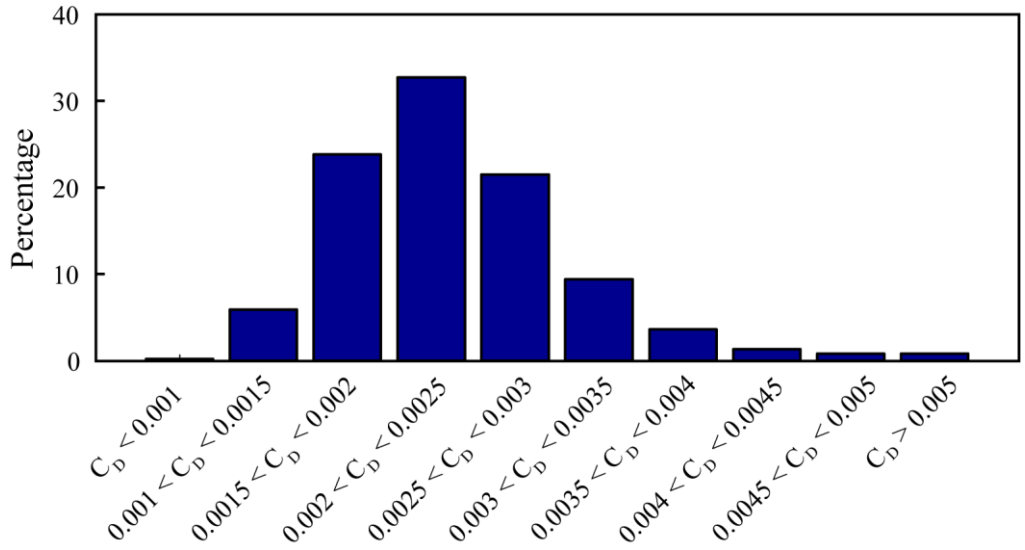

Figure 4-8. Distribution of the drag coefficient values for the ice cover. All the velocity profiles were included in the statistical analysis.

4.5 Discussion

Flow velocity distributions in ice-covered rivers are seen to vary significantly from month to month in the winter season and from river section to river section. This has significant implications for the determination of winter discharges using the so-called velocity index methods (Healy and Hicks, 2004). The velocity index methods require a single-point field measurement of the maximum velocity at a given ice-covered river section. It is difficult to locate the core(s) of high velocities and therefore difficult to apply the methods. This is particularly problematic in the case where the maximum velocity does not occur in the vicinity of the thalweg, as is the case with the distributions illustrated in Figures 4.4b and 4.4c.

It appears that the ratio of the maximum flow velocity to the cross-sectionally averaged velocity is close to U_m/U = 1.356 at ice-covered river cross sections. This information is useful for the conversion from the maximum velocity to the averaged velocity and for further calculations of the discharge using the averaged velocity, along with data of the flow area for a given river cross section. This assumes that the approximate position of the maximum velocity at a given river section can be identified and the maximum velocity can be measured.

In the steady, one-dimensional form of the momentum equations, one must use the momentum coefficient β to correct the momentum flux as $\beta\rho QU$ to account for a non-uniform velocity distribution. For the same reason, it is necessary to use the energy coefficient α to correct the velocity head term as $\alpha U^2/2g$ in the Bernoulli equation. The use of the literature values for the coefficients (Chow, 1959) would lead to over corrections. To the authors' knowledge, this study represents the first study to derive the

energy and momentum coefficients from a large volume of field data. The results presented in Table 4.1 may be used as a reliable reference for similar ice-covered rivers. It is important to note that in the case of irregular channel alignment, the coefficients are expected to change from section to section.

There is an increasing demand for predictive tools for river flow applications to compensate decreasing river gauging infrastructures. In principle, CFD modelling can be applied to ice-covered rivers. One way to handle the riverbed and ice cover in CFD modelling is to apply the no-slip boundary condition, meaning that the bottom and ice boundary layers must be resolved at the turbulence length scale. It is not practical to implement CFD modelling with the boundary layers resolved because the computational costs are prohibitively high. A better alternative is to use the drag coefficient to parameterise the frictional effects of the two solid surfaces on the flowing water between them. This study facilitates the application of CFD modelling to ice-covered rivers by presenting drag coefficient values pertinent to ice-covered rivers.

It is worth noting that ice-covered river flows are more complicated in terms of non-uniform velocity distributions, compared to river flows under open water conditions. Reliable flow resistance coefficients for both the riverbed and ice cover must be specified for computations of depth-averaged flow. Relevant bed shear stress parameters are needed for computations of three-dimensional flow. Literature and site-specific values for the above-mentioned coefficients and parameters may be available for river flows under open water conditions, but these values may not be relevant to ice-covered river flows.

The length scale of turbulence near the riverbed may be defined as $\eta = \nu/v_\tau$. This parameter is important to the study of the velocity structures in the vicinity of the

riverbed as well as fish habitats. This parameter is also important to the formulation of sediment bedload transport. When all the velocity profiles available to this study are used in the analysis, the length scale is shown to have an overall average value of η = 1.06 mm, with a standard deviation of 0.07 mm. The bottom shear stress must be given in hydrodynamic models for simulations of ice-covered river flow; this is essential to the modelling of river ice dynamics (Shen *et al*. 2000; Shen, 2010). The results of shear stress on the riverbed presented in Figures 4.6a-c are useful.

4.6 Conclusions

This chapter has provided reliable estimates of the energy, momentum and drag coefficients through an analysis of a large volume of field measurements of flow velocity profiles collected from ice-covered river sections. These estimates, along with estimates of the Manning's coefficient, are useful for modelling studies of ice-covered river flows in various dimensions. The main findings are as follows:

(a) The energy and momentum coefficients are estimated to be α = 1.23 and β = 1.08, respectively, in comparison to the overestimated literature values of 1.50 and 1.17. On the reach scale, one-dimensional modelling of cross-sectionally averaged flow is attractive because of its computational efficiency; the two coefficients provide necessary input.

(b) Suitable drag coefficients are C_D = 0.0035–0.0045 for the riverbed and C_D = 0.0015–0.0025 for the ice cover. These results are useful for studies of the formulation of bedload transport and the associated riverbed erosion in ice-covered rivers.

(c) The cross-sectionally averaged velocity is proportional to the maximum velocity at the same river section. The ratio of the maximum to averaged velocity is 1.356. This value represents a good approximation for all the surveyed ice-covered river sections. This parameter may be used for the determination of winter discharges at ice-covered cover rivers, but not for the determination of the energy and momentum coefficients.

(d) The bed shear stress has a median value of 0.1 N/m^2, as determined using the mixing length theory for the riverbed boundary layer. The associated length scale of turbulence is 1 mm. This parameter has applications to boundary layer investigations.

(e) A variety of velocity distributions exist at ice-covered river sections: Some feature a single core of high flow velocities in the thalweg, some show a single core of high velocities off the thalweg, and the others have multiple cores of relatively high velocities at the cross section. This finding has important implications for the use of velocity index methods for determining winter discharges at ice-covered rivers.

Chapter 5

Modelling velocity structures and bed shear stress over gravel dunes

Summary: A poor understanding of near-bed flow over bedforms has hindered the progress in modelling bedload and bed level change in alluvial channels. This chapter aims to produce detailed near-bed flow and to establish links between near-bed flow and bed shear stress useful for bedload and bed level change calculations. We predict the flow structures over fixed gravel dunes using a 3-D hydrodynamics model and further predict the bed shear stress using different methods. New ADV measurements from flume experiments are used to verify the predictions. The model has several advantages including dune-surface-following σ coordinate, fine spatial resolutions near the bed and

high computational efficiency. The predicted velocity profiles and bed shear stress values agree reasonably well with the ADV measurements at different locations over the dune length, especially at the dune crest. A dynamic equilibrium between dune morphology and flow field is reached after the fifth dune. Velocity shear is the most significant near the bed, within the bottom 17% layer of the local depth of flow; it drops by almost an order of magnitude further above the bed. For the purpose of modelling bedload, it is appropriate to link the bed shear stress to near-bed flow velocity using the logarithmic law; using flow velocities at the wall distance of $y^+ \approx 300$ gives consistent values for the friction velocity and hence the bed shear stress. Along the dune length, the bed shear stress reaches the maximum at the dune crest. This location is the most important for bedload transport. When using the multi-layer modelling approach, we propose a minimum of five layers to resolve near-bed flow structures within the bottom one-fifth layer of the local depth of flow.

5.1 Introduction

Dunes are commonly formed at an alluvial riverbed when the flow exerts sufficiently strong excess shear stress. Dunes have a longitudinal profile of approximately triangle shape, with a mild stoss side and a steep leeside (Figure 5.1a). The leeside slope angle is roughly equal to the angle-of-repose of the bed sediments, although low-angle dunes are present in larger rivers (Best, 2005). Dunes have a length of some tens of centimetres to a few metres in laboratory flumes and small streams, and a few hundred metres in larger rivers; their crest height ranges from centimetres to metres (Kennedy, 1969; Robert, 2003). Dunes have significant effects on sediment transport, hydraulic resistance and

(a)

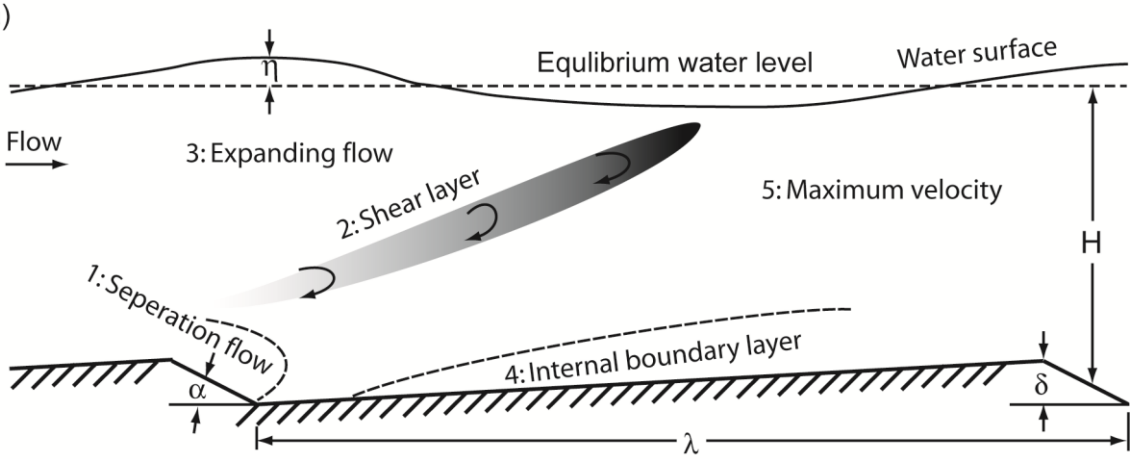

(b)

Figure 5-1. (a) A schematic diagram showing two-dimensional dunes and the delineation of flow zones. (b) A photo of eight consecutive gravel dunes built in the laboratory flume (from Attar, 2008). The dune length is $\lambda = 1.6$ m, height is $\delta = 0.08$ m, and leeside angel is $\alpha = 28^{\circ}$. The sediment median grain size is $d_{50} = 10$ mm.

river discharge, with potentially disastrous consequences including severe channel erosion and loss of infrastructure and land. Thus, studies of dune dynamics are of engineering relevance.

Previous studies have dealt with mostly dunes in sandy-bed rivers. In fact, dunes with sediment size $d_{50} > 2$ mm are also present in gravel-bed rivers (Carling and Shvidchenko, 2002), which behave differently from sandy-bed rivers. However, gravel dunes have not been studied adequately. The purpose of this study is to investigate near-bed flow structures and to further establish new ways to link the bed shear stress (τ_b) to near-bed flow for efficient flow and bedload computations.

For completeness, we describe the research progress with regard to sand dunes. Their dimensions are thought to be related to the depth of flow (Allen, 1968) as well as τ_b (Gill, 1971; Fredsoe, 1982; Yalin, 1972; van Rijn, 1982). The maximum crest heights depend on the depth of flow (Raudkivi, 1998, p. 78). Mierlo and de Ruiter (1988) obtained detailed turbulent flow measurements over fixed dunes. More recent progress in understanding sand dune dynamics has been summarised in a review paper by Best (2005). Since 1990, extensive experimental investigations have been carried out regarding the interaction between dune bedform and flow (Bennett and Best, 1996; Lyn, 1993; Nelson *et al*., 1993; Kadota and Nezu, 1999; Venditti and Bennett, 2000), sediment bedload (McLean *et al*., 1999c), suspended load (Venditti and Bennett, 2000) and vortex characteristics (Kadota and Nezu, 1999). The results from previous studies show complex dune bedform patterns, turbulence characteristics and mean flow features. As schematically shown in Figure 4.1a, the flow field over a dune length can be divided into five principal regions. The separation and shear layer regions are considered to be

important sources for turbulence production. The maximum turbulent kinetic energy occurs around the separation region, and the maximum shear stress takes place over the crest and just downstream of the reattachment point. The experimental results and field observations are proven to be useful for the development and verification of numerical models for river dune applications.

A review of the literature shows some advances in numerical modelling of flow over dunes and associated morphological evolution. The models vary in level of complexity from direct numerical simulations (Shimizu *et al*., 2001), large eddy simulations (Stoesser *et al*., 2008; Yue *et al*., 2006) and solutions to the Reynolds-averaged Navier-Stokes equations (Yoon and Patel, 1996). A number of models (Giri and Shimizu, 2006; Shimizu *et al*., 2009; Niemann *et al*., 2011) have incorporated a sediment transport component for the initiation and evolution of bedform, but their applications have been limited to dunes in sandy-bed rivers, with sediment mean grain sizes of 1 mm or smaller. Like general CFD models, the complex models mentioned above are impractical to implement on the field scale (Giri and Shimizu, 2006; Rameshwaran *et al*., 2011). This is for two simple reasons: Firstly, they incur prohibitively high computational costs. Secondly, they are data-hungry. The lack of sufficient and quality data for input and verification for the scales of interest inevitably limits their applications.

Gravel dunes and mixed sand-gravel dunes have been observed in natural rivers (Carling, 1996; Kleinhans, 2001; Radecki-Pawlik *et al*., 2006; Wilbers and ten Brinke, 2003) and laboratory flumes (Kleinhans, 2001; Carling *et al*., 2005). According to Wilbers and ten Brinke (2003), in addition to flow strength, sediment grain size controls the growth and decay of dunes and armouring of the bed surface retards the growth. This

is in contrast to the field finding of Carling (1996) that grain size is not a major control preventing dune-growth in coarse sediment. Field observations have led to the development of some relationships for determining dune dimensions, migration rate and even bedload transport. We caution that these relationships are empirical and site-specific. Kleinhans (2001) argued that sediment transport and deposition in sand-gravel rivers strongly depend on dune development: specifically, the historic sorting of sediments on the leeside of dunes and selective deposition in dune troughs. It can be seen that there are uncertainties in the results about gravel dunes.

On the basis of historic data compiled in Carling (1999), gravel dunes are reported to have a length in the range of less than 0.6 m to greater than 100 m and a height of less than 0.1 m to 16 m; gravel dunes have been developed in laboratory flumes in median grain sizes d_{50} up to 28.6 mm and in the field in d_{50} up to 60 mm. For gravel dunes to develop, two hydraulic conditions are considered to be necessary: (a) the Froude number, Fr, is a range up to 0.75, and (b) the Shields parameter, θ, ranges from 0.1 to about 0.3. Qualitatively speaking, incipient dunes develop during near-threshold conditions of fluid motion (Carling *et al*., 2005) and reach their maximum height at $\theta = 2.5$ (Carling, 1999). The Shields parameter is defined as $\theta = \tau_b[(s-1)\rho g d_{50}]^{-1}$, where s is the specific weight of bed sediments, ρ is the density of water, and g is the gravitational acceleration.

The question is how to accurately determine flow-induced τ_b in a computationally efficient manner; this issue is important to modelling dune dynamics. In this modelling study, we will address the issue using the multi-layer modelling approach. For the first instance, we will consider fixed gravel dunes and compute the flow field using a three-dimensional hydrodynamics model. The computations are efficient because there is no

need to explicitly deal with turbulent quantities such as Reynolds stress and turbulence kinetic energy, and therefore the modelling approach is suitable for implementation on the field scale. We will further derive τ_b using a number of methods (turbulent eddy viscosity, quadratic shear law and the law of the wall) and discuss their suitability. The results will be verified by comparing computed velocity profiles as well as τ_b values with new ADV measurements (Attar, 2008).

In the following, the ADV measurements will briefly be described. Details about the modelling theory and simulation conditions will be provided. The linkage between τ_b and near-bed flow will be introduced. The model results along with their comparisons with the measurements will be presented and discussed. Finally, conclusions will be drawn.

5.2 Experimental data

The experimental data used for comparison with numerical results are measurements of flow and shear stress over periodic fixed gravel dunes (Figure 5.1b) using a Nortek Vectrino$^+$ acoustic Doppler velocimeter (ADV). For details about the measurements, refer to Attar (2008). The measurements were made from flume experiments that were carried out in the Hydraulics Laboratory at the University of Ottawa, Canada. The flume was a 30 m long, 1.5 m wide and 0.5 m deep. Its sidewalls and bottom were made of cement and the base was constructed using aluminium. The experimental channel had a zero overall bed slope. Water was pumped from a large underground reservoir and circulated through the experimental channel.

Along the channel length, there were eight consecutive fixed gravel dunes (Figure

5.1b) built with sediments of median grain size of d_{50} = 10 mm. The dimensions of individual dunes were determined from consideration of the following factors: the depth of flow (h), channel width (b) and d_{50}. As in Mierlo and de Ruiter (1988), the fixed dunes had a length of $\lambda = 1.6$ m, a crest height of $\delta = 0.08$ m and a leeside angle of $\alpha = 28^{\circ}$ (Figure 5.1a). The accuracy of measurements is ± 1 mm for the dune dimensions and ± 0.29º for the angle. The accuracy of α is based on an analysis of error propagation from measured δ and horizontal length of the leeside. During the experiments, the average depth of flow was kept at h = 0.25 m; the accuracy of depth measurements is ± 1 mm. These values were selected on the basis of some existing graphs (Yalin, 1992) and empirical relationships (van Rijn, 1984). According to Yalin (1992), a dune length of 1.6 m corresponds to a flow depth of 0.252 m. The selected values also closely satisfy Coleman *et al.*'s (2006) criteria of $\lambda / h = 6.25$ and $h / \delta = 3$ and McLean *et al.*'s (1999a) criterion of $\lambda / \delta = 20$. The difference between Mierlo and de Ruiter (1988) and Attar (2008) is the sediment grain size; the former dealt with sand dunes, whereas the latter considered gravel dunes.

During the experiments, the discharge was kept at Q = 0.074 m^3/s. This is an estimate from the cross-sectionally averaged flow velocity and flow area. The cross-sectionally averaged flow velocity was determined from ADV measurements of mean velocity at an array of points at an upstream cross section. The accuracy of mean velocity measurements is ± 5% of measured value ± 0.001 m/s (Nortek, 2004). During the experiments, the mean velocities did not exceed 0.35 m/s. Thus, the accuracy of the mean velocity measurements is better than ± 0.0185 m/s. The accuracy of flow-depth and channel-width measurements is ± 1 mm. It can be shown that the accuracy of discharge is

better than ± 0.007 m^3/s (or better than 10% of the indicated Q value).

The upstream flow of steady depth approached the eight consecutive fixed dunes. From the 5th dune downstream, an equilibrium condition between the flow field and dune bedform was considered to be reached (Nelson *et al*., 1993; Nelson and Smith, 1989). The bed sediments were immobile during the flow experiments, which allowed detailed measurements of velocity without complication of both a migrating and changing bedform and without the difficulty of flow measurement in the presence of sediment transport. The three velocity components of flow and Reynolds shear stresses above the dune surface between the sixth and seventh crests (counting from upstream) were measured using the ADV (Attar, 2008).

The ADV was configured as follows: The sampling frequency was 200 Hz; the nominal velocity range was ± 0.3 m/s; the height of sampling volume was 5.5 cm; the sampling duration at each measurement point was 120 s. In total, 24 velocity profiles were taken along the dune centreline at a spatial interval of 0.07 m between adjacent profiles. Each profile consisted of 12 to 14 point measurements in the vertical. Measurement locations nearest to the dune surface were between 0.005 and 0.007 m above the surface.

5.3 Modelling theory and conditions

5.3.1 Hydrodynamic equations

A three-dimensional hydrodynamics model, ECOMSED (HydroQual, 2002), is used to compute free surface elevation and velocity components. Let (x_1, x_2, x_3) denote the Cartesian coordinates. The x_1-axis points toward the approach flow direction, the x_2-axis

is in the cross-channel direction, and the x_3-axis points upward. Let u_i denote the velocity component in the x_i direction. For an incompressible fluid, conservation of mass is expressed as

$$\partial u_j / \partial x_j = 0 \tag{5.1}$$

where the subscript j is standard tensor notation. The horizontal momentum equation is given by

$$\frac{\partial u_i}{\partial t} + \frac{\partial (u_i u_j)}{\partial x_j} = -\frac{1}{\rho}\frac{\partial p}{\partial x_i} + \frac{\partial}{\partial x_3}(K_m \frac{\partial u_i}{\partial x_3}) + F_i \tag{5.2}$$

where t is time, p is pressure, K_m is a coefficient for turbulent momentum mixing, and F_i is the horizontal mixing term. Since the average depth of flow (h = 0.25 m) is smaller than the horizontal length scale (dune length $\lambda = 1.6$ m) by an order of magnitude, as an approximation, the vertical momentum equation may be reduced to the hydrostatic pressure relation: $\partial p/\partial x_3 = -\rho g$.

5.3.2 Turbulence closure

Equation (5.2) contains parameterised Reynolds stress. The coefficient K_m is obtained by appealing to a second order turbulence closure scheme of Mellor and Yamada (1982). Let $q^2/2$ denote the turbulence kinetic energy and L denote the turbulence macro-scale (as opposed to turbulence micro-scale). The coefficient is given by $K_m = LqS_m$, where S_m is a stability function. For water of constant density, S_m is a constant (= 0.41). For more details, refer to Mellor and Yamada (1982).

In the horizontal, all of the motions not directly resolved by model grid are

parameterised as horizontal mixing, expressed as $F_i = \partial[A_m(\partial u_i/\partial x_j + \partial u_j/\partial x_i)]/\partial x_j$, and A_m is a coefficient. Its values are chosen to allow sufficient smoothing for numerical stability but at the same time to avoid excessive damping of the resolved flow structure. A_m should vary in order to maintain a uniform grid Reynolds number; in this regard, the scheme by Smagorinsky (1963) is good. The coefficient is given by $A_m = (C_s\Delta)^2(S_{ij}S_{ij})^{1/2}$, where C_s is a constant ($0.1 < C_s < 0.24$), Δ is the grid size in the horizontal, and S_{ij} is the resolved strain rate, defined as $S_{ij} = 0.5\ (\partial u_i/\partial x_j + \partial u_j/\partial x_i)$.

5.3.3 Boundary conditions

Kinematic conditions are specified on channel sidewalls and at the free water surface as well as the fixed dune surface. The sidewalls are assumed to be fully slippery, where the velocity normal to them is zero. At the free surface $x_3 = \eta(x_1, x_2)$ (Figure 5.1a), fluid particles are assumed to remain there all the time, mathematically expressed as

$$\partial\eta/\partial t + u_i\partial\eta/\partial x_i - u_3 = 0 \tag{5.3}$$

At the dune surface $x_3 = -H(x_1, x_2)$ (Figure 5.1a), there is no advective or diffusive flux through it, formulated as

$$u_i\partial H/\partial x_i + u_3 = 0 \tag{5.4}$$

Equations (5.3) and (5.4) are used to determine u_3 at the free surface and dune surface.

Dynamic condition is specified at the dune surface. A slip boundary condition is assumed, and a quadratic bottom friction is applied.

$$\left\langle \tau_{b1}, \tau_{b2} \right\rangle = \rho c_D \left| \left\langle u_{b1}, u_{b2} \right\rangle \right| \left\langle u_{b1}, u_{b2} \right\rangle \tag{5.5}$$

where τ_{bi} is the bed shear stress in the x_i direction, c_D is a dimensionless drag coefficient, and u_{bi} is velocity component nearest the dune surface. This coefficient depends on the roughness elements of the dune surface, given by

$$c_D = \kappa^2 / \ln^2 \left(0.5 \Delta h_b / z_\circ \right) \tag{5.6}$$

where κ is the von Karman constant ($\kappa = 0.41$), and Δh_b is the bottom layer thickness, and z_o is related to the size of the roughness elements of the dune surface. The parameter z_o is calibrated from model runs. The coefficient c_D is calculated from equation (5.6), but its minimum value is set to the literature value of 0.0025.

At the upstream boundary, distributed volume fluxes are specified such that they give a prescribed velocity structure and total discharge. At the downstream boundary, either water level is specified or a cyclic condition on velocity is used. The treatment of the downstream boundary should ensure insignificant reflection of disturbances from the boundary.

5.3.4 Computational techniques

For a better representation of the wavy dune surface (Figure 5.1b; Figure 5.2a), the σ coordinate, defined by $\sigma = (\eta - x_3)/(\eta + H)$, is used in the vertical. Some of the advantages are that both the dune surface and the free surface are transformed into coordinate surfaces, and therefore boundary conditions can be implemented more realistically at these coordinate surfaces than at the Cartesian coordinates. Introducing a

new set of independent variables associated with the σ coordinate requires the transformation of all the equations and relationships. The free surface is located at $\sigma = 0$, and the dune surface at $\sigma = -1$ (Figure 5.2b).

Using the multi-layer approach, the water column between the two surfaces is divided into multiple layers (Figure 5.2b). For the k'th layer, the layer-averaged velocity $\overline{u}_i$ is defined by $\overline{u}_i = (\sigma_{k+1} - \sigma_k)^{-1} \int_{\sigma_k}^{\sigma_{k+1}} u_i d\sigma$. Equations for layer-averaged velocities are obtained by integrating equations (5.1) and (5.2) over the thickness of the layer.

For better computational efficiency, mode splitting techniques are applied to split the flow field into an external mode and an internal mode (Madala and Piacsek, 1977). The former is solved for depth-averaged velocity $\overline{U}_i$, whereas the latter is solved for the vertical velocity shear $\overline{u}_i - \overline{U}_i$. The flow modes and free surface are computed using finite difference techniques on structured grids. For $\overline{U}_i$, equations (5.1) and (5.2) are integrated vertically over the depth of flow. The resultant equations can be solved using a relatively small time step in order to accommodate usually fast moving surface waves. For $\overline{u}_i - \overline{U}_i$, a larger time step can be used to solve the layer-averaged equations, subtracted by the external mode. The mode splitting technique permits the calculation of the free water surface with little sacrifice in computational time by solving the volume transport separately from the vertical shear velocity. The finite difference formations employed are of second order accuracy.

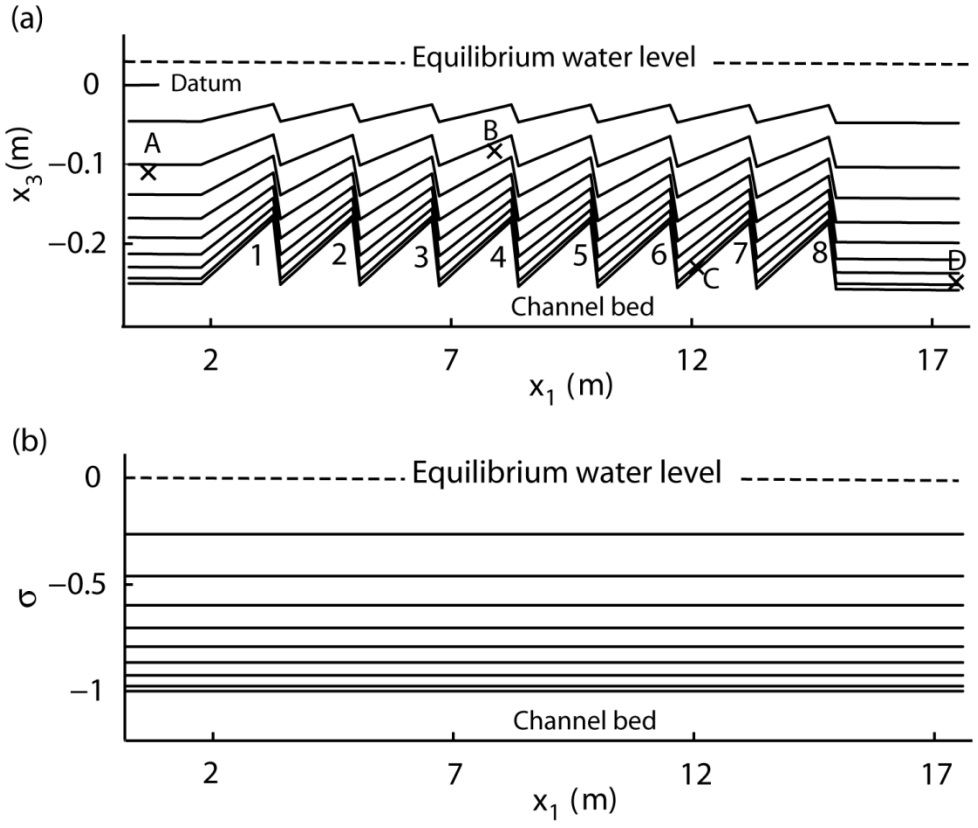

Figure 5-2 A vertical section along the channel centreline, showing the partitioning of layers: (a) in the Cartesian coordinates (the solid curves), and (b) in the σ coordinates (the solid straight lines). Every second layer is plotted. The flow is from left to right. The upstream and downstream open boundaries are located at x1 = 0 and 17.6 m, respectively. In panel (a), the channel bed contains 8 fixed dunes (marked as 1, 2, 3 …. 8); ADV measurements were made between the 6th and 7th dune crests; the symbol '×' marks four locations for which time series of velocities are extracted from model results for examination. In panel (b), the free surface and dune surface are transformed into coordinate planes.

5.3.5 Simulation conditions

Numerical simulations are setup for conditions matching the flume experiments to facilitate a comparison between predictions and measurements. These conditions, along with other control parameters used in the simulations, are summarised in Table 5.1. The conditions of dune dimensions and flow field have been explained in the Experimental Data section. Here, consideration from the perspective of numerical modelling is given. The model channel has an overall bed slope, which helps reduce end effect. This slope is estimated from the Manning's equation in such a manner that uniform flow in the channel will carry the same discharge as in the experiments; the input parameters are bed roughness and the average depth of flow used in the experiments.

Table 5-1. A summary of conditions and control parameters for model runs. The dimensions of the model channel are shown in Figures 5.2a,b.

Parameters	Value	Unit
Discharge (Q)	0.074	m^3/s
Average flow depth (h)	0.25	m
Water level η at downstream	-0.0086	m
Overall bed slope	5×10^{-4}	
Grid dimensions (x_1 and x_2 directions)	118×10	
Grid resolutions (x_1 and x_2 directions)	0.15×0.15	m
Number of σ layers	18	
Ratio of layer thickness to average flow depth	0.024 –0.137	
Time interval (Δt)	0.0004	s
Simulation period	502.4	s
Horizontal mixing coefficient (A_m)	5	m^2/s
Gravity (g)	9.81	m/s^2
Ramping period	0.4	s
Criterion for convergence	10^{-6}	

The model channel consists of three sections: a 12.8 m long section of eight consecutive two-dimensional fixed dunes, a 1.8 m long flat-bottom section upstream of the dunes, and a 3 m long flat-bottom section downstream of the dunes (Figures 5.2a,b). The total length (17.6 m) of the model channel is smaller than that of the experimental channel (30 m long), but the dune section is the same between the model and experimental channels. A reduction in length has been made to the flat-bottom sections in the model to improve computation efficiency. The presence of the upstream section is beneficial for the development of dynamically consistent flow approaching the dunes, and the downstream section is useful to minimising end effect.

The model channel is divided into 18 layers in the vertical. Since near-bed velocities are of particular interest, the layer thicknesses near the dune surface are as thin as 2.4% of the total depth of flow. This percentage corresponds to 0.005 m at the crest of the dunes. In the horizontal, the model channel is covered with finite difference grids of sufficiently fine spacing so as to resolve the expected spatial variations in the flow over dunes; uniform grids are used to avoid flow distortion.

Simulations commence from a state of rest. Initially, the free surface is given a longitudinal slope. The idea is to achieve steady state solutions faster for given upstream and downstream conditions. The upstream condition is a power-law profile of along-channel velocity that gives the same total discharge as in the experiments. This represents an improvement from the typical use of uniform flow from upstream. The time interval, ramping period and the horizontal mixing coefficient are chosen for the sake of numerical stability.

5.3.6 Bed Shear Stress

Consider the channel bed as a completely rough bed with average roughness height k_s (Figure 5.3). The bed shear stress τ_b created by the overflowing water is difficult to measure directly. However, it can indirectly be estimated using several methods: (1) energy slope, (2) Reynolds shear stress or turbulent kinetic energy, (3) the quadratic stress law, (4) a turbulent model based on the concept of eddy viscosity, and (5) the law of the wall.

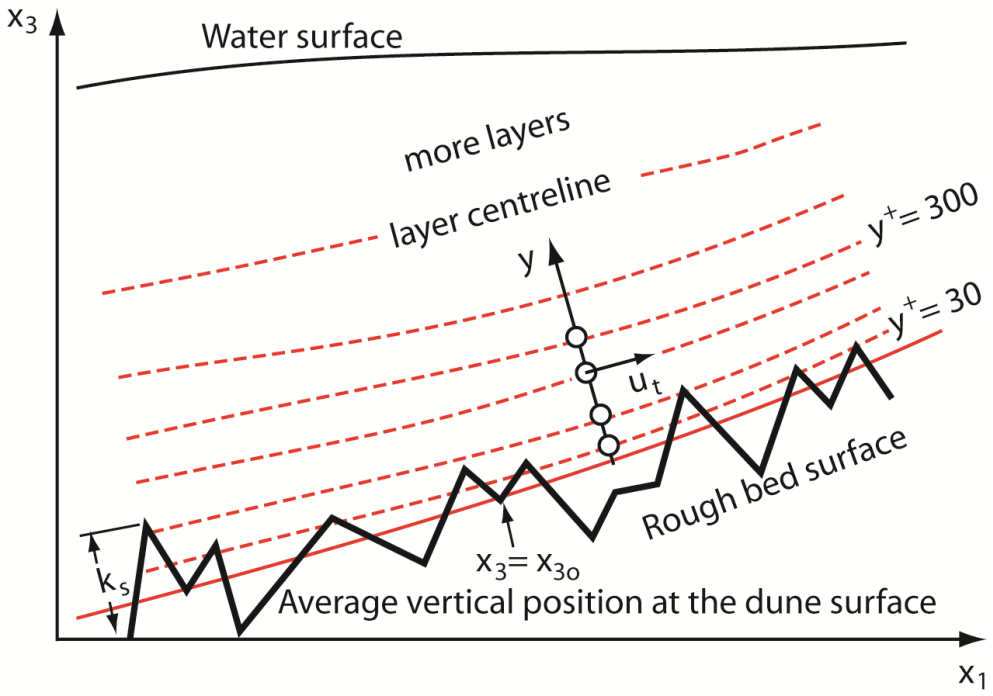

Figure 5-3. A small detailed section of a dune. The scale of the near-wall region normal to the dune surface has been exaggerated for clarity. Computations produce velocities for each layer along its centreline (the dashed lines). Within the near-wall region, the bottom layer has its centreline at $y^+ \approx 30$, and the upper most layer has its centreline at $y^+ \approx 300$.

Method 1 is commonly used to estimate reach-scale average of τ_b, assuming that the flow is approximately uniform. Since this assumption is not valid for flow over dunes, Method 1 is not useful to this study.

Method 2 for determining τ_b requires input of Reynolds shear stress or turbulent kinetic energy (Hinz, 1975, pp. 642–643). The computational costs to explicitly solve these quantities are often prohibitively high, especially on the field scale. This disadvantage makes CFD modelling impractical. In this multi-layer modelling study, the computations do not produce the turbulence quantities. Thus, Method 2 is not suitable.

Method 3 is based on classic theories for the turbulent boundary layer of flow over a completely rough bed. In this case, surface shear stress is insignificant; τ_b is due to pressure drag or form drag on the roughness elements. The bed shear stress is written as $c_D = \tau_b / (0.5\rho U_\circ^2)$, where the number 0.5 has been inserted to form the familiar dynamic pressure (Fox and McDonald, 1992, p. 438), and U_o is the freestream velocity outside the boundary layer. However, in multi-layer models, U_o is customarily replaced by the bottom layer velocity and the number 0.5 is dropped, as in equation (5.5). Note that if z_o in equation (5.6) is taken as $k_s/30$, equations (5.5) and (5.6) will yield a logarithmic velocity profile.

In Method 4, τ_b is parameterised through an eddy viscosity ν_t as (Schlichting and Gersten, 2000, p. 536)

$$\tau_b = \rho \nu_t \partial u_t / \partial y \tag{5.7}$$

where u_t is the velocity component tangential to the dune surface, and y is the normal

distance from the surface (Figure 5.3).

Method 5 is based on the logarithmic relation between the friction velocity u_* ($u_* \equiv \sqrt{\tau_b / \rho}$) and the variation of u_t with y, expressed as

$$u_t / u_* = \kappa^{-1} \ln(30y / k_s) \tag{5.8}$$

This relationship is valid for the fully turbulent near-wall region, where the wall distance ($y^+ = yu_* / \nu$, where ν is the kinematic viscosity of water) ranges from 30 to 300. This study uses $k_s = 2.5d_{50}$ (Raudkivi, 1998, p.120).

We will use the model predictions of velocity as input and evaluate τ_b using Methods 3, 4 and 5. The results will be compared.

5.4 Results

5.4.1 Equilibrium solutions

Test model runs were carried out where parameters (Table 5.1) including time interval Δt, horizontal mixing coefficient (A_m) and roughness parameter (z_o) were adjusted. In the first set of test runs, proper Δt and A_m values were determined to ensure numerical stability. In the second set of test runs, different treatments of the downstream boundary were used; the application of optimised clamp condition on water level at the boundary appeared to efficiently produce equilibrium solutions with insignificant waves/fluctuations reflected from the boundary. In other words, there are no significant errors in the results due to artificial end effects. The two sets of test runs have produced satisfactory results (not shown).

Subsequently, a set of model runs were conducted where z_o was calibrated for optimal comparison between predicted velocities and AVD data. In the range of $0.0003 \le z_\circ \le 0.1$, the model run where z_o = 0.0003 produced results closely matching the ADV data (Attar, 2008). The results for this run are discussed below. Steady state solutions were obtained by integrating equations (5.1) and (5.2) over time until the criterion for convergence (Table 5.1) is satisfied. To demonstrate the satisfaction, time series of velocity are plotted as curves in Figures 5.4a,b for four selected locations. These locations are marked by the symbols '×' and labelled as A, B, C and D in Figure 5.2a.

Longitudinally, location A is in the approach flow section upstream of the dunes, at x_1 = 0.7 m; B and C are in the dune section, at x_1 = 7.9 and 12.1 m, respectively; D is downstream of the dunes, at x_1 = 17.5 m. In the vertical, locations A, B, C and D are at σ = -0.461, -0.461, -0.952 and -0.952, respectively (Figure 5.2b). In Figures 5.4a,b, the velocity field is shown to reach the state of equilibrium after about 100 seconds of the model time. This exceeds the advection time scale of approximately 77 seconds as estimated from the channel length of 17.6 m and the depth-averaged velocity of 0.23 m/s approaching the dunes.

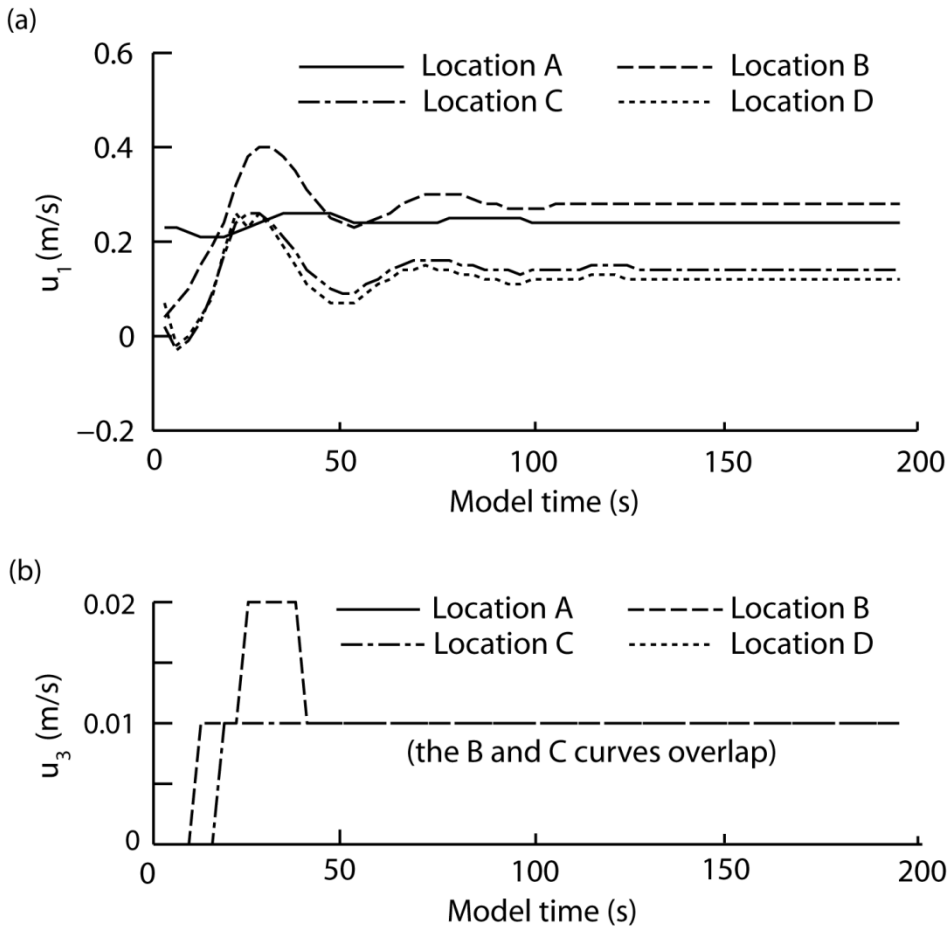

Figure 5-4. Time series of computed along-channel velocity u_1 (panel a) and vertical velocity u_3 (panel b) at the four selected locations (A, B, C and D, marked by the symbol '×' in Figure 5.2a) along the channel centreline. In panel (b), the time series for A and D overlap.

During the transient state of motions, the free water surface η fluctuates. Thus, the four locations A, B, C and D (Figure 5.2a) move up and down until the steady state is reached. Subsequently, all the four time series show equilibrium velocities (Figures 5.4a,b). This provides a benchmark for determining the required minimum time period of model runs. The equilibrium along-channel velocity u_1 is the strongest at the location B

where the flow approaches the crest, and is the weakest at locations C and D because they are in close proximity to the dune surface. Importantly, the results shown in Figures 5.4a,b imply that the implementation of the condition at the downstream boundary is appropriate; there are no significant wave reflections from the boundary back to the dune section.

As expected, the vertical velocity u_3 at locations A and D is virtually zero (Figure 5.4b), where the channel bed is flat (Figure 5.2a) and the flow is primarily in the horizontal. The vertical velocity at location B is intermittent, with amplitude of 1 cm/s, during the transient state of motions, and subsequently vanishes. The flow has an equilibrium vertical velocity of about 1 cm/s at locations B and C. Location B is in the upper water column on the stoss side of a dune. This is within the flow zone of maximum velocity (Figure 5.1a). The cross-channel velocity (not shown) is insignificant everywhere in the model channel.

5.4.2 Velocity structure

To reveal the flow development along the fixed dunes, vertical profiles of the along-channel velocity u_1 at a number of crests are compared in Figure 5.5. All the profiles show significant velocity shear in the vertical, especially near the dune surface; u_1 increases with increasing distance from the dune surface (specifically dune crests). At all the depths, the velocity profile for the second crest (the dashed-dotted curve) is plotted to the right of the profile for the first crest (the dotted curve), meaning that the flow is in a state of acceleration between the first and the second dunes.

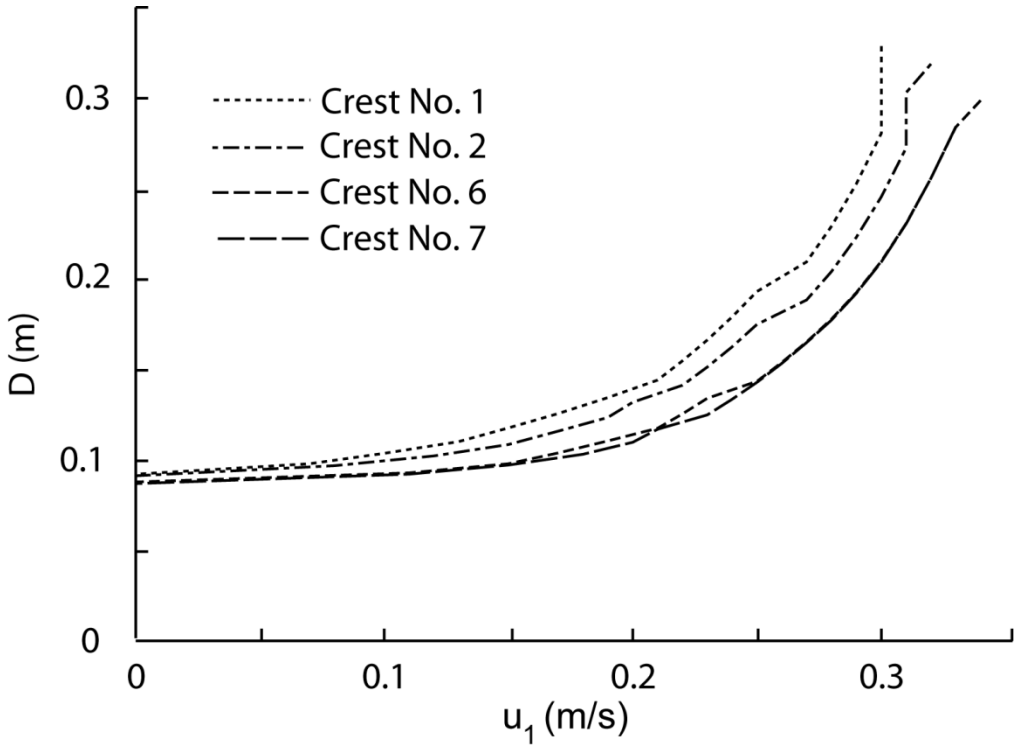

Figure 5-5. Vertical profiles of computed along-channel velocity u_1 at four selected dune crests (marked in Figure 5.2a). From upstream to downstream, the flow passes crests No. 1, 2, 6 and 7. The velocity profiles were extracted from the model results at model time of 502 s (Table 5.1). D is the vertical distance from the reference level located at 0.259 m below the equilibrium water level.

The acceleration ends as the flow passes the fifth dune, as indicated by the almost overlapping profiles at the sixth and seventh crests (Figure 5.5). If the velocity profiles of flow over two consecutive dune crests are similar, the flow over the dunes is considered as quasi-equilibrium (McLean et al., 1994; Bennet and Best, 1996). According to this criterion, the model predicts that the velocity field reaches a state of quasi-equilibrium after the fifth dune. This prediction is consistent with the results of Nelson and Smith

(1989) and Nelson *et al*. (1993), who showed the existence of a dynamic equilibrium between dune morphology and flow after the fifth dune.

In Figure 5.6, the vertical structure of the along-channel velocity at the seventh dune crest is shown to develop with model time. At the early stage of integration over time, the vertical structure oscillates to a large extent; the profiles at model times t = 50 and 80 s are seen to shift position back and forth. After model time of 100 s, the vertical structure reaches a state of equilibrium. Similar to the velocity profiles shown in Figure 5.5, the equilibrium vertical profile plotted in Figure 5.6 shows significant velocity shear, which cannot be predicted by depth-averaged hydrodynamics models with a missing dimension in the vertical. The large velocity shear near the channel bed plays an important role in bedload transport.

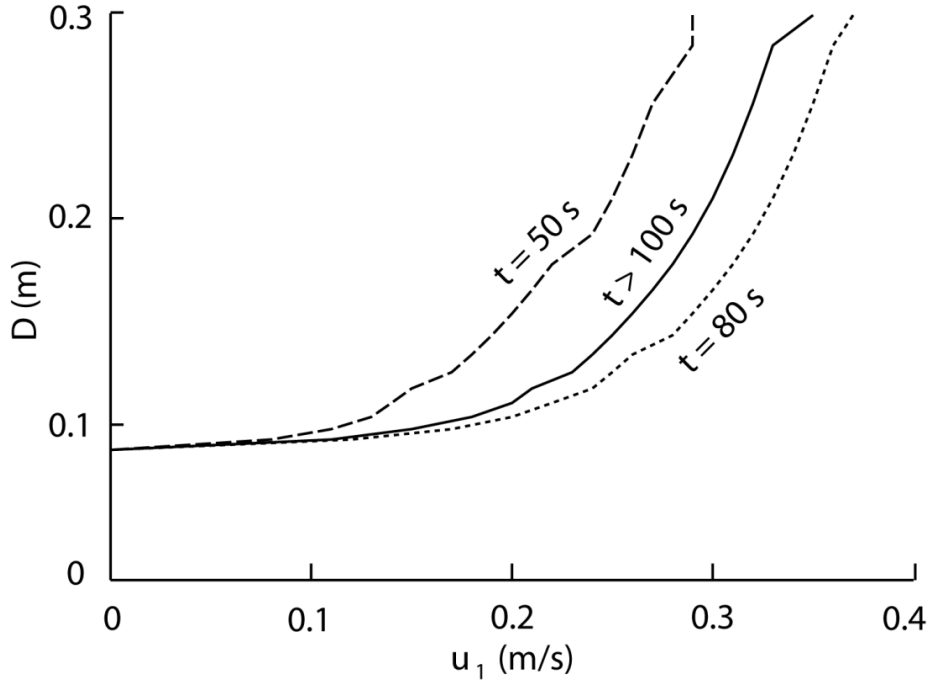

Figure 5-6. Vertical profiles of computed along-channel velocity u_1 at the seventh dune crest. D is defined in Figure 5.5.

5.4.3 Data comparison

A comparison between computed velocity profiles and the ADV data (Attar, 2008) at six selected locations is made in Figures 5.7a-f. The predicted velocities are extracted from the model solution at equilibrium for cells that are closest to the ADV locations. The ADV data of along-channel velocity are from 24 evenly spaced locations between the sixth and seventh dune crests (numbered as 6 and 7 in Figure 5.2a), the spacing being 7 cm. At each location, there are point measurements of along-channel velocity at 12 to 14 discrete depths below the surface (or elevations above the dune surface). In Figures 5.7a-f, the 12 point measurements are plotted as the symbols '+'. A number of features are clearly shown: First, the along-channel velocity increases with increasing vertical distance from the dune surface. Second, no flow reversal occurs above the crest. Lastly, the velocity shear is the most significant in the lower 17% layer of the water column. Note that the average depth of flow is 0.25 m. The data comparison is good for the stoss side (Figures 5.7d-f) and reasonable around the reattachment point (Figure 5.7c). The data comparison needs improvement for the leeside (Figure 5.7b).

Since the dune crest is known to be the most important location over a dune length with bedload implications, we examine closely the model prediction for that location. In Figure 5.8, the vertical structure of the computed along-channel velocity at $x_1 = 11.55$ m or the sixth dune crest (Figure 5.2a) is shown as the solid curve. The total depth of flow is 21.3 cm. There are no ADV data for the top 5.5 cm layer of the water column because of a distance of 5.5 cm from the ADV probe to the sampling volume. The solid curve is seen to plot through most of the ADV data points (the symbol '+'), especially in the lower water column where velocity shear is important for application to bedload calculations.

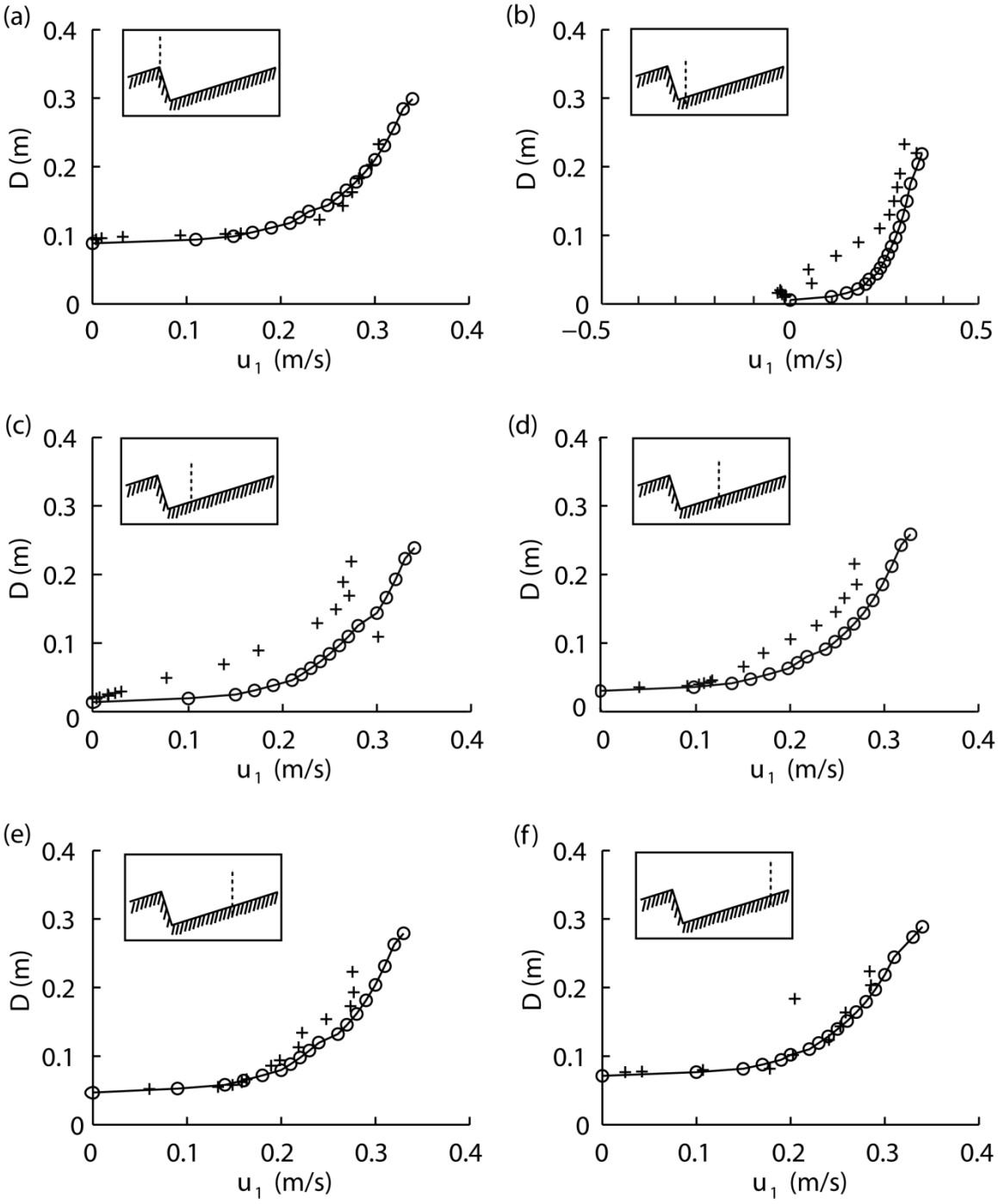

Figure 5-7. Vertical profiles of computed along-channel velocity (the solid curves with circles) at different locations between the 6th and 7th dune crests (Figure 5.2a). The corresponding ADV data are shown as the symbols '+' for comparison. The locations are marked by the dashed lines in the inserted panels. D is defined in Figure 5.5.

The data comparison shown in the figure (5.8) is acceptable. It is clear that the model has captured the observed shape of velocity profile at the crest of a dune.

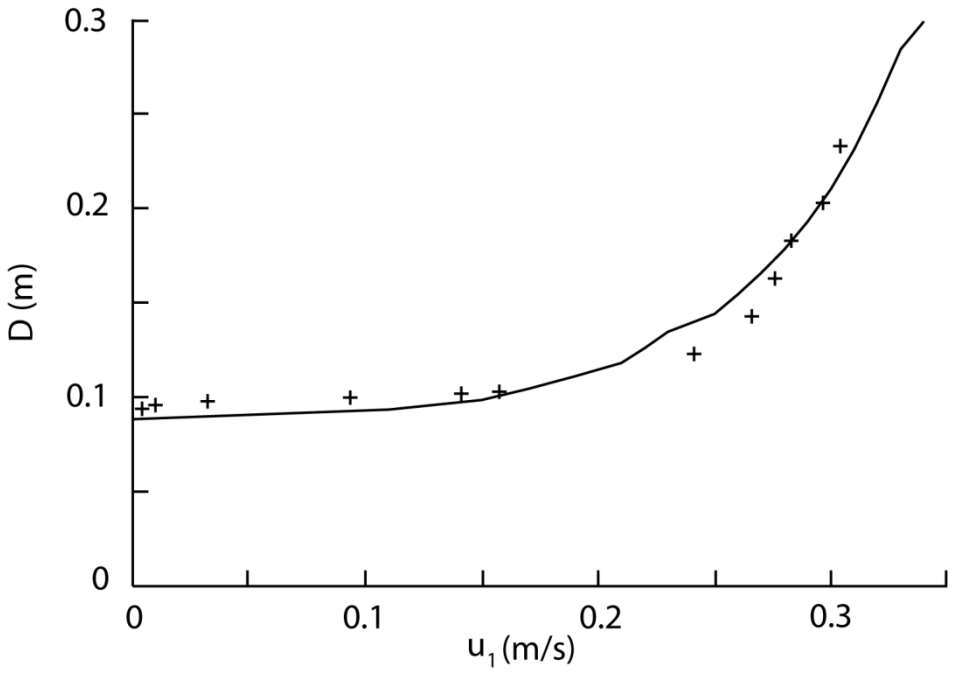

Figure 5-8. Vertical profile of along-channel velocity (the solid curve) extracted from the model results at the location of x_1 = 11.55 m or at the sixth dune crest (Figure 5.2a). ADV data of along-channel velocity (the symbol '+') from the same location are shown for comparison. There are no ADV data for the top 5.5 cm of the water column because of a distance of 5.5 cm from the ADV probe to the sampling volume. D is defined in Figure 5.5.

5.4.4 Bed shear stress

Estimating the bed shear stress τ_b using Method 3 (equation (5.5)) for requires the drag coefficient c_D (equation (5.6)) as input. Consider that the bottom layer has a characteristic thickness of $\Delta h_b = 0.006$ m, calculated as 2.4% of the average flow depth of 0.25 m, and the roughness parameter z_o takes the optimal value of 0.0003. This coefficient is c_D = 0.031. Estimates of τ_b from the model results of bottom layer velocity and the drag coefficient are presented in Table 5.2. The maximum τ_b occurs at the dune crest. If the drag coefficient is given the literature value of 0.0025, estimates of τ_b will be lower by an order of magnitude (Table 5.2).

Estimates of τ_b using Method 4 (equation (5.7)) are lower than those using Method 3, by a factor of 2 to 4. In Method 4, the eddy viscosity value of 1.3×10^{-5} (m^2/s) has been adopted from Graf and Istiarto (2002).

Table 5-2. A comparison of the bed shear stress (τ_b in N/m^2) calculated using different methods. The locations (a) to (f) match the dashed lines in the inserted panels of Figures 5.7a-f.

Locations	Method 3		Method 4	Method 5
	$c_D = 0.031$	$c_D = 0.0025$	$\nu_t = 1.3\times10^{-5}$ (m^2/s)	$k_s = 2.5d_{50}$ (mm)
(a)	0.481	0.039	0.115	0.282
(b)	0.376	0.030	0.101	0.282
(c)	0.311	0.025	0.119	0.259
(d)	0.311	0.025	0.094	0.237
(e)	0.252	0.020	0.116	0.231
(f)	0.311	0.025	0.123	0.256

Method 5 can be used for τ_b estimates by fitting tangential velocities from near-bed layers to the logarithmic profile (equation (5.8)), provided that these layers are within the wall distance range of 30 to 300. The method can also be applied to individual layers. The estimates of the friction velocity over the dune length from profile fitting and application to the fourth layer from the bed are close to each other, with a maximum difference of 3.3%; the profile fitting uses velocities from the four layers nearest the bed.

The τ_b estimates from Method 5 using velocities from the fourth layer from the bed are presented in Table 5.2. The τ_b estimates are lower by 10 to 70%, compared to the estimates using Method 3 with $c_D = 0.031$. The τ_b estimates from Method 5 are compared with the ADV measurements (Attar, 2008) of bed shear stress in Figure 5.9. Together with the results presented in Table 5.2, this comparison will show the suitability of the three methods mentioned above. The estimated τ_b values (Figure 5.9, the solid curve) are seen to plot through the ADV data points (the symbols '×', '□', '○' and 'Δ'). The ADV data are from near-bed locations at the wall distance of $171 \le y^+ \le 354$. The fourth layer from the bed is at the wall distance of $300 \le y^+ \le 324$, the average y^+ value being 313. The bed shear stress tends to intensify toward the crest of a dune and reaches the maximum there. This is similar to the sand dune results of McLean *et al*. (1999a) and van Rijn (1993, p.128). The estimates of τ_b appear to be more reliable for the stoss side of the dunes' crest than their leeside. Bedload transport is expected to be the most significant at the crest. Less accurate estimates for the leeside are perhaps not critical from the perspective of the local bedload transport. The estimated bed shear stress is in the range of 0.231 to 0.282 N/m^2 (Table 5.2; Figure 5.9), meaning that a variation of exceeding 20% over the dune length. This variation is quite significant in the case of incipient dune

development during near-threshold conditions of fluid motion.

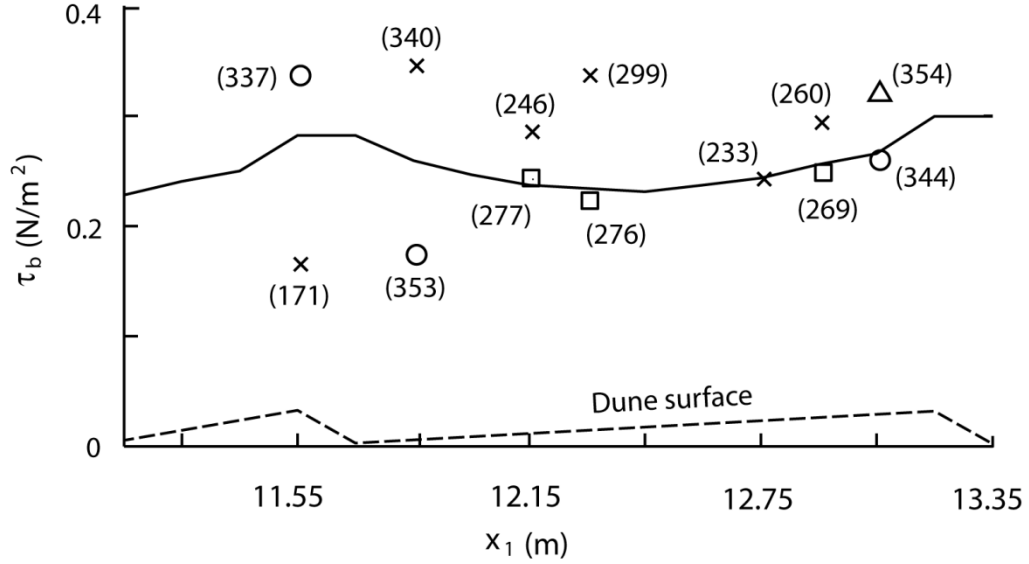

Figure 5-9. A comparison between estimated bed shear stresses from Method 5 (the solid curve) and ADV measurements of shear stress (the symbols '×', '□', '○' and 'Δ'). The dune surface is schematically shown for indentifying locations. The number in parentheses next to a symbol is the wall distance of the ADV measurement location, and the four symbols indicate that the ADV measurement locations are at normal distances of 7, 8, 9 and close to 10% of the total depth of flow from the bed, respectively.

In connection with the application of Method 5 (equation (5.8)) to the fourth layer from the bed, some sample calculations are given below. At the location of x_1 = 12.9 m (Figure 5.2a, between the crests of dune number 7 and 8), the tangential velocity at a normal distance of y = 0.0195 m (Figure 5.3, the fourth layer from the bed) from the bed surface is $(u_1^2 + u_3^2)^{0.5} \approx 0.19$ m/s. From equation (5.8), the friction velocity is implicitly determined to be $u_* = 0.016$ m/s, giving a value of 0.256 N/m^2 for the bed shear stress. To

confirm the applicability of equation (5.8) to individual layer-averaged velocities, we produce velocity profiles through back calculations using u_* implicitly solved. These velocity profiles are compared with the model output of corresponding velocity profiles in Figure 5.10. The velocity profiles are well correlated, with the correlation coefficient $\beta = 0.99$.

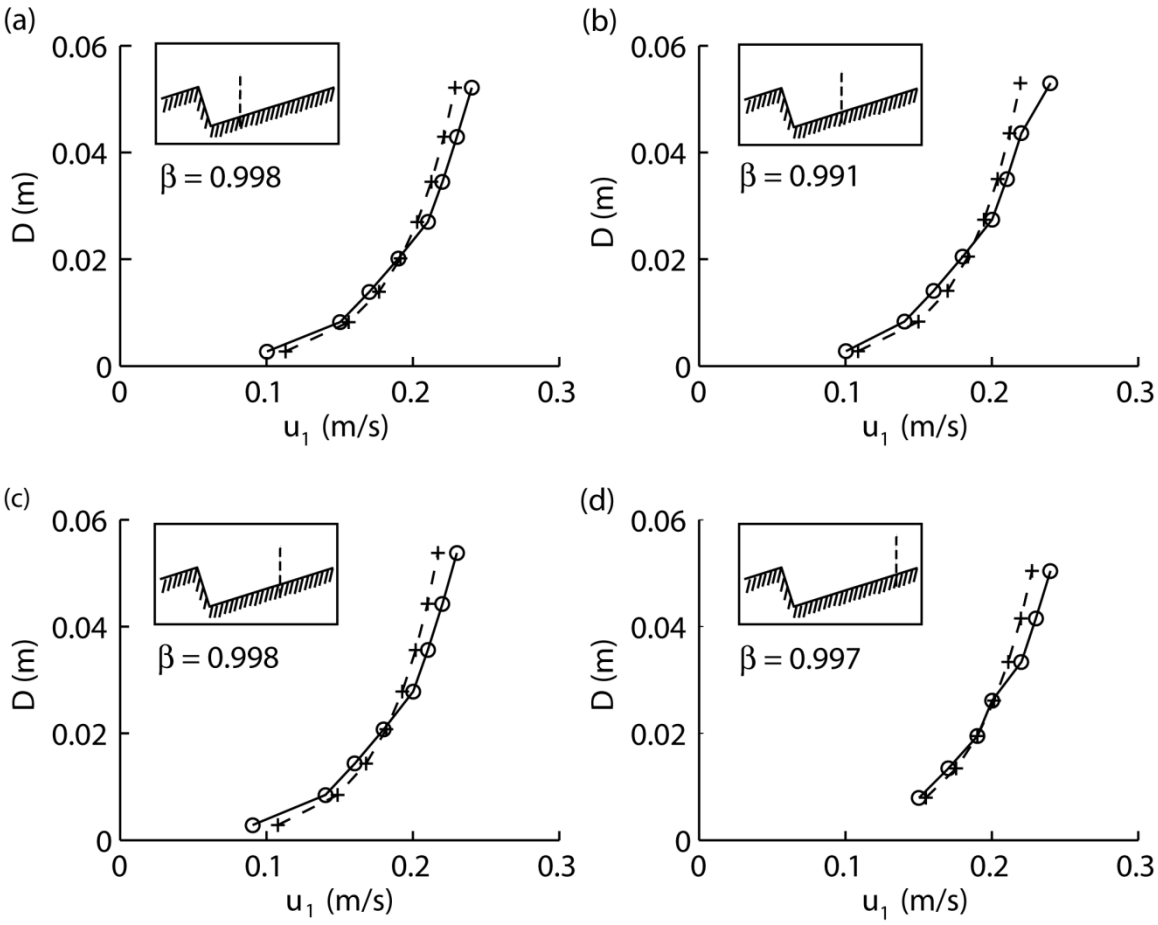

Figure 5-10. A comparison of velocity profiles between hydrodynamics model computations (open circles) and back calculations using the friction velocity (the symbol '+'). Since the focus is on near-bed flow, the profiles cover the bottom 25% of the total depth of flow. D is defined in Figure 5.5.

5.5 Discussion

After reaching the conclusion that a state of quasi-equilibrium is established after the fifth dune, we rerun the hydrodynamics model with refined grid resolutions for a shortened model channel. This model channel covers the dune section between just upstream of the sixth crest and just downstream of the seventh crest (Figure 5.2a). The purpose of the run is to understand if refined grid resolutions can improve the results for the leeside of a dune. Relevant parameters for the refined-grid-resolutions run are listed in Table5.3. In this run, the upstream boundary condition is the established flow profile from the run for which the results have been discussed in the preceding section, and cyclic condition is applied at the downstream boundary. An examination of the results for the refined-grid-resolutions run (not shown) indicates that: (a) there is a slight improvement from the results presented in Figures 5.7a-f, and (b) refining the grid is not adequate to reproduce the feature of leeside flow separation and its resultant eddy motions downstream of the dune crest. A possible explanation for the failure is the model limitation of assumed hydrostatic condition.

Table 5-3. Conditions of the refined-grid-resolutions model run. Other necessary parameters not listed here are the same as in Table 5.1.

Parameters	Value	Unit
Refined grid dimensions (x_1 and x_2 directions)	118×10	
Refined grid resolutions (x_1 and x_2 directions)	0.014×0.15	m
Number of σ layers	20	
Ratio of layer thickness to average flow depth	0.006 – 0.172	
Time interval (Δt)	10^{-6}	s
Simulation period	5.04	s
Horizontal mixing coefficient (A_m)	0.5	m^2/s
Ramping period	0.09	s

We are successful in predicting the flow structure and bed shear stress for the stoss side and dune crest (Figures 5.7, 5.8 and 5.9). According to Engelund and Fredsoe (1982), on the stoss side, the shear stress moves sediments uphill until they pass the crest. In an analysis of bed shear stress and bedload over dunes, McLean *et al*. (1999a) suggested that transport rates are the highest at the crest. Since numerical modelling of bedload often relates the bed shear stress to velocity distribution in the vertical, the good comparison of velocities at the crest (Figure 5.8) indicates that the modelling approach presented in this chapter is promising for an extension to bedload computations. Many models face the issue of a tradeoff between reducing spatial resolutions for the flow field and affordable computational costs. This is less problematic when the σ coordinate is used. The dune crest, being the most important region from the perspective of bedload modelling, is automatically resolved with the highest resolution in the vertical (Figure 5.2a), without extra computational costs.

The use of the quadratic shear law for determining bed shear stress (Method 3) in numerical models is computationally efficient because all the calculations are explicit, but it has the disadvantage that the drag coefficient c_D needs to be optimised. Therefore, the method is model suitable for diagnostic than prognostic use. The eddy viscosity approach (Method 4) is similar to Method 3 in terms of advantage and disadvantage. Both the drag coefficient and eddy viscosity are model parameters that depend on flow conditions. If flow data are not be available for calibration, it will be difficult to realistically estimate the parameters.

In flow models that use the logarithmic relation (Method 5, equation (5.8)) as bed shear stress condition, this condition is conventionally applied to the first nodes or cells

from the bed. In reality, velocities for some of these nodes may not be defined because of the roughness elements of the bed (Figure 5.3). This would create uncertainties in numerical results. We explore the idea to allow a minimum number of layers for the near-bed region (Figure 5.3) and produce multi-layer velocities for implementing the relation through profile fitting. The profile fitting approach has rarely been used in numerical models, although it has been used by many researchers to analyse near-bed measurements of velocity from laboratory experiments and the field. It is critical to ensure that the relation is valid and at least one velocity is defined. In this regard, we provide the following sample calculations: Take the maximum velocity of the approach flow (u_m = 0.30 m/s) as the velocity scale. The friction velocity is estimated to be $u_* = 0.015$ (m/s) from the quadratic friction law $\tau_b = c_D \rho u_m^2$, with $c_D = 0.0025$ (the literature value). For target wall distances of $y^+ = 30$ and 300, the corresponding normal distances are $y = 2.04$ and 20.4 mm (Figure 5.3). Thus, the bottom layer and the third or fourth layer from the bottom may have their centrelines at the two normal distances, respectively. Accordingly, computations provide three or four velocity data points within the near-bed region. Alternatively, this region may simply be taken as a certain percentage of the total depth of flow. Biron *et al*. (2004) and Rameshwaran *et al*. (2011) suggested 10% or lower. The main disadvantage of implementing profile fitting in numerical models is the high computational costs.

The relevance of profile fitting discussed above is not limited to modelling flow over gravel dunes. Specifically for flow over gravel dunes, we have shown that the logarithmic relation applied to an individual near-bed layer, but not to the bottom layer where velocity may be undefined in reality, successfully produces velocity profiles

closely matching the output from hydrodynamic computations (Figure 5.10). Although there are still implicit calculations of the friction velocity, but the calculation procedures are much more efficient than profile fitting, and thus, are suitable to be incorporated into numerical models for bedload computations.

There is experimental evidence that near-bed turbulence controls the initiation of defects from lower-stage plane gravel beds, which lead to incipient, low-amplitude, simple two-dimensional gravel dunes, but larger-scale, coherent turbulent structures in the outer flow are related to dune development (Carling *et al*., 2005). This supports the idea of formulating the bed shear stress from velocity above the bottom layer in the multi-layer modelling approach.

5.6 Conclusion

This chapter has described multi-layer modelling techniques useful for predicting flow structures in alluvial channels. The techniques have been successfully applied to reproduce newly available ADV measurements of flow velocity (Attar, 2008) over fixed periodic dunes. This chapter has further investigated practical ways to link bed shear stress τ_b to near-bed flow velocity such that from computed layer-averaged velocities, one can determine τ_b as input to bedload computations. The following conclusions can be drawn from this study:

1) The multi-layer modelling approach is suitable for simulations of near-bed flow hydraulics, particularly when used in conjunction with terrain-following σ coordinates. The suitability is confirmed through a favourable comparison between predictions and the ADV measurements. The success in application to the

challenging problem of flow over dunes is possibly attributed to the following advantages: The uneven bed and free water surface are transformed into coordinate planes, conditions at these boundaries are imposed in a realistic manner, and thus there are no artificial distortions to the flow field in the vicinity of the boundaries. Without modification, the techniques are applicable to problems of mobile bed hydraulics with bedload transport, although this study deals with fixed dunes.

2) In the vertical, velocity shear is the most significant within a vertical distance of slightly less than one fifth of the total depth from the bed and it drops by an order of magnitude further above the bed. This implies that turbulence activities cause significant upward transport of momentum deficit in the near-bed region. In studies of near-bed flow, one should consider spatial resolutions fine enough to resolve the near-bed region. Specifically, one must allow at least five layers to represent the near-bed region in multi-layer modelling studies. For example, on the field scale, the near-bed region is the bottom 2 m of the water column in natural rivers of 10 m deep.

3) The results of this study show that linking τ_b to near-bed flow velocity through the logarithmic law gives good results, as confirmed by a comparison with ADV measurements of Reynolds shear stress. Velocity profiles from back calculations using the logarithmic law correlate well with velocity profiles from the model output. Although the logarithmic law has been used widely to estimate resistant force in turbulent boundary layer, the linking as discussed in this chapter is a new idea. It provides reliable τ_b estimates and offers high computational efficiency when incorporated into numerical models for bedload transport and morphological change predictions.

4) The use of predicted flow velocities at a wall distance of $y^+ \approx 300$ gives consistent τ_b values. Along the dune wavelength, τ_b reaches the maximum at the dune crest, meaning this location is the most important with regards to bedload transport.

5) In the horizontal, dynamic equilibrium between dune morphology and flow field is reached after the fifth dune. This finding from the present study is consistent with those from earlier studies. It suggests that a minimum of five dune wavelengths is needed in the design of laboratory experiments of flow over dune bedform.

Chapter 6

Numerical simulations of flow and bedload transport over gravel dunes

Summary: River dunes are important bedforms. Problems associated with their development and evolutions include increased flood risks, channel erosion and damages to fish habitats. This paper deals with gavel dunes, as opposed to sand dunes on which previous studies of dune dynamics have focused. The purpose of this paper is to investigate the flow structure near the dune surface and flow-driven bedload transport. We predict the velocity field using a multi-layer hydrodynamics model. To improve computational efficiency, we parameterise flow separation on the leeside of dunes and use nested grid modelling strategies. The bed shear stress is determined on the basis of a

logarithmic relationship between the friction velocity and tangential flow velocity near the dune surface. Fractional bedload transport rates of a sediment mixture of sands and gravel are calculated using surface-based techniques. The numerical results of near-bed flow structure and associated bed shear stress are compared with new ADV measurements of good quality from flume experiments. The comparisons are acceptable. Bedload transport is shown to increase non-linearly with distance toward the dune crest and reach the maximum at the dune crest. Thus, the crest is the key location for estimates of bedload over dunes and dune migration. This implies that dune-length averaged bed shear stress is not suitable for bedload calculations. At low discharges, the bed shear stress is the limiting factor, resulting in insignificant bedload. At high discharges when the bed shear stress exceeds a threshold, the effect of sediment-grain hiding and sediment-size availability are important for bedload calculations. The relationship between discharge and bedload transport is non-linear; doubling the discharge can increase the transport rate by several orders of magnitude. This study has demonstrated selective transport and potential dune surface coarsening. In this paper, corrections to existent parameterisation of flow separation have been proposed.

6.1 Introduction

The study of sediment bedload transport in rivers is important because of its consequences for channel erosion, riverbank instability, damage to fish habitats and increase of flood risk. Bed sediments begin to move when the applied bed shear stress exceeds certain threshold values. The transport of sediments gives rise to different bedforms that may migrate along the river. It is a challenging problem to numerically

predict near-bed flow over bedforms, flow-induced bed shear stress and resultant bedload transport. The problem has not been solved in a satisfactory manner and still needs research efforts.

Dunes are known to be the most common bedform in rivers, which are highly susceptible to change during their existence. They are influential to channel sedimentation, flow resistance and channel discharge. Understandably, modelling river dunes has attracted considerable research attention (Bennett and Best, 1996; Kadota and Nezu, 1999; Lyn, 1993; McLean *et al*., 1999; Nelson *et al*., 1993; Venditti and Bennett, 2000). However, the applications have been mostly to sandy bed rivers, where the bed sediments have a simple grain size distribution relative to bed sediments of mixed sands and gravel considered in this study. Some of the modelling studies (Venditti and Bennett 2000; Shimizu *et al*., 2001; Stoesser *et al*., 2008; Yue *et al*., 2006; Yoon and Patel, 1996) have focused on only the flow over dunes, excluding bedload calculations.

Some of the modelling studies did consider bedload and dune evolution (Giri and Shimizu, 2006; Shimizu *et al*., 2009; Niemann *et al*., 2011). It is worth noting that Giri and Shimizu (2006) successfully predicted the recirculating eddies in the flow separation zone on the leeside of dunes with a non-hydrostatic model. Also, these models allow for sophisticated and presumably realistic turbulence closure. The problem is low computation efficiency. The computational costs for resolving the recirculating eddies are too high; this makes it impractical to apply the models to field conditions. Some modelling studies (Jerolmack and Mohrig, 2005; Onda and Hosoda, 2004) simply excluded the effect of flow separation on dune development. This exclusion is not

realistic, although it is the maximum shear stress at the dune crest that is the most important for bedload calculations (Mclean et al. 1999).

The purpose of this paper is to provide efficient numerical predictions of the flow field and bedload transport of a sediment mixture over the dune surface, considering the phenomenon of flow separation on the leeside of dunes. It is possible to parameterise the flow separation zone, as reported in Kroy *et al*. (2002) who investigated the wind field over aeolian sand dunes. The parameterisation greatly reduces computational efforts. Paalberg *et al*. (2007) modified Kroy *et al*'s (2002) formulation for applications to river dunes and determined relevant parameter values for a range of flow and dune conditions. In this paper, we extend the idea to deal with bedload transport of mixed size sediments.

Well-known methods for estimating sediment bedload transport over bedforms can be classified into three types: duBoys-type of equations, Schoklitsch-type of equations and Einstein-type of equations. duBoys (cited in Graf, 1984) proposed the earliest formula of bedload driven by shear stress, wrongly assuming that sediment particles move along the bottom in layers with velocities varying linearly in the downward direction. In an attempt to make a correction, O'Brein *et al*. (1933), Straub (1935) and Zeller (1963) introduced characteristic sediment coefficients as a function of grain size. Shields (1936) and Kalinske (1947) began to use modern fluid mechanics concepts for bedload estimates. The Schoklitsch-type of equations takes the so-called critical discharge as input. It is easier to obtain river discharge than shear stress, and therefore this type of equations is more practical. However, shear stress would be more relevant to use for bedload estimates; accordingly, several bedload formulae involving shear stress (see e,g. Graf, 1984; Meyer-Peter et al., 1948) have been proposed. The Einstein-type of

equations (Einstein, 1942, 1950) avoids the difficult definition of incipient motion. These bedload equations are based on the concept that the rate of deposition per unit area depends on the transport rate of sediments as well as the probability at particular time and space that hydrodynamic forces allow sediment grains to deposit, however, the rate of erosion depends on the number and properties of grains and the probability that instantaneous hydrodynamic lift force is large enough to move the grains (Yang, 1996, p. 100; Graf, 1984, p. 140).

Bedload formulae for incorporation into numerical models must be surface-based formulae. For application to a sediment mixture of different grain size, the surface-based bedload formulae proposed by Parker (1990) and Wilcock and Crowe (2003) are particularly appropriate. According to Parker *et al*. (1982) and Parker and Klingeman (1982), the coarsening of the surface layer of gravel-bed rivers during equilibrium or near-equilibrium sediment transport can act to increase the mobility of coarse particles at the expense of fine particles. Parker (1990) developed a surface-based bedload model applicable to equilibrium and non-equilibrium conditions and used field data for calibration. The model takes into account the effect of particle hiding and predicts differential transport rates for sediment fractions of different grain size, which can lead to surface coarsening. Wilcock and Crowe (2003) obtained a nonlinear relation between sand contents and dimensionless critical shear stress, recognizing that an increase in sand contents in gravel-bed channels leads to an increase in bedload transport rate. With this recognition, they proposed a bedload model and validated it using laboratory measurements of flow velocity, sediment transport and bed-surface grain size distribution.

Surface gain size distribution is needed in order to use the model of Parker (1990) or Wilcock and Crowe (2003). When using Parker's (1990) model, one must remove all the sand and finer materials before the determination of surface gain size distribution, because the model deals with the transport of gravel and coarser sediments only. Wilcock and Crow's (2003) model is applicable to the transport of mixed sands and gravel. In many cases, the field conditions are that the bed sediments contain significant sand contents.

In the following, methods for hydrodynamics computations, the parameterisation of flow separation, calculations of bed shear stress and estimates of bedload transport are described in Section 6.2. Then, model results are presented, along with a comparison with acoustic Doppler velocimeter (ADV) measurements from laboratory flume experiments in Section 6.3. Next, scale up to field conditions and implications to dune migration are discussed in Section 6.4. Finally, conclusions are drawn in Section 6.5.

6.2 Methods

6.2.1 Hydrodynamic computations

Consider the typical case where the depth of flow in the vertical is much smaller than the dune length in the horizontal, as illustrated in Figure 6.1, where x is the along-channel coordinate and d is the height above the dune trough. The pressure distribution will be approximately hydrostatic over the dune surface except inside the flow separation zone below the separation streamline. One wants to take the advantage of high computational efficiency of a hydrostatic model to compute the flow field outside the separation zone. For given dune geometry (Figure 6.1) and hydraulic conditions, the velocity vectors

outside the separation zone as well as the free surface elevation are calculated numerically with a multi-layer hydrodynamics model. This model is based on the principles of mass conservation and momentum balance (A.1-2). Details about the model with regard to governing equations, turbulence closure, boundary treatment, assumptions and computational procedures are given in Appendix A.

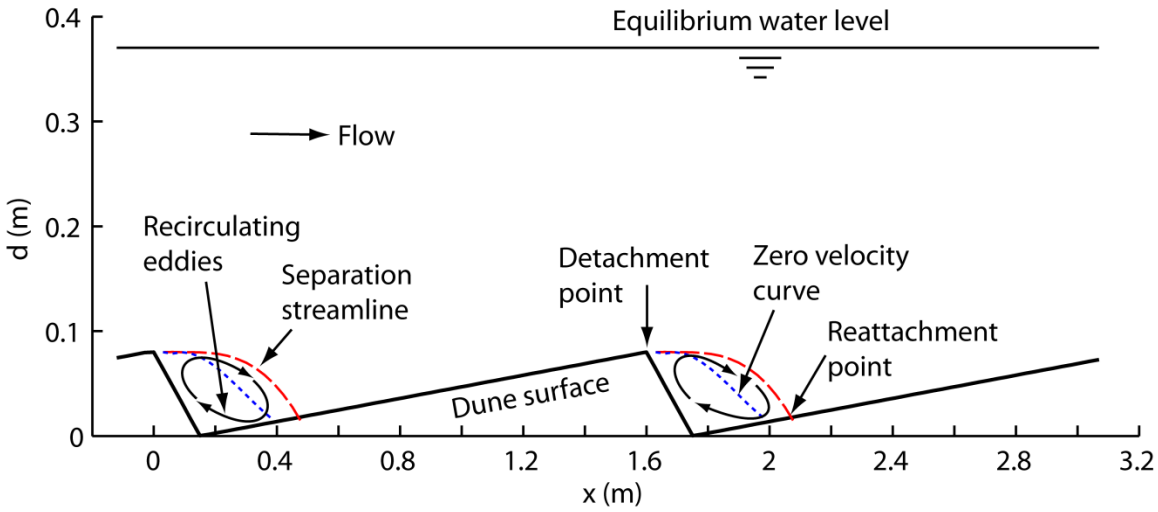

Figure 6-1. Schematic sketch of flow over consecutive dunes of triangular shape. Flow separation typically occurs on the leeside of dunes, giving rise to recirculating eddies.

The main features of the model are outlined below: The model uses the approximation of hydrostatic pressure distribution (A.3). Horizontal and vertical momentum mixing coefficients are introduced for turbulence closure (A.4-5). The horizontal mixing coefficient is adjusted for numerical stability consideration. Regarding the treatment of model channel boundaries, the sidewalls are assumed to be fully slippery, where the velocity normal to them is zero. At the free surface, fluid particles are assumed to remain there all the time (A.6). At the dune surface, there is no advective or diffusive flux through it (A.7). A slip boundary condition is assumed at the dune surface,

and a quadratic bottom friction is applied (A.8). The drag coefficient is related to a parameter linked to the size of the roughness elements of the dune surface. This parameter is calibrated from model runs. Mode splitting techniques are applied to split the flow field into an external mode and an internal mode (Madala and Piacsek, 1977). The former is solved for depth-averaged velocity, whereas the latter is solved for the vertical velocity shear. The mode splitting techniques improve computational efficiency. At the upstream open boundary, distributed volume fluxes are specified such that they give a prescribed velocity structure and discharge. At the downstream open boundary, either water level is specified or a cyclic condition on velocity is used. The treatment of the downstream boundary should ensure insignificant reflection of disturbances from the boundary.

The separation streamline (Figure 6.1) is treated as a fully slippery artificial bed in the region of flow separation for calculations of the flow field with the hydrostatic model. Along this artificial bed, the shear stress is set to zero. This treatment is consistent with the phenomenon of fluid flow separation where the shear stress is zero. Along other portion of the dune surface (Figure 6.1), the shear stress is determined from (A.8). The shape of the separation streamline depends on the dune height (the vertical distance between dune trough and crest) and the distance between the detachment and reattachment points.

6.2.2 Shape of the separation streamline

Let $S(x)$ denote the separation streamline on the leeside of dunes between the detachment point $x = x_d$ and reattachment point $x = x_{rt}$ (Figure 6.1). In this study, the detachment point is the dune crest. Following Paarlberg *et al*. (2007), we express $S(x)$ as a cubic polynomial normalised by the dune height δ

$$\widetilde{S}(\xi) = \frac{S(\xi)}{\delta} = s_3\xi^3 + s_2\xi^2 + s_1\xi + s_\circ \tag{6.1}$$

where $\xi = (x - x_d)/\delta$ is the normalised distance away from x_d, and $s_\circ$, s_1, s_2 and s_3 are coefficients.

Assuming that the separation streamline matches the elevation of the dune crest at the detachment point $x = x_d$ or $\xi = 0$, we have $s_\circ = \widetilde{S}(0) = 1$. To determine the coefficient s_1, we impose a smooth connection of the separation streamline with the dune crest at $\xi = 0$. Since the dune has a nearly horizontal bed at $\xi = 0$, we have $s_1 = d\widetilde{S}(0)/d\xi = 0$. The coefficients s_2 and s_3 are determined from the condition of the separation streamline at the reattachment point or at $\xi = 1$. The results are

$$s_3 = \tan\alpha_{rt} / L'^{\,2}_{st} + 2/L'^{\,3}_{st} \tag{6.2}$$

$$s_2 = -s_3 L'_{st} - 1/L'^{\,2}_{st} \tag{6.3}$$

where α_{rt} is the slope of the separation streamline at $x = x_{rt}$ and $L'_{st} = (x_{rt} - x_d)/\delta$ represents the length of the separation zone normalised by the dune height. These two parameters are evaluated on the basis of experimental data.

In order to make a unified comparison among various experiments, Paarlberg *et al*. (2007) considered x_{rt} as the x coordinate of the location where the cubic separation streamline (Equation 6.1) would intersect a hypothetical flat bed whose elevation is the same as the dune trough elevation. Analyses of the experimental data give $L'_{st} = 5.17$ and $\alpha_{rt} = -0.53$. One may substitute these values into Equations (6.2) and (6.3) to find the coefficients s_2 and s_3 and further determine the shape of the separation streamline using Equation (6.1).

For the dune geometry given in Attar (2008), the shape of the separation streamline is shown as the long-dashed curve (marked as 'Separation streamline') in Figure 6.1. For the same dune geometry, the separation streamline obtained according to Kroy *et al*.'s (2002) formulation has a different shape. Kroy *et al*. (2002) expressed the separation streamline as

$$\widetilde{S}(\xi) = \frac{S(\xi)}{\delta} = s_3\zeta^3 + s_2\zeta^2 + s_1\zeta + s_\circ \tag{6.4}$$

where $\zeta = (x - x_d)/L'_{st}$ is the distance away from the detachment point x_d normalised by the normalised length of the separation zone, and s_o, s_1, s_2 and s_3 are coefficients. These coefficients are determined by imposing conditions on the separation streamline at the detachment and reattachment points. Their values are follows: $s_o = 1$, $s_1 = 0$, $s_2 = -3$ and $s_3 = 2$.

For dunes with a nearly horizontal bed at the detachment point, as is the case in this study, the length of the separation zone has no influence on the coefficients in Equation (6.4) or the shape of the curve described by that equation. Paarlberg *et al*. (2007) showed experimental evidence that the curve described by Equation (6.4) is plotted through

observed zero velocity points much more closely than observed separation streamline. For this reason, in this study we consider that Equation (6.4) describes the zero velocity curve, which divides forward and backward flow of the recirculating eddies within the flow separation zone. For the dune geometry given in Attar (2008), this zero velocity curve is shown as the short-dashed curve (marked as 'Zero velocity curve') in Figure 6.1. This division curve helps contracture the flow pattern of the recirculating eddies.

6.2.3 Bed shear stress

The bed shear stress is a key input to the calculations of bedload transport. There are several methods for determining the bed shear stress, including the quadratic friction law (A.8). In the multi-layer modelling approach, the quadratic friction law is implemented using bottom layer velocities. In fact, in natural river channels with a rough bed, the bottom layer velocity may be undefined over some portion of the bed surface (Tennekes and Lumley, 1972, p. 164). In this study, we calculate the bed shear stress τ_b on the basis of the logarithmic relation between the friction velocity u_* ($u_* \equiv \sqrt{\tau_b / \rho}$, where ρ is the density of water) and the variation of tangential velocity u_t (tangential to the bed) with the normal distance y (normal to the bed). The relationship is expressed as

$$u_t / u_* = \kappa^{-1} \ln(30 y_n / k_s) \tag{6.5}$$

where κ is the von Karman constant (κ = 0.41), and k_s is the roughness height of the roughness elements of the bed surface. Equation (6.5) is valid for the fully turbulent near-wall region, where the wall distance ($y^+ = y_n u_* / \nu$, where ν is the kinematic viscosity of

water) ranges from 30 to 300. The roughness height is proportional to the median grain size d_{50} of the bed sediments as $k_s = 2.5d_{50}$ (Raudkivi, 1998, p.120).

6.2.4 Bedload transport

Bedload transport is calculated using a surface-based transport model for a sediment mixture of sands and gravel (Wilcock and Crowe, 2003). The sediment mixture is divided into a number of fractions. The model predicts fractional transport rates for a given bed shear stress τ_b and grain size distribution of surface sediments (as opposed to substrate sediments). Let D_i denote the grain size of the i'th fraction, and F_i denote the volume percentage of that fraction. A fractional transport function is defined as

$$w_i^* = \frac{(s-1)\,g\,q_{bi}}{F_i\,u_*^{\,3}} \tag{6.6}$$

where s is the specific weight of sediment, g is the gravity, q_{bi} is the volumetric transport rate per unit width of channel, and u_* is the friction velocity ($u_* \equiv (\tau_b / \rho)^{0.5}$).

Data fitting yields the following functional form for w_i^*

$$w_i^* = \begin{cases} 0.002\,\phi^{7.5} & \text{for } \phi < 1.35 \\ 14(1 - 0.894/\phi^{0.5})^{4.5} & \text{for } \phi \geq 1.35 \end{cases} \tag{6.7}$$

where ϕ is the ratio of τ_b to the reference shear stress τ_{ri} for the i'th sediment fraction. This reference shear stress is considered to depend on two factors: (a) the relative exposure of sediment grains, mathematically expressed as the ratio of D_i to the mean grain size D_{sm} of the sediment mixture; (b) the volume percentage of sands F_s of the sediment mixture.

To demonstrate the calculation procedures, we use the sand-gravel mixture data reported in Elhakeem and Imran (2012). The sediment mixture has a specific weight of s = 2.65 and an s-shape, log normal grain size distribution with D_{sm} = 1.92 mm and F_s = 38%. Firstly, the dimensionless reference shear stress τ_{rm}^* for the mean grain size is determined from

$$\tau_{rm}^* = 0.021 + 0.015e^{-20F_s} \tag{6.8}$$

To be very close to the minimum value of 0.021. Note that τ_{rm}^* increases with decreasing percentage of sands in a sediment mixture and reaches the maximum value of 0.036 for a sediment mixture without sands. Second, the reference shear stress τ_{rm} for the mean grain size is obtained from

$$\tau_{rm}^* = \frac{\tau_{rm}}{(s-1)\rho g D_{sm}} \tag{6.9}$$

With $\tau_{rm}^* = 0.021002$, ρ = 1000 kg/m^3, g = 9.81 m/s^2 and D_{sm} = 1.92 mm, we obtain $\tau_{rm} = 0.6527$ N/m^2. Third, for the i'th sediment fraction with grain size D_i, the reference shear stress τ_{ri} is calculated from

$$\frac{\tau_{ri}}{\tau_{rm}} = \left(\frac{D_i}{D_{sm}}\right)^b \tag{6.10}$$

$$\text{with } b = \frac{0.67}{1 + \exp(1.5 - D_i / D_{sm})} \tag{6.11}$$

Lastly, for a given bed shear stress τ_b, ϕ is determined as the ratio τ_b/τ_{ri} and enters Equation (6.7) to evaluate the transport function w_i^*. The volumetric transport rate per unit width of channel q_{bi} can be calculated from Equation (6.6).

6.2.5 Model runs

A total of seven hydrodynamics model runs were carried out under conditions summarised in Table 6.1. In Run 1, the model channel consists of a 12.8-m section of eight consecutive fixed dunes (Figure 6.1), a 1.8-m approach channel section L_1 upstream of the dunes and a 3-m extension section L_2 downstream of the dunes; the total length is 17.6 m. Both the approach channel section and the extension channel section have a flat bottom. Run 1 matches the flume experiments of Attar (2008) in terms of dune geometry and hydraulic conditions.

In Attar (2008), the dune length is λ = 1.6 m. The dune height is δ = 0.08 m. The leeside angle is α = 28º. The channel width is B = 1.5 m. At the equilibrium water level (Figure 6.1), the water depth at the dune trough is d_t = 25 cm (the same depth at the upstream end of the channel), and the water depth at the dune crest is 17 cm, giving an average depth of d_o = 21 cm. The discharge is Q = 0.074 m^3/s. The Froude number, define as $Fr = Q(Bd_t)^{-1}(gd_\circ)^{-1/2}$, is Fr = 0.137. The fixed dunes were built with gravel of median grain size of d_{50} = 10 mm, and the dune bedform was fixed.

For Run 1, the upstream boundary condition is a power-law profile of along-channel velocity that gives the same total discharge as in the experiments of Attar (2008). This represents an improvement from the typical use of uniform flow from upstream. The flow separation zone (Figure 6.1) is part of the hydrodynamics model domain for computations of the flow velocity and water surface elevation. Run 1 serves two purposes. The first is to achieve model calibration through a comparison between model results and the experimental data of Attar (2008). The second is to supply lateral open boundary conditions for Runs 2 throughout 7.

Table 6-1. A summary of the hydraulic and geometric parameters and conditions for model runs.

Parameter	Value						
	Run 1	Run 2	Run 3	Run 4	Run 5	Run 6	Run 7
Q (m^3/s)	0.074	0.074	0.15	0.27	0.074	0.074	0.074
B (m)	1.5	1.5	1.5	1.5	0.25	0.25	1.5
s_o	5×10^{-4}	0	0	0	5×10^{-4}	0	5×10^{-4}
Fr	0.137	0.137	0.278	0.501	0.824	0.824	0.137
N	8	2	2	2	2	2	1
$IM\times JM$	118×10	108×10	108×10	108×10	130×10	130×10	118×10
$\Delta x\times\Delta y$ (cm)	15×15	3×15	3×15	3×15	2.5×2.5	2.5×2.5	1.4×15
K_b	18	20	20	20	18	18	20
$\Delta z/h$	0.024-0.137	0.006-0.172	0.006-0.172	0.006-0.172	0.024-0.137	0.024-0.137	0.006-0.172
Δt (s)	0.0004	0.0001	0.0001	0.0001	0.00001	0.00001	0.000001
t_r (s)	0.4	0.99	0.99	0.99	0.099	0.099	0.099
T (s)	502.4	120	90.4	90.4	15.04	15.04	5.04
L_1 (m)	1.8	-	-	-	-	-	-
L_2 (m)	3	-	-	-	-	-	-
A_m (m^2/s)	5	0.5	0.5	0.5	5	5	0.5
η_d (m)	-0.0086	-	-	-	-	-	-
FSP	No	Yes	Yes	Yes	No	No	No

Note: "FSP = No" means that the flow separation zone is included in the model domain; "FSP = Yes" means that the flow separation zone is excluded in the model domain; *IM*, *JM* and *Kb* = *x*-, *y*- and *z*-direction grid dimensions; N = number of consecutive dunes; T = simulation time period; Δz = layer thickness; η_d = water level at the downstream open boundary.

For Run 2, the model channel is shortened to two consecutive dunes (Figure 6.1) for enhanced computational efficiency. At the same time, the flow separation zone is parameterised and is excluded from the model domain for hydrodynamics computations. The upstream boundary condition is a vertical profile of along-channel velocity u extracted from the results for Run 1 at the corresponding location. A cyclic condition is applied at the downstream boundary. Note that the conditions of Run 2 match the experiments of Attar (2008), and therefore the model results for this run can directly be compared with the experimental data.

For Runs 3 and 4, the conditions are the same as those for Run 2, except that the Froude number increases from 0.14 for Run 2 to 0.28 for Run 3 and to 0.50 for Run 4. The upstream boundary condition is a u profile of the same shape as that for Run 2. A cyclic condition is applied at the downstream boundary. These runs will show how Fr affects the flow over dunes and bedload transport.

For Runs 5, 6 and 7, there is no flow separation parameterisation (FSP), meaning that the flow separation zone is part of the model domain for hydrodynamics computations. The upstream and downstream boundary conditions are the same as those in Run 2. Runs 5, 6 and 7 are intended to show how sensitive the predicted flow structure is sensitive to the aspect ratio of grid resolutions in the x- and y-directions, Δx and Δy, and to grid resolutions. Note that the grids in the horizontal for Runs 5, 6 and 7 are finer than those for Runs 1 throughout 4. In addition, between Runs 6 and 5, the model channel has a horizontal bed in the former and an overall slope s_o in the latter; the idea is to reveal if the slope has any influence on the model results.

All the model runs commence from a state of rest. Initially, the free surface is given a longitudinal slope. This allows us to achieve steady state solutions faster for given upstream and downstream conditions. The time step Δt, ramping period t_r over which the approach flow grows to full strength, and the horizontal mixing coefficient are chosen for the sake of numerical stability.

6.3 Results

6.3.1 Steady-state flow and dynamic equilibrium

For all the seven runs (Table 6.1), the unsteady hydrodynamics model equations (see Appendix A) are integrated over time until steady state is reached. At each time step, iterations proceed until the criterion for convergence is satisfied. The convergence criterion is 10^{-6}. Using the hydraulic and geometric conditions listed under Run 1 in Table 6.1, a series of test runs (not numbered in Table 6.1) were carried out, where the bed roughness parameter z_o (A.8) was adjusted for model calibration. In the range of 0.3 (mm) $\leq z_o \leq$ 10 (mm), the test run with z_o = 0.3 (mm) produced velocity profiles in good agreement with the ADV data of Attar (2008).

In Run 1, because the model channel is long (covering eight consecutive dunes) relative to those in the other runs, it takes longer model time to achieve steady solutions (Figures 6.2a,b). In Figure 6.2a, we show a time series of along-channel velocity u at a representative location (near the crest of the fourth dune). The flow has an initial velocity of zero, fluctuates over time over the first 75 s of model time, and approach more or less a constant velocity after about 100 s of model time. In Run 2, the model channel is

shorter (covering two dunes), the steady state is reached quickly within 10 s of model time.

The approach of the steady state (Figures 6.2a,b) indicates that the treatment of the downstream open boundary is appropriate. For Run 1, we may interpret as water flowing through the 1.8-m approach channel section, the 12.8-m section of eight consecutive dunes and the 3-m extension channel section and then leaving the model domain through its downstream open boundary, without significant reflection of disturbances from the boundary.

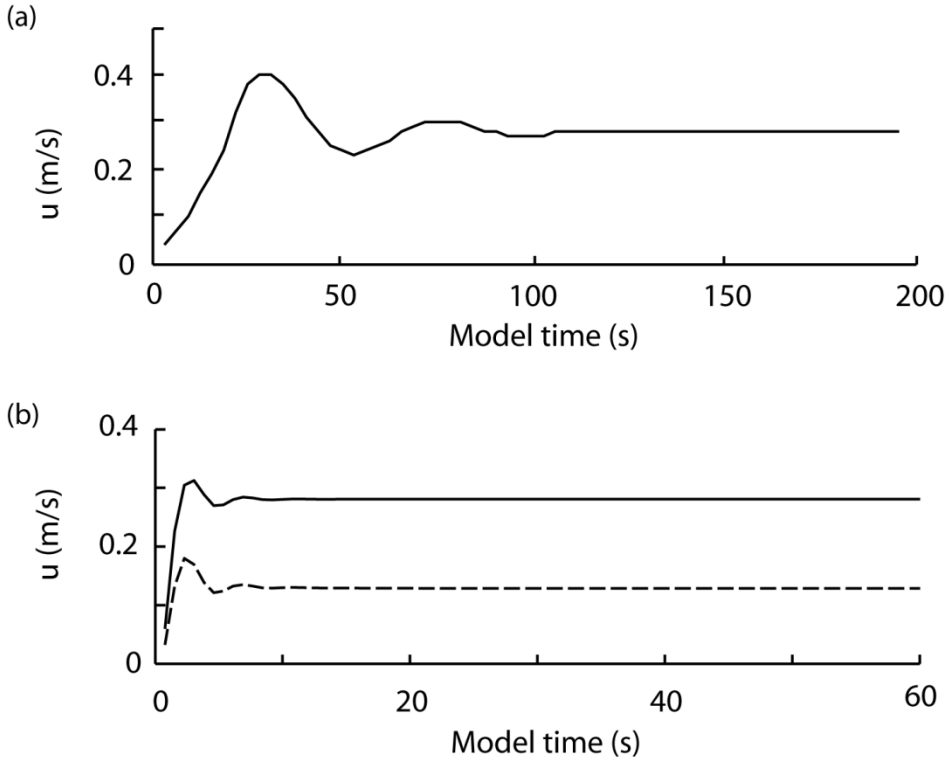

Figure 6-2. Time series of along-channel velocity u. (a) at a selected location: (x, σ) = (7.9 m, σ = - 0.461) for Run 1; (b) at two selected locations: (x, σ) = (0.48 m, -0.965) and (x, σ) = (0.48 m, -0.534) for Run 2.

It is important to note that the velocity field develops in vertical structure as water flows through the consecutive dunes. Nelson and Smith (1989) and Nelson *et al*. (1993) concluded that there exists a dynamic equilibrium between dune morphology and flow after the fifth dune. The model results for Run 1 from this study are consistent with their conclusion; after the fifth dune, vertical profiles of along-channel velocity u are virtually identical at corresponding longitudinal locations between dunes. As an example, we compare the flow velocities at the crest of the sixth dune with those at the crest of the seventh dune in Figure 6.3. At both locations, the longitudinal velocity increases from u = 0.11 m/s nearest the dune surface to u = 0.33 m/s nearest the water surface; there is no difference in the vertical structure of flow velocity.

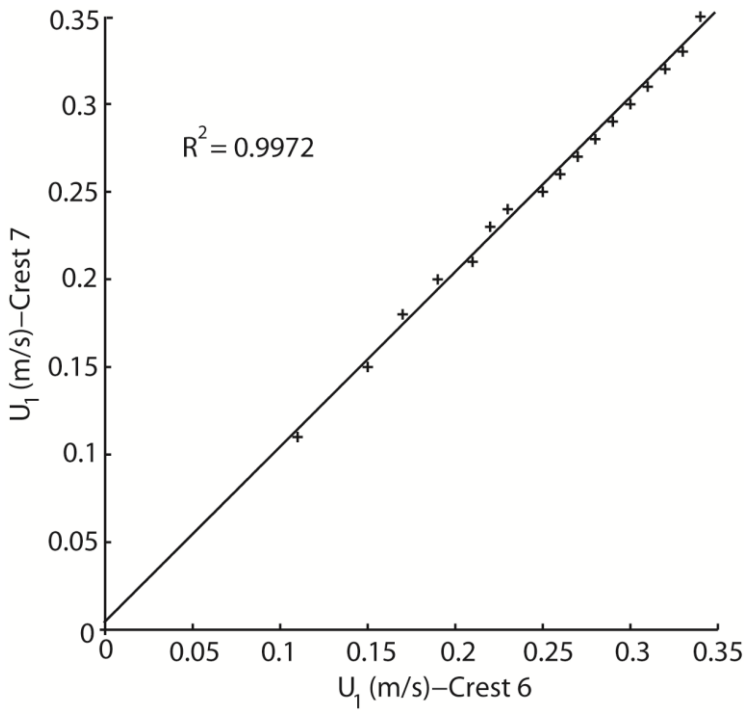

Figure 6-3. A comparison of along-channel velocity u between the sixth and seventh dune crests. The velocities are extracted from the steady-state results for Run 1.

The long (17.6 m) model channel for Run 1 accommodates the longitudinal development of flow structure, yielding a dynamic equilibrium. We take this advantage to improve computational efficiency by truncating the long model channel to a 3.2-m model channel of two consecutive dunes (Figure 6.1) for Runs 2 throughout 6 and to a 1.6-m model channel of one dune for Run 7. The upstream boundary of these truncated channels corresponds to a location just upstream of the crest of the sixth dune for Run1. The dynamically equilibrium u velocity profile for that location is extracted from the model results for Run 1, and is imposed either directly or indirectly (providing profile shape) as the condition at the upstream open boundaries of the truncated model channels for subsequent runs.

6.3.2 Velocity structure

Velocity vectors are extracted from the steady state results for Run 2 and are plotted in Figure 6.4. This plot is a vertical section along the channel centreline. No velocity vectors are plotted within the flow separation zone because it has been parameterised (Equations 6.1–6.3). The predicted flow field exhibits a number of features: a) the along-channel velocity tends to increase with an increasing distance from the channel bed, meaning that there is an equilibrium boundary layer over the dune surface; b) boundary layer velocity profiles are seen to intensify toward the dune crest; c) bottom layer velocities nearest the dune surface between the reattachment point and the crest (Figure 6.1) are small compared to those along the separation streamline. The last feature is expected because the bottom shear stress over the flow separation zone is zero.

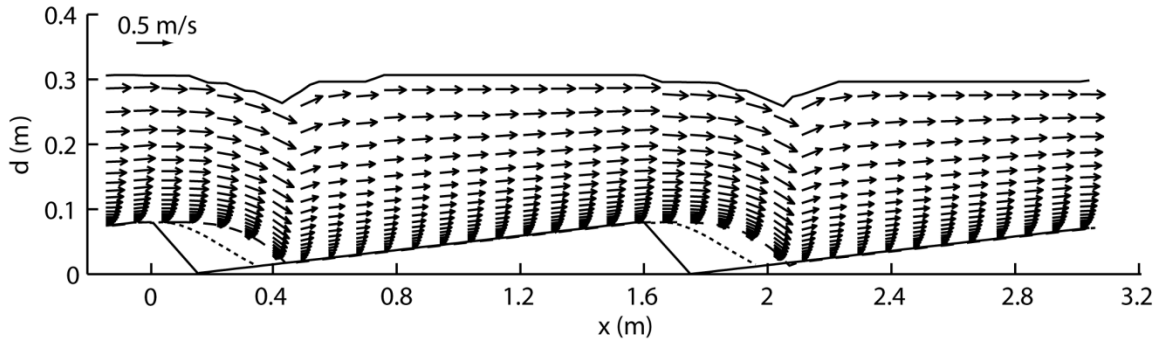

Figure 6-4. A vertical section along the channel centreline, showing velocity vectors extracted from the model results for Run 2. The model grids resolve the velocity field with 53 columns of vectors per dune length. Every third column is plotted.

6.3.3 Data comparison

In Figure 6.4, each column of velocity vectors reveals the vertical structure of along-channel velocity *u* at a location along the dune length. At six selected locations, we compare the model predictions of the *u* velocity for Run 2 with available ADV measurements (Figures 6.5a-f). The longitudinal coordinates of the locations are x = 0.61, 0.67, 0.82, 0.97, 1.18 and 1.24 m (Figure 6.4), respectively. The predicted velocities are extracted from the steady state results for Run 2 for water columns closest to the locations of six ADV profiles on the stoss side. Each of these profiles contains point measurements of the *u* velocity at 12 to 14 discrete depths below the free surface. Since the ADV measurements (Attar, 2008) and model σ layers do not coincide in vertical spacing, we include only the ADV measurements at essentially the same vertical positions as the σ layers in the comparisons. Each of the comparison panels includes 10 to 12 velocity data points (Figs. 5a-f). In some cases (panels c, e and f), the model appears to over-predict the velocity immediately above the dune surface. However, the

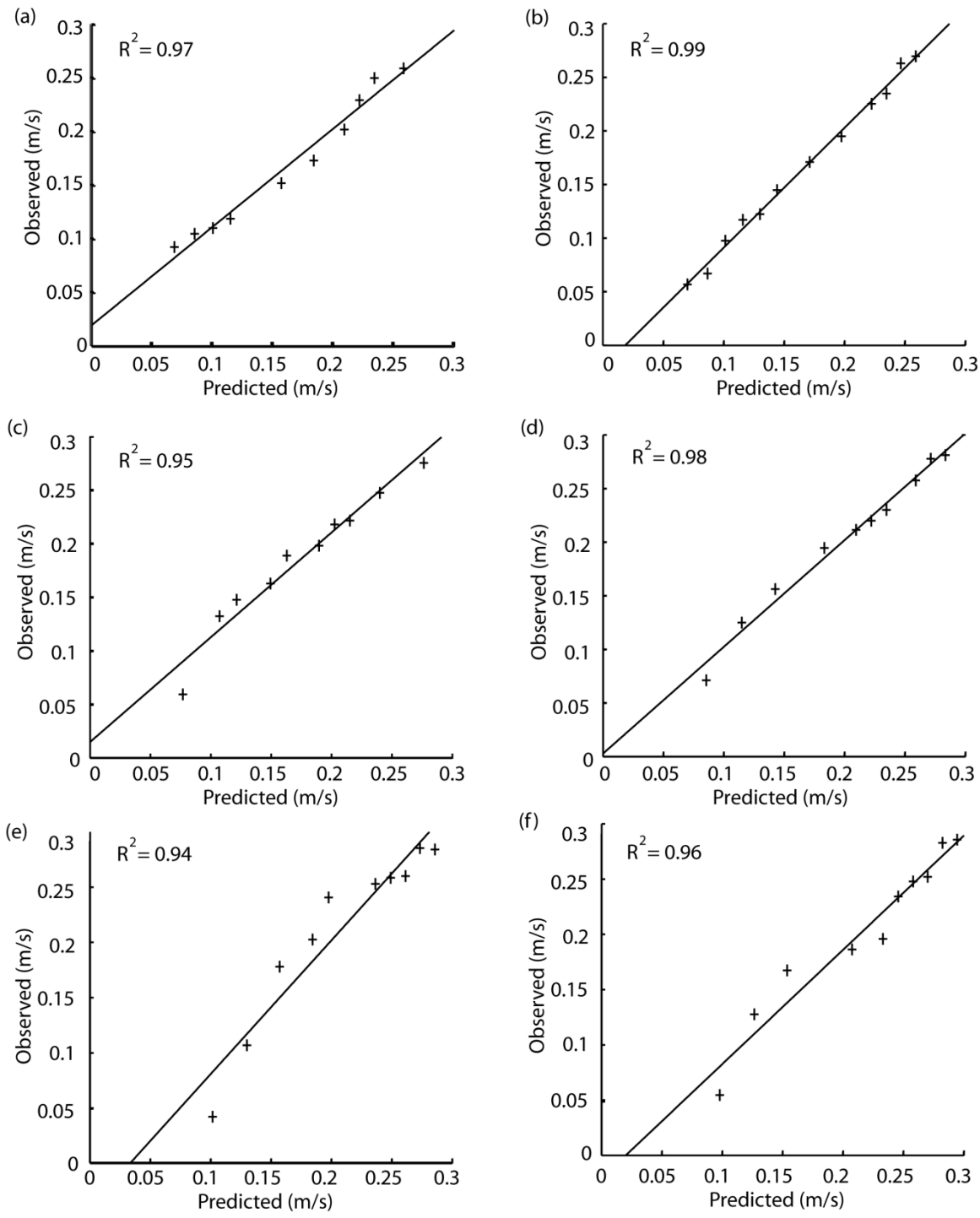

Figure 6-5. Comparisons of along-channel velocities at six selected locations between model predictions and experimental data. The experimental data are ADV measurements of mean flow velocity from flume experiments (Attar, 2008).

predictions are in very good agreement with the measurements.

The parameterised flow separation streamline intersects with the dune surface (not with a hypothetical horizontal bed) at the reattachment point (Figure 6.1). According to Equation (6.1) proposed by Paarlberg *et al*. (2007), the horizontal length between the detachment point and the reattachment point is about 44 cm, compared to 45 cm based on the ADV measurements (Attar, 2008). If Equation (6.4) proposed by Kroy *et al*. (2002) is used to determine the reattachment point, the horizontal length will be 37 cm. Thus, the length of the flow separation zone calculated from Equation (6.1) is slightly lower than the measured value. Equation (6.4) appears to underestimate the length. We propose a correction factor of 1.023 for Paarlberg *et al*.'s (2007) formulation and 1.216 for Kroy *et al*.'s (2002) formulation (Table 6.2). It is important to note that the location of the reattachment point is not sensitive to the flow condition or the Froude number.

Table 6-2. A comparison between values for the length of flow separation zone

Method	Length of flow separation zone	Correction factor	Reference
Equation (6.1)	44 (cm)	1.023	Paarlberg *et al*. (2007)
Equation (6.4)	37 (cm)	1.216	Kroy *et al*. (2002)
Experiment	45 (cm)	-	Attar (2008)

In the experiments, the reattachment point is located on the basis of velocity profiles measured at different positions in the separation zone downstream of the dune trough (Figure 6.4). Velocity profiles measured around the dune trough showed significant flow reversal near the dune surface. With an increasing distance away from the dune trough toward downstream, flow reversal became less significant. The location of the first profile that ceased to show flow reversal is taken as the approximate location of the reattachment point. Although the horizontal spacing of 7 cm between adjacent ADV

profiles prevents us to pin point the reattachment point, it was clear that a velocity profile measured at a horizontal distance of 42 cm away from the dune crest showed minimal flow reversal near the dune surface, whereas the next velocity profile measured at a distance of 49 cm away from the dune crest no longer contained any flow reversal. Further downstream, adverse pressure gradient disappeared. Between the horizontal distances of 42 and 49 cm, we estimate the length of the separation zone as 45 cm. As Paarlberg *et al*. (2007) and Kroy *et al*. (2002), we have assumed that the detachment point is the dune crest.

In this study, the friction velocity u_* is calculated using Equation (6.5) for given roughness height k_s and tangential velocity u_t at a certain normal distance y_n. The bed materials used to build the dunes in the experiments of Attar (2008) has a median grain size of d_{50} = 10 mm. The corresponding roughness height will be k_s = 25 mm. From the model results for Run 2, we extract data of flow velocity for the 13th layer below the free surface, and derive tangential velocities for estimates of u_* and the bed shear stress τ_b. A comparison between the calculated τ_b values and measured τ_b values (Attar, 2008) at a number of locations is presented in Table 6.3. The comparison is acceptable. The differences between the calculated and measured values are less than 10% for half of the locations and less than 15% for most of the locations. The reason for choosing the 13th layer is that the normal distance is in the range of 1.8 cm < y_n < 2.3 cm, and the corresponding wall distance is in the range of 242 < y^+ < 300; therefore Equation (6.5) is suitable for estimating the bed shear stress. Moreover, the measured bed shear stresses for comparison are also from the wall distance in that range for measurement.

Table 6-3. A comparison between calculated and measured values for the bed shear stress at different locations or distances from the dune crest (see Figures 6.1 and 6.4).

Distance x (cm)	61	67	82	88	97	112	118	124
Calculated τ_b (N/m^2)	0.279	0.285	0.309	0.324	0.349	0.396	0.417	0.44
Measured τ_b (N/m^2)	0.272	0.243	0.336	0.326	0.338	0.375	0.241	0.37

6.3.4 Bedload

This section presents predictions of the bedload transport of a sand-gravel sediment mixture over dunes. The sediment data reported in Elhakeem and Imran (2012) is used to demonstrate the predictions. The data (Table 6.4) is a sediment mixture of sands with grain sizes in the range of 0.25 to less than 2 mm and gravel with grain sizes in the range of 2 to 10 mm. We divide the sediment mixture into a total of nine size fractions (i = 1, 2, …, 9). An individual fraction has a median grain size D_i and a volume percentage F_i. The sediment mixture contains 62% of very fine to medium gravel and 38% of fine to very coarse sands. To predict the bedload transport rate of a sediment fraction, one needs the median grain size D_i and volume percentage F_i of that fraction as well as the bed shear stress τ_b as input to Equations (6.6) to (6.11).

The friction velocity and hence the bed shear stress is calculated from Equation (6.5) using tangential velocity at the wall distance of preferably $y^+ \approx 300$. Calculations show that $y^+ \approx 300$ corresponds to the 13th, 15th and 17th layer below the free surface for Runs 2, 3 and 4, respectively. Tangential velocities from these layers are near the bed, at a vertical distance (from the bed) of less than 10% of the local total depth of flow. In Equation (6.5), the roughness height is k_s = 4.8 mm, calculated as 2.5 times the median

grain size of the sediment mixture D_{sm} = 1.92 mm, which is derived from the grain size distribution (Elhakeem and Imran, 2012).

Table 6-4. Grain size distribution and predictions of fractional bedload transport. The sediment data is from Elhakeem and Imran (2012).

Fraction i	1	2	3	4	5	6	7	8	9
Median grain size D_i (mm)	0.25	0.44	0.89	1.44	2.04	2.87	4.06	5.53	7.9
Volume percentage F_i (%)	2.5	7.5	12	16	14.5	15	14.5	10.5	7.5
	Bedload transport rate ($cm^3/s/m$)								
Run 2 $q_{bi}\times10^7$	0.718	1.37	1.19	0.916	0.463	0.197	0.0454	0.00541	0.0004
Run 3 $q_{bi}\times10^2$	0.81	1.91	2.14	2.00	1.17	0.547	0.126	0.015	0.001
Run 4 q_{bi}	0.586	1.63	2.35	2.83	2.29	1.96	1.33	0.56	0.151

In Figures 6.6a-c, we plot distributions of the bedload transport rate along the stoss side. The reattachment point is located at x = 0.414 m and the dune crest at x = 1.6 m (Figures 6.1 and 6.4). In each of the panels (Figures 6.6a-c), there are nine curves corresponding to the nine sediment fractions. The bedload curves diverge, meaning that the transport rates are different among different sediment fractions, and the differences become more significant as it is closer to the dune crest. The most striking feature of the plots is a non-linear increase in bedload with distance toward the dune crest; this is true for all the sediment fractions and at all the discharge levels (Figures 6.6a-c, all the curves).

A comparison between Figures 6.6a and 6.6b shows that the bedload transport rates increase by a few order of magnitude in response to an increase in discharge in the model channel. Both panels show negligible bedload over the upstream half (up to x = 1.22 m) of the stoss side; they also show insignificant bedload for the coarsest sediment fraction

(fraction number 8 and 9). Possibly, this leads to dune surface coarsening. Selectively, only sands (coarse and very coarse sands) are in transport.

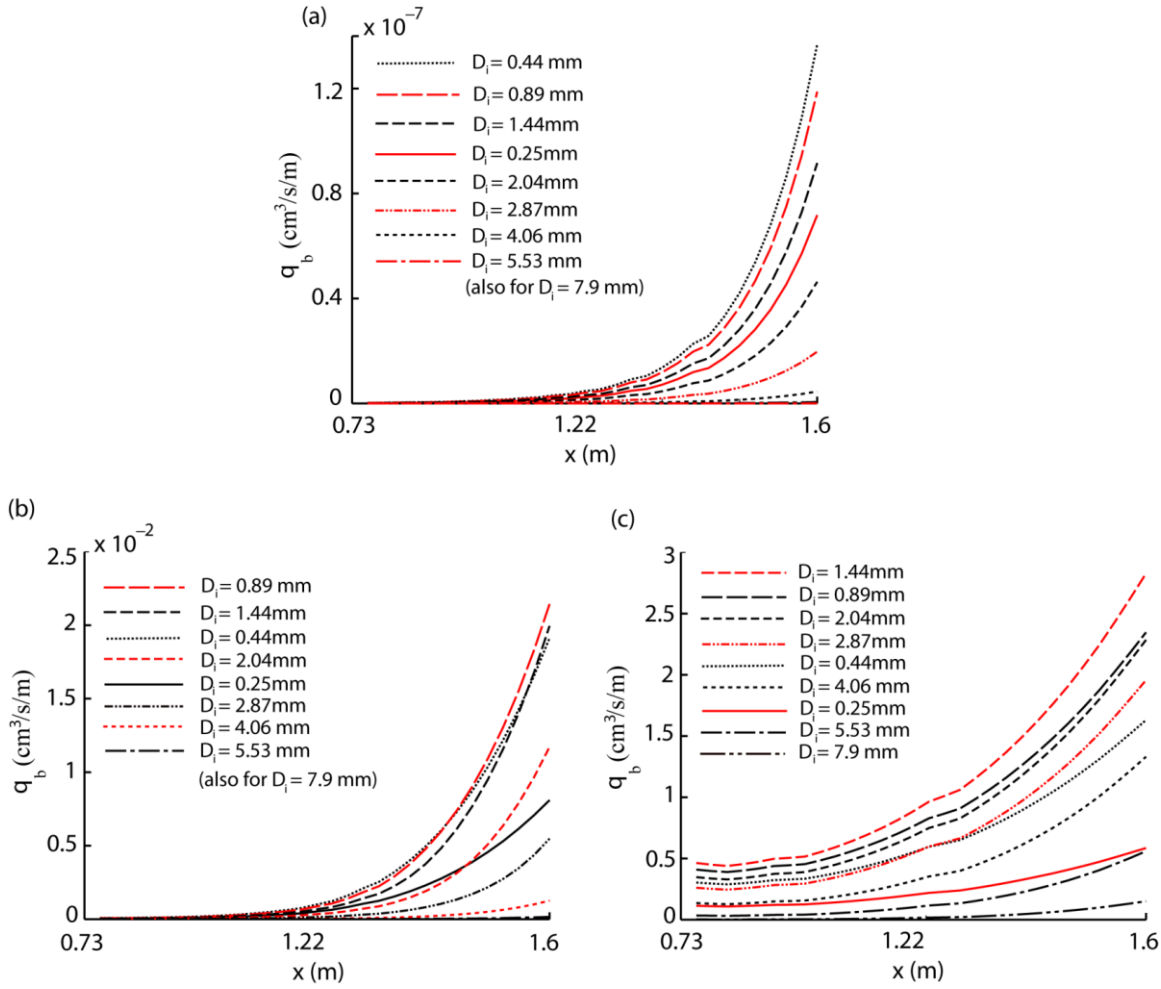

Figure 6-6. Distributions of bedload transport rate downstream of the reattachment point and the dune crest for (a) Run 2 in which Q = 0.074 m^3/s, (b) Run 3 in which Q = 0.15 m^3/s and (c) for Run 4 in which Q = 0.27 m^3/s. In (a) and (b), the bedload curves for D_i = 7.9 mm overlap with the x-axis.

The results for Run 4 (Figure 6.6c) show that the all sediment fractions participate in transport, and transport occurs over a larger portion of the dune surface. For example, the bed is mobile further upstream at the distance of x = 0.73 m in Run 4, compared to x = 1.22 m in Run 3.

A comparison between Figures 6.6a and 6.6c for fraction number 1 (the solid curve for d_i = 0.25 mm) shows that this fraction has relatively high transport rates in Run 2 but relatively low transport rates in Run 3. The explanation is that when coarse sediment grains are in transport at a higher discharge or higher resultant bed shear stress, finer grains are less exposed to the flow. The effect of hiding leads to lower transport rates for finer sediment fractions. This demonstrates the importance of using surface-based techniques for bedload predictions and considering the non-uniformity of the bed materials.

The fractional bedload transport rate q_{bi} reaches a maximum at the dune crest, true for all the runs (Figures 6.6a-c). Since the dune crest is the most important location with regard to bedload predictions, we present the maximum q_{bi} values in Table 6.4; the results indicate the following conclusions:

(1) For Run 2, the flow-induced bed shear stress is not strong enough to mobilise the bed sediments. Even the sand fractions show insignificantly low transport rates. The highest fractional transport rate per unit width of channel is $q_{bi} = 1.37\times10^{-7}$ cm^3/s/m, associated with fraction number 2. This amounts to an annual bedload of 4.31 cm^3. When all the fractions are taken into account, the annual transport per unit width is as low as 15.5 cm^3. This is a case where the applied bed shear stress (Equation 6.5) is the determining factor.

(2) When the discharge in the channel doubles from Run 2 to Run 3 (Table 6.1), the very fine gravel fractions (5 and 6) participate in transport, in addition to all the sand fractions. The sediment fractions of larger grain sizes (fraction number 8 and 9) are still immobile. The annual transport rate per unit width is 0.676 m^3 as the highest fractional transport (fraction number 3) and 2.75 m^3 when all the fractions are summed up. This represents an increase in bedload by five orders of magnitude due to doubling the discharge, which reflects the nonlinearity of bedload transport. Run 3 is a case where all the three factors, namely applied bed shear stress (Equation 6.5), material availability (F_i in Table 6.4) and relative exposure of sediment grains (Equation 6.10), play an important role in determining fractional transport rates and hence the total bedload transport. The bed materials in transport are mostly sands.

(3) Further doubling the discharge from Run 3 to Run 4 produces flow strong enough to mobilise all the sediment fractions and causes an increase in bedload by two order of magnitude, which again shows the nonlinearity of bedload transport. In terms of fractional transport, the annual transport rate per unit width is 89.2 and 72.1 m^3 as the highest among the sands fractions and among the gravel fractions, respectively. In total, the annual transport rate per unit width is 431 m^3; this consists of slightly more sands than gavel.

6.4 Discussion

Overall, the results of flow separation parameterisation (Table 6.2) and bed shear stress (Table 6.3) from this study are in reasonable agreement with ADV data from laboratory experiments (Attar, 2008). Only at the location (x = 118 m in Table 6.4), there is a large

discrepancy between the calculated and measured values for the bed shear stress. Possibly, this is attributed to uncertainties of the ADV measurements from a location very close to a rough bed. As reported in Prech et al. (2006), the sampling volume height given by the ADV software often underestimates the true, effective sampling volume height. The flow velocities very close to the bed measured by ADV can be underestimated.

In Attar (2008), the height of the sampling volume was set to 5 mm with a sampling rate of 200Hz. The accuracy of mean velocity measurements is ± 5% of measured value ± 0.001 m/s (Nortek, 2004). In the vertical, point measurements of velocity were made at a 2 mm space interval to cover the near-bed region. The first measurement point nearest the bed was assumed to be 5 mm above the bed. Thus, the comparisons shown in Figure 6.5 are considered to be reliable with respect to vertical positions between model results and ADV measurements (Attar, 2008); uncertainties in vertical position do not exceed 2 mm.

Numerical modelling of the flow field over dunes often encounters low computational efficiency problems and difficulties in handling disparity in motion scales. This study presents a modelling approach in which eddy motions within the flow separation zone is parameterised, the flow field is computed using a hydrostatic model. This modelling approach has the advantage of high computational efficiency and therefore is very useful for applications to field conditions; it effectively avoids some uncertainties associated with complicated turbulent modelling techniques; it is relatively simple and is shown to produce numerical results confirmed by experimental data. The parameterisation of flow separation does not affect estimates of bedload transport over

the dune crest, which is the most important location with regard to bedload transport over dunes and dune migration.

The bedload calculations and results presented in the preceding section have a number of important implications: Some earlier studies have used average bed shear stress over the dune length to determine bedload transport over dunes (Smith and Mclean, 1977; Mclean et al., 1999b). The average bed shear stress is not suitable to determine bedload transport over gravel dunes. Unlike predicting bedload over sand dunes, predicting bedload over gravel dunes must allow for fractional transport. This is because the effect of sediment grain hiding and selective transport play an important role in the transport of sediments.

6.5 Conclusion

This chapter represents an extension of previous studies of sand dune dynamics to deal with gravel dunes. The results presented in this paper include numerical predictions of flow structure and bed shear stress along with comparisons between the predictions and new ADV measurements of acceptable quality from laboratory experiments. The results also include predictions of bedload transport over the dune surface. The following conclusions can be drawn from the present study:

(1) The near-bed structure of flow over gravel dunes has been predicted using a multi-layer hydrodynamics model with flow separation parameterisation; the predicted flow structure and associated bed shear stress are in a favourable comparison with experimental data. The logarithmic relationship between the friction velocity and near-bed flow velocity gives good estimates of the bed shear stress.

(2) The following modelling strategies are useful for reducing computational efforts and improving efficiency: We predict the longitudinal development of flow over a large number of consecutive dunes using relatively coarse grids to produce the dynamic equilibrium solution for given hydraulic conditions and dune geometry. Using the equilibrium solution as boundary condition, we predict the detailed distribution of near-bed flow over the dune length using fine grids. We avoid the difficulties in explicitly modelling flow separation on the leeside of a dune through parameterisation without sacrificing the accuracy of bedload calculations.

(3) The transport of a sediment mixture of sands and gravel shows a non-linear increase with distance toward the dune crest for given hydraulic conditions and reaches the maximum at the dune crest, making the dune crest the key location with regards to estimates of bedload over the dune surface and dune migration. The implication is that dune-length averaged bed shear stress is not suitable for bedload calculations.

(4) At low discharges (Run 2) in a channel, the applied bed shear stress is the determining factor, limiting bedload transport to an insignificant level. At high discharges (Runs 3,4) when the applied bed shear stress exceeds a threshold, the relative exposure of sediment grains and their availability become important factors in bedload calculations. The relationship between discharge and bedload transport is non-linear; doubling the discharge can increase the transport rate by several orders of magnitude. In the case of high discharges (Runs 3), bedload transport is shown to be size-selective; a potential consequence is dune surface coarsening.

(5) It is necessary to introduce a correction factor to the previous formulations of flow separation parameterisation.

Chapter 7

Conclusion and recommendations for future work

7.1 Conclusion

In this doctorate research thesis, knowledge gaps with regard to near-boundary flow and its interaction with bed sediments in river channels under open-water and ice-covered conditions have been identified. It is important to fill the knowledge gaps because of their practical engineering relevance and hindrance to progress in numerical modelling of river flow and morphology. This thesis has presented analyses of field observations of flow velocity from ice-covered rivers and numerical modelling of flow structures and bedload transport along dunes in gavel-bed river channels.

For some practical purposes in river engineering, it may be sufficient for river engineers to carry out one-dimensional calculations of cross-sectionally averaged flow and water level. Although there is no need to explicitly solve variations in flow velocity or velocity structures at river cross sections, the spatial variations must be parameterised properly so as to apply the momentum and energy principles to carry out one-dimensional calculations.

For other purposes, one needs information about the vertical structure of the velocity field. Due to prohibitively high computational costs, it is often not feasible to explicitly resolve the bottom boundary layer in numerical modelling of river flow. As a result, the riverbed is traditionally treated as a slippery boundary, whereas its resistance to the overlying flowing water is parameterised through a drag coefficient.

In this thesis, the analyses of a large volume of field observations have produced results of energy, momentum and drag coefficients for the parameterisation of velocity structures. These results are new contributions to the permanent literature.

This thesis has contributed to the establishment of an appropriate link of the bed shear stress to near-bed flow structure for calculations of bedload transport in gravel-bed river channels. The traditional approach has been to link the bed shear stress to the so-called ‘bottom-layer velocity’. This approach is applicable to a relatively smooth riverbed (e.g. sandy-bed rivers), but not to gravel riverbed because rough elements can be so large that the ‘bottom-layer velocity’ is undefined. The link is based on the well-established logarithmic law, but the method for using it for numerical modelling is novel.

It is notoriously difficult to predict the transport of a sediment mixture in river channels. Complication factors include the relative exposure (to water flow) of sediment

grains of different sizes, changes in availability of various grain sizes, and feedback to the near-bed flow field. This thesis has demonstrated efficient modelling strategies for the case of bedload transport over dunes in a gravel-bed channel. The major findings from this doctorate research thesis are:

1) Using multi-layer modelling techniques, in conjunction with terrain-following σ coordinates, we have successfully reproduced acoustic Doppler velocimeter measurements of flow velocity over consecutive dunes. Dune morphology and flow field are shown to reach a dynamic equilibrium after the fifth dune. Velocity shear is the most significant within a vertical distance of nearly one fifth of the total depth from the channel bed; velocity shear drops by an order of magnitude further above it. These findings have implications to the design of experiments of flow over dunes as well as the development of numerical modelling strategies.
2) The use of nested model grids and flow separation parameterisation in the modelling of flow over consecutive dunes offers high computational efficiency, relative to the use of existent complicated models and general CFD models, and therefore is particularly suitable for implementation to field conditions. This research has produced a correction factor to existent formulations of flow separation streamline.
3) It has been shown that bed shear stresses calculated using the logarithmic relationship agree well with the ADV measurements, when the logarithmic relationship uses tangential velocities at the wall distance of $y^+ \approx 300$ as opposed to velocities from the bottom layer. The logarithmic relationship has produced more consistent results than the quadratic shear law and the eddy viscosity approach.

4) One can improve the accuracy of calculated bed shear stresses using the logarithmic relationship by allowing a minimum number of layers for the near-bed region. When using the multi-layer modelling approach, we propose to allow at least five layers to represent the near-bed region with the wall distance of $y^+ \leq 300$.

5) The bed shear stress has been shown to reach the maximum at the dune crest along the dune length, and thus this location is the most important with regard to calculations of bedload transport and dune migration. The implication is that dune-length averaged bed shear stress is not suitable for bedload calculations. The transport of a sediment mixture of sands and gravel non-linearly increases with distance toward the dune crest. By parameterising flow separation, one can avoid the difficulties to explicitly resolve eddy motions on the leeside of dunes without sacrificing the accuracy of bedload calculations.

6) At low discharges in a channel, the applied bed shear stress is the determining factor, and limits bedload transport to an insignificant level.

7) At high discharges when the shear stress exceeds a threshold, the relative exposure of sediment grains and their availability become important factors in bedload calculations. The relationship between discharge and bedload transport is non-linear. Bedload transport is size-selective, with the potential to result in dune surface coarsening.

8) Although the vertical structures of streamwise flow velocity in ice-covered rivers vary from river sections to river sections, the vertical structures can approximately be described by a two-layer universal function containing three parameters: two exponents and one coefficient. The exponents are associated with the frictional

effects of ice and riverbed, whereas the coefficient is related to per-unit width discharge. This function is useful for estimates of shear stress near the solid surfaces and incorporation into numerical models.

9) At river sections covered with smooth ice, the ratio of the maximum to averaged velocity is approximately 1.356, and the locations of the velocity maxima are closer to the ice than to the riverbed. One may this ratio to reduce field efforts for the purpose of determine winter discharges in ice-covered rivers.

10) For ice-covered rivers, the energy coefficient (α) and momentum coefficient (β) have average values of 1.23 and 1.08, respectively. These represent corrections of 18% and 8.3% to the literature values. The drag coefficient (c_D) ranges from 0.0035 to 0.0045 for the riverbed and from 0.0015 to 0.0025 for ice. The shear stresses near the ice are almost twice of those near the riverbed. One needs α and β when modelling cross-sectionally averaged flow typically on the reach scale and c_D when modelling velocity structures in the vertical.

7.3 Recommendation for further study

The research has led to a number of improvements in the understanding of near-boundary flow structures and the modelling of bed shear stress and bedload transport. In future studies, we make the following recommendations:

1) Extend this research to include morphological update of the channel bed; allow spatial and temporal variations in sediment transport and channel geometry through the use of a sediment continuity equation.

2) Incorporate the newly derived equation for bed shear stress along with the bedload model equations into computer code and couple numerical hydrodynamics models with the bedload transport model.
3) Apply the modelling techniques to field conditions, which are more realistic, and investigate the effects of sediment supply as a constraint.
4) Deal with flow separation by including non-hydrostatic pressure.

References

Allen JRL. 1968. The nature and origin of bed-form hierarchies. *Sedimentology* **10**(3): 161–182.

Ashton GD. 1979. River Ice. *American Scientist* **67**(1): 38-45.

Ashton GD. 1986. *River and Lake Ice Engineering*. Water Resources Publications: Littleton, Colorado, pp. 485.

Ashworth PJ, Ferguson RI. 1989. Size-selective entrainment of bed load in gravel bed streams. *Water Resources Research* **25**(4): 627-634.

Attar S. 2008. *Investigation of gravel bed form influence on shear stress and velocity distribution*. Master's thesis, Department of Water Engineering, Isfahan University of Technology, Isfahan, Iran (in Persian, Abstract in English).

Attar S, Li SS. 2012. Data-fitted velocity profiles for ice-covered rivers. *Canadian Journal of Civil Engineering* **39**(3): 334-338. DOI: 10.1139/L2012-001.

Beltaos S. 2001. Hydraulic roughness of breakup ice jams. *Journal of Hydraulic Engineering – ASCE* **127**(8): 650-656.

Bennett SJ, Best JL. 1996. Mean flow and turbulence structure over fixed ripples and the ripple-dune transition. In *Coherent flow structure in open channel*, Ashworth PJ, Bennett SJ, Best JL, Mclelland SJ (eds): Chichester, NY; 281–304.

Best JL. 1993. On the interactions between turbulent flow structure, sediment transport and bedform development: some considerations from recent experimental research. In *Turbulence*: *Perspectives on Flow and Sediment Transport*, Clifford NJ, French JR, Hardisty J (Eds), Wiley and Sons, Kingston Hull, England, 61-92.

Best J. 2005. The fluid dynamics of river dunes: A review and some future research directions. *Journal of Geophysical Research* **110**(F4): 21–24.

Biron PM, Robson C, Lapointe MF, Gaskin SJ. 2004. Comparing different methods of bed shear stress estimates in simple and complex flow fields. *Earth Surface Processes and Landforms* **29**(11): 1403–1415.

Brayall MG. 2011. *2-D Hydraulic and Ice Process Modeling at Hay River, NWT.* Master's thesis, Department of Civil and Environmental Engineering, University of Alberta, Edmonton, Alberta, Canada.

Bui MD, Rutschmann P. 2010. Numerical modelling of non-equilibrium graded sediment transport in a curved open channel. *Computers and Geoscience* **36**(6): 792-800.

Calkins DJ. 1986. Hydrologic aspects of ice jams. Cold Regions Hydrology Symposium, American Water Resources Association, Fairbanks, Alaska, 603–609.

Carling PA. 1996. Morphology, sedimentology and palaeohydraulic significance of large gravel dunes, Altai Mountains, Siberia. *Sedimentology* **43**(4): 647–664.

Carling PA. 1999. Subaqueous gravel dunes. *Journal of Sediment Research* **69**(3): 534–545.

Carling PA, Golz E, Orr HG, Radecki-Pawlik A. 2000. The morphodynamics of fluvial sand dunes in the River Rhine, near Mainz, Germany. I. sedimentology and morphology. *Sedimentology* **47**: 227-252.

Carling PA, Richardson K, Ikeda H. 2005. A flume experiment on the development of subaqueous fine-gravel dunes from a lower-stage plane bed. *Journal of Geophysical Research-Earth Surface* **110**(F4): F04S05, DOI: 10.1029/2004JF000205.

Carling PA, Shvidchenko AB. 2002. A consideration of the dune : antidune transition in fine gravel. *Sedimentology* **49**(6): 1269–1282.

Catella M, Paris E, Solari L. 2005. 1D Morphodynamic model for natural rivers. *Proceedings 4th Conference on River, Coastal and Estuarine Morphodynamics,* Urbana, Illinois, 4-7 October, 2005.

Chow VT. 1959. *Open Channel Hydraulics.* McGraw-Hill: New York, pp. 700.

Coleman SE, Nikora VI, McLean SR, Clunie TM, Schlicke T, Melville BW. 2006. Equilibrium hydrodynamics concept for developing dunes. *Physics of Fluids* **18**(10). DOI: 10.1063/1.2358332.

Dargahi B. 2004. Three-dimensional flow modelling and sediment transport in the river Klarälven. *Earth Surface Process and Landforms* **29**(7): 821-852.

Demuren AO. 1993. A numerical model for flow in meandering channels with natural bed topography. *Water Resources Research* **29**(4): 1269-1277.

Egiazaroff IV. 1965. Calculation of nonuniform sediment concentrations. *Journal of the Hydraulic Division* – ASCE **91**(4): 225-247.

Einstein HA. 1942. Formulas for the transportation of bed load. *Transactions of the ASCE* **107:** 561-577.

Einstein HA. 1950. *The bed-load function for sediment transportation in open channel flows.* U.S. Department of Agriculture. Washington, D.C. Technical Bulletin No. 1026.

Elhakeem M, Imran J. 2012. Density function for entrainment and deposition rates of nonuniform sediment. *Journal of Hydraulic Engineering – ASCE* **138**(7): 591-609.

El Kadi Abderrezzak K, Paquier A, Gay B. 2008. One-dimensional numerical modelling of dam-break waves over movable beds: application to experimental and field cases. *Environmental Fluid Mechanics* **8**(2): 169-198.

El Kadi Abderrezzak K, Paquier A. 2009. One-dimensional numerical modeling of sediment transport and bed deformation in open channels. *Water Resources Research* **45**(5): W05404.

Engelund F, Fredsoe J. 1982. Sediment ripples and dunes. *Annual Review of Fluid Mechanics* **14**: 13–37.

Ettema R, 2002. Review of alluvial-channel responses to river ice. *Journal of Cold Regions Engineering – ASCE* **16**(4): 191-217. DOI: 10.1061/(ASCE)0887-381X(2002)16:4(191).

Ferguson RI, Parsons DR, Lane SN, Hardy RJ. 2003. Flow in meander bends with recirculation at the inner bank. *Water Resources Research* **39**(11): 1322. DOI: 10.1029/2003WR001965.

Fox RW, McDonald AT. 1992. *Introduction to Fluid Mechanics*, 4th ed. Willey: New York, pp. 615.

Fredsoe J, 1982. Shape and dimensions of stationary dunes in rivers. *Journal of the Hydraulics Division – ASCE* **108**(HY8): 932–947.

Gill MS, 1971. Height of sand dunes in open channel flows. *Journal of the Hydraulics Division – ASCE* **97**(HY12): 2067–2074.

Giri S, Shimizu Y. 2006. Numerical computation of sand dune migration with free surface flow. *Water Resources Research* **42**(10). DOI: 10.1029/2005WR004588.

Graf WH. 1984. *Hydraulics of sediment transport.* Water Resources Pubs: Colorado, pp. 513.

Graf WH, Istiarto I. 2002. Flow pattern in the scour hole around a cylinder. *Journal of Hydraulic Research* **40**(1): 13–20.

Healy D, Hicks FE. 2004. Index velocity methods for winter discharge measurement. *Canadian Journal of Civil Engineering* **31**(3): 407-419. DOI: 10.1139/L04-001.

Hinz JO. 1975. *Turbulence*, 2nd ed. McGraw-Hill: New York, pp. 790.

Hoque MA. 2009. *Hydraulic Analysis of Ice-covered River Flow.* Master's thesis, Department of Building, Civil & Environmental Engineering, Concordia University, Montreal, Quebec, Canada.

HydroQual. 2002. *A Primer for ECOMSED*. Mahwah, NJ.

Jackson RG. 1976. Sedimentological and fluid-dynamic implications of the turbulent bursting phenomenon in geophysical flows. *Journal of Fluid Mechanics* **77**(3): 531-560.

Jerolmack DJ, Mohrig DC. 2005. A unified model for subaqueous bed form dynamics. *Water Resources Research* **41**(W12421). DOI: 10.1029/2005WR004329.

Kadota A, Nezu I. 1999. Three-dimensional structure of space-time correlation on coherent vortices generated behind dune crest. *Journal of Hydraulic Research* **37**(1): 59–80.

Kalinske AA. 1947. Movement of sediment as bed load in rivers. *Transactions of the American Geophysical Union* **28**(4): 310-317.

Kennedy JF. 1969. The formation of sediment ripples, dunes and antidunes. *Annual Review of Fluid Mechanics* **1**(1): 147–168.

Klaassen G. 1992. Experiments on the effect of gradation and vertical sorting on sediment transport phenomena in the dune phase. *Mitteilungen Der Versuchsanstalt Fur Wasserbau, Hydrologie Und Glaziologie an Der Eidgenossischen Technischen Hochschule Zurich* **117:** 127-145.

Kleinhans MG. 2001. The key role of fluvial dunes in transport and deposition of sand-gravel mixtures, a preliminary note. *Sedimentary Geology* **143**(1–2): 7–13.

Kroy K, Sauermann G, Hermann HJ. 2002. Minimal model for aeolian sand dunes. *Physical Review E* **66**(031302): 1-17.

Lacey RWJ, Roy AG. 2008. The spatial characterization of turbulence around large roughness elements in a gravel-bed river. *Geomorphology* **102**(3–4): 542–553.

Lai CJ, Yen CW. 1993. Turbulent free surface flow simulation using a multilayer model. *International Journal for Numerical Methods in Fluids* **16**(11): 1007-1025.

Lane SN, Hardy RJ, Elliott L, Ingham DB. 2004. Numerical modeling of flow processes over gravelly surfaces using structured grids and a numerical porosity treatment. *Water Resources Research* **40**(1): W01302.

Langendoen EJ, Simon A, Thomas RE. 2001. CONCEPTS-a process-based modeling tool to evaluate stream-corridor restoration designs. *In Wetlands Engineering & River Restoration Conference Proceedings, ASCE*. Donald FH (ed.), 27-31 August, 2001.

Langendoen EJ, Thomas RE, Bingner RL. 2002. Numerical simulation of the morphology of the Upper Yalobusha River, Mississippi between 1968 and 1997. In *River Flow* 2002*, Proceedings of the International Conference on Fluivial Hydraulics,* Louvain la Neuve, Bousmar D, Zech Y. (eds); 931-939, 4-6 September, 2002.

Larsen PA. 1969. Head losses caused by an ice-covered open channel. *Journal of the Boston Society of Civil Engineers* **56**(1): 56-57.

Lau YL. 1982. Velocity distributions under floating covers. *Canadian Journal of Civil Engineering* **9**(1): 76-83.

Lau YL, Krishnappan BG. 1981. Ice cover effects on stream flows and mixing. *Journal of the Hydraulic Division – ASCE* **107**(10): 1225-1242.

Lau YL, Krishnappan BG. 1985. Sediment transport under ice cover. *Journal of Hydraulic Research* **111**(6): 19791-19808.

Li SS. 2012. Estimates of the Manning's coefficient for ice-covered rivers. *Proceedings of the Institution of Civil Engineers – Water Management* **165**(9): 495-505.

Lopez JL, Falcon MA. 1999. Calculation of bed changes in mountain streams. *Journal of Hydraulic Engineering – ASCE* **125**(3): 263-270.

Lyn DA. 1993. Turbulence measurements in open-channel flows over bedforms. *Journal of Hydraulic Engineering – ASCE* **119**(3): 306–326.

Madala RV, Piacsek SA. 1977. A semi-implicit numerical model for baroclinic oceans. *Journal of Computational Physics* **23**(2): 167–178.

Matthes GH. 1947. Macroturbulence in natural stream flow. *Transactions, American Geophysical Union* **28**(2): 255-265.

McLean SR, Nelson JM, Wolfe SR. 1994. Turbulence structure over two-dimensional bed forms: Implications for sediment transport. *Journal of Geophysical Research* **99**(C6): 12729–12747.

Mclean SR, Wolf SR, Nelson JM. 1999a. Prediction boundary shear stress and sediment transport over bed forms. *Journal of Hydraulic Engineering* **125**(7): 725-736.

Mclean SR, Wolf SR, Nelson JM. 1999b. Spatially averaged flow over a wavy boundary revisited. *Journal of Geophysical Research* **104**(C7): 15743-15753.

McLean DG, Church M, Tassone B. 1999c. Sediment transport along lower Fraser River – Measurements and hydraulic computations. *Water Resources Research* **35**(8): 2533–2548.

Mekonnen M, Dargahi B. 2007. Three dimensional numerical modelling of flow and sediment transport in rivers. *International Journal of Sediment Research* **22**(3): 188-198.

Mellor GL, Yamada T. 1982. Development of a turbulence closure model for geophysical fluid problems. *Reviews of Geophysics and Space Physics* **20**(4): 851–875.

Meyer-Peter E, Müller R. 1948. Formulas for bed-load transport. *Proceedings of the 2nd Meeting of the International Association for Hydraulic Structures Research,* Stockholm, 39-64, 7-9 June, 1948.

Mierlo MCLM van, Ruiter JCC de. 1988. *Turbulence measurements above artificial dunes*. Delft Hydraulics, Delft, The Netherlands, Report No. TOW A55 Q789.

Morse B, Hamai K, Choquette, Y. 2005. River discharge measurement using the velocity index method. In *13th Workshop on the Hydraulics of Ice Covered Rivers*, Hanover, NH, 15-16 September 2005.

Morvan H, Pender G, Wright NG, Ervine DA. 2002. Three-dimensional hydrodynamics of meandering compound channels. *Journal of Hydraulic Engineering – ASCE* **128**(7): 674-682.

Muller A, Gyr A. 1986. On the vortex formation in the mixing layer behind dunes. *Journal of Hydraulic Research* **24**(5): 359-375.

Myers RH. 1990. *Classical and modern regression with applications*. 2nd edition, PWS-KENT: Boston, MA.

Nelson JM, McLean SR, Wolfe SR. 1993. Mean flow and turbulence fields over two-dimensional bed forms. *Water Resources Research* **29**(12): 3935–3953.

Nelson JM, Smith JD. 1989. Mechanics of flow over ripples and dunes. *Journal of Geophysical Research* **94**(C6): 8146–8162.

Nicholas AP, Smith GHS. 1999. Numerical simulation of three-dimensional flow hydraulics in a braided channel. *Hydrological* Processes **13**(6): 913-929.

Niemann S, Fredsoe J, Jacobsen N. 2011. Sand dunes in steady flow at low Froude numbers: Dune height evolution and flow resistance. *Journal of Hydraulic Engineering – ASCE* **137**(1): 5–14.

Nortek 2004. *Nortek Vectrino Velocimeter user guide*. No-1351 Rud, Norway.

O'Brien MP. 1933. Review of the theory of turbulent flow and its relation to sediment transport. *Transactions, American Geophysical Union* **14(**1): 487-491.

Olsen NRB. 2003. Three-dimensional CFD-modeling of self-forming meandering channel. *Journal of Hydraulic Engineering – ASCE* **129**(5): 366-372.

Onda S, Hosoda T. 2004. Numerical simulation on development process of dunes and flow resistance. In *River flow 2004:* **1**. *Proceedings of the Second International Conference on Fluvial Hydraulics,* Greco M, Carravetta A, Della Morte R. (eds); Balkema AA, Leiden, Netherland, 245-252, 23-25 June, 2004.

Packman AI, Salehin M, Zaramella M. 2004. Hyporheic exchange with gravel beds: basic hydrodynamic interactions and bedform-induced advective flows. *Journal of Hydraulic Engineering – ASCE* **130**(7): 647-656.

Paarlberg AJ, Dohmen-Janssen CM, Hulscher SJMH, Termes P. 2007. A parameterization of flow separation over subaqueous dunes. *Water Resources Research* **43**(W12417), DOI: 10.1029/2006WR005425.

Parker G. 1990. Surface-based bedload transport relation for gravel rivers. *Journal of Hydraulic Research* **28(**4): 417-436.

Parker G, Klingeman PC. 1982. On why gravel bed streams are paved. *Water Resources Research* **18**(5): 1409-1423.

Parker G, Klingeman PC, McLean DG. 1982. Bedload and size distribution in paved gravel-bed streams. *Journal of the Hydraulics Division – ASCE* **108**(4): 544-571.

Prowse TD. 1990. Heat and mass balance of an ablating ice jam. *Canadian Journal of Civil Engineering* **17**(4): 629-635.

Precht E, Janssen F, Huettel M. 2006. Near-bottom performance of the Acoustic Doppler Velocimeter (ADV) – a comparative study. *Aquatic Ecology* **40**: 481–492. DOI: 10.1007/s10452-004-8059-y.

Radecki-Pawlik A, Carling PA, Slowik-Opoka E, Ksiazek, L. 2006. Field investigations of sand-gravel bed forms within the Raba River, Poland. In *River Flow* 2006: **1-2**. *Proceedings and Monographs in Engineering*, *Water and Earth Sciences*, Ferreira RML, Alves CTL, Leal GAB et al. (eds); 979–984, 6-8 September, 2006.

Rameshwaran P, Naden PS. 2004. Three-dimensional modelling of free surface variation in a meandering channel. *Journal of Hydraulic Research* **42**(6): 603-615.

Rameshwaran P, Naden PS, Lawless M. 2011. Flow modelling in gravel-bed rivers: rethinking the bottom boundary condition. *Earth Surface Processes and Landforms* **36**(10): 1350–1366.

Rantz SE. 1982. *Measurement and computation of channel flow*. Water Supply Paper No. 2175. Vol. 1 and Vol. 5 of U.S. Geological Survey, Washington D.C.

Raudkivi AJ. 1998. *Loose Boundary Hydraulics*. A.A. Balkema Publisher: Rotterdam, pp. 496.

Ribberink JS. 1987. *Mathematical modelling of one-dimensional morphological changes in rivers with non-uniform sediment.* Delft University of Technology, Faculty of Civil Engineering, pp. 200.

Richardson EV, Davis SR. 2001. *Evaluating scour at bridges*. 4th ed., Federal Highway Administration, Hydraulic Engineering Circular No. 18, Virginia, USA, FHWA NHI 01-001.

Robert A. 2003. *River Processes*: *An Introduction to Fluvial Dynamics*. Arnold Publishing: London, pp. 214.

Samaga BR, Raju KGR, Garde RJ. 1986. Bed load transport of sediment mixtures. *Journal of Hydraulic Engineering – ASCE* **112**(11): 1003-1018.

Sayre WW, Song GB. 1979. *Effects of ice covers on alluvial channel flow and sediment transport processes*. University of Iowa, Iowa, pp. 96.

Schoklitsch A.1930. *Der Wasserbau: Ein Handbuch für Studium und Praxis.* Springer, Vienna, 2nd ed. English translation (1937) by S. Shulits.

Schlichting H, Gersten K. 2000. *Boundary-Layer Theory*. 8th revised and enlarged ed. Springer: Berlin, pp. 795.

Shen HT. 2003. Research on River Ice Processes: Progress and missing links. *Journal of Cold Regions Engineering – ASCE* **17**(4): 135-142.

Shen HT. 2010. Mathematical modeling of river ice processes. *Cold Regions Science and Technology* **62**(1)**:** 3-13. DOI: 10.1016/j.coldregions.2010.02.007.

Shen HT, Ackermann NL. 1980. Wintertime flow distribution in river channels. *Journal of the Hydraulics Division – ASCE* **106**(HY5): 805-817.

Shen HT, Su J, Liu L. 2000. SPH simulation of river ice dynamic. *Journal of Computational Physics* **165**(2): 752-770.

Shields A. 1936. *Anwendung der anhnlichkeitmechanik und turbulenz-forschung auf die geschiebebewegung*. Mitteilungen der Preussischen Versuchsanstalt fúr Wasserbau und Schiffbau, No. 26, Berlin, Germany (English Translation by Ott WP, Uchelon JC., California Institute of Technology, Pasadena, California, USA).

Shimizu Y, Giri S, Yamaguchi S, Nelson J. 2009. Numerical simulation of dune-flat bed transition and stage-discharge relationship with hysteresis effect. *Water Resources Research* **45**(4), W04429. DOI:10.1029/2008WR006830.

Shimizu Y, Schmeeckle MW, Nelson JM. 2001. Direct numerical simulation of turbulent over two-dimensional dunes using CIP method. *Journal of Hydroscience and Hydraulic Engineering* **19**(2): 85–92.

Shinohara K, Tsubaki T. 1959. On the characteristics of sand waves formed upon the beds of open channels and rivers. *Reports of Research Institute of Applied Mechanics* **7**(25): 15-45.

Sinha SK, Sotiropoulos F, Odgaard AJ. 1998. Three-dimensional numerical model for flow through natural rivers. *Journal of Hydraulic Engineering – ASCE* **124**(1): 13-24.

Smagorinsky J. 1963. General circulation experiments with the primitive equations. *Monthly Weather Review* **91**(3): 99–164.

Smith JD, Mclean SR. 1977. Spatially averaged flow over a wavy surface. *Journal of Geophysical Research* **82**(12): 1735-1746.

Smith BT, Ettema R. 1997. Flow resistance in ice-covered alluvial channels. *Journal of Hydraulic Engineering – ASCE* **123**(7): 592-599.

Spiegel MR, Lipschutz S, Liu J. 2009. *Mathematical handbook of formulas and tables*. McGraw-Hill, 3rd ed.: New York, pp. 289.

Steffler PM, Jin YC. 1993. Depth averaged and moment equations for moderately shallow free surface flow. *Journal of Hydraulic Research* **31**(1): 5-17.

Stoesser T, Braun C, Gacia-Villalba M, Rodi W. 2008. Turbulence structures in flow over two-dimensional dunes. *Journal of Hydraulic Engineering – ASCE* **134**(1): 42–54.

Straub LG. 1935. Missouri River report, *In-House Document 238*. *73rd Congress, 2nd Session, U.S. Government Printing Office,* Washington, DC, 1135-1156.

Teal MJ, Ettema R, Walker JF. 1994. Estimation of mean flow velocity in ice-covered channels. *Journal of Hydraulic Engineering – ASCE* **120**(12): 1385-1400. DOI: 10.1061/(ASCE)0733-9429(1996)122:8(476).

Tennekes H, Lumley JL. 1972. *A First Course in Turbulence*. The MIT Press, Cambridge, Massachusetts, pp. 300.

Thomas WA, Prashum AL. 1977. Mathematical model of scour and deposition. *Journal of the Hydraulics* Division – *ASCE* **110**(11): 1613-1641.

Tsai WF, Ettema R. 1994. Ice cover influence on transverse bed slopes in a curved alluvial channel. *Journal of Hydraulic Research* **32**(4): 561–581.

Urroz GE, Ettema R. 1994. Application of two-layer hypothesis to fully developed flow in ice-covered curved channels. *Canadian Journal of Civil Engineering* **21**(1): 101–110.

Uzuner MS. 1975. The composite roughness of ice covered channels. *Journal of Hydraulic Research* **13**(1): 79–102.

van Rijn LC. 1982. Equilibrium roughness of alluvial bed. *Journal of the Hydraulics Division – ASCE* **108**(10): 1215–1218.

van Rijn LC. 1984. Sediment transport, part II: Bed forms and alluvial roughness. *Journal of Hydraulic Engineering – ASCE* **110**(12): 1733–1754.

van Rijn LC. 1993. *Principles of Sediment Transport in Rivers, Estuaries and Coastal Seas*. Aqua Publications: Amsterdam, pp. 715.

Venditti JG, Bennett SJ. 2000. Spectral analysis of turbulent flow and suspended sediment transport over fixed dunes. *Journal of Geophysical Research* **105**(C9): 22035–22046.

Wadhams P. 2002. *Ice in the Ocean* . Gordon and Breach Science Publishers: London, pp. 351.

Walker JF. 1994. Methods for discharge under ice cover. *Journal of Hydraulic Engineering – ASCE* **120**(11): 1327-1336.

Walker JF, Wang D. 1997. Measurement of flow under ice covers in North America. *Journal of Hydraulic Engineering – ASCE* **123**(11): 1037-1040. DOI: 10.1061/(ASCE)0733-9429(1997)123:11(1037).

White KD. 2003. Review of prediction methods for breakup ice jams. *Canadian Journal of Civil Engineering* **30**(1): 89–100.

Wilbers AWE, Ten Brinke WBM. 2003. The response of subaqueous dunes to floods in sand and gravel bed reaches of the Dutch Rhine. *Sedimentology* **50**(6): 1013–1034.

Wilcock PR, Crowe JC. 2003. Surface-based transport model for mixed-size sediment. *Journal of Hydraulic Engineering – ASCE* **129**(2): 120-128.

Wooldridge JM. 2009. *Introductory econometrics: a modern approach.* South Western, Cengage Learning, 4th ed., pp.865.

Wu WM. 2008. *Computational River Dynamics*. Taylor & Francis: London, pp. 494.

Wu W, Vieira DA. 2002. *One-dimensional channel network model CCHE1D version 3.0–technical manual*. Report No. NCCHE-TR, National Center for computational Hydroscience and Engineering, University of Mississipi, Oxford, Miss.

Wu W, Rodi W, Wenka T. 2000. 3D numerical modeling of flow and sediment transport in open channels. *Journal of Hydraulic Engineering – ASCE* **126**(1): 4-15.

Xia C, Jin YC. 2006. Multilayer averaged and moment equations for one-dimensional open-channel flows. *Journal of Hydraulic Engineering – ASCE* **132**(8): 839-849.

Xia C, Jin YC. 2007. Multilayer depth-averaged flow model with implicit interfaces. *Journal of Hydraulic Engineering – ASCE* **133**(10): 1145-1154.

Yalin MS. 1972. *Mechanics of Sediment Transport*. Pergamon: Oxford, pp. 290.

Yalin MS. 1992. *River Mechanics*. Pergamon: Oxford, pp. 219.

Yang CT. 1996. *Sediment Transport: Theory and Practice.* McGraw-Hill: New York, pp. 396.

Yang CT, Huang J, Greimann BP. 2004. *User's Manual for GSTAR-1D 1.0 (Generalized Sediment Transport for Alluvial Rivers–One Dimension, Version 1.0)*. Department of the Interior, Bureau of Reclamation, Technical Service Center, Denver, Colorado.

Yoon J, Patel V. 1996. Numerical model of turbulent flow over sand dune. *Journal of Hydraulic Engineering – ASCE* **122**(1): 10–18.

Yoon JY, Patel VC, Ettema R. 1996. Numerical model of flow in ice-covered channel. *Journal of Hydraulic Engineering – ASCE* **122**(1): 19-26.

Yue WS, Lin CL, Patel VC. 2006. Large-eddy simulation of turbulent flow over a fixed two-dimensional dune. *Journal of Hydraulic Engineering – ASCE* **132**(7): 643–651.

Zeng J, Constantinescu G, Weber L. 2008. A 3D non-hydrostatic model to predict flow and sediment transport in loose-bed channel bends. *Journal of Hydraulic Research* **46**(3): 356-372.

Zhu J. 1992. *An introduction and guide to the computer program FAST-3D*. Report No. 691, Institude for Hydromechanics, University of Karlsruhe, Germany, pp. 98.

Appendix A

Governing equations of the hydrodynamics model

A three-dimensional hydrodynamics model (ECOMSED) developed by HydroQual (2002) is used to compute the velocity field and free surface elevation. Let (u, v, w) denote the velocity components in the Cartesian coordinates (x, y, z). The equation of continuity is expressed as

$$\frac{\partial u}{\partial x}+\frac{\partial v}{\partial y}+\frac{\partial w}{\partial z}=0 \tag{A.1}$$

The horizontal momentum equations are given by

$$\frac{\partial u}{\partial t}+u\frac{\partial u}{\partial x}+v\frac{\partial u}{\partial y}+w\frac{\partial u}{\partial z}=-\frac{1}{\rho}\frac{\partial p}{\partial x}+\frac{\partial}{\partial x}\left(A_m\frac{\partial u}{\partial x}\right)+\frac{\partial}{\partial y}\left(A_m\frac{\partial u}{\partial y}\right)+\frac{\partial}{\partial z}\left(K_m\frac{\partial u}{\partial z}\right) \tag{A.2}$$

$$\frac{\partial v}{\partial t}+u\frac{\partial v}{\partial x}+v\frac{\partial v}{\partial y}+w\frac{\partial v}{\partial z}=-\frac{1}{\rho}\frac{\partial p}{\partial y}+\frac{\partial}{\partial x}\left(A_m\frac{\partial v}{\partial x}\right)+\frac{\partial}{\partial y}\left(A_m\frac{\partial v}{\partial y}\right)+\frac{\partial}{\partial z}\left(K_m\frac{\partial v}{\partial z}\right) \quad \text{(A.3)}$$

The vertical momentum equation is reduced to

$$-\frac{1}{\rho}\frac{\partial p}{\partial z}-g=0 \quad \text{(A.3)}$$

where t is time, ρ is the density of water, p is pressure, A_m and K_m are coefficients for turbulent momentum mixing in the horizontal and vertical, respectively, and g is the gravitational acceleration. The following key assumptions and approximations have been made in the above model equations: (a) The fluid is incompressible; (b) the pressure distribution is hydrostatic; (c) the effects of turbulent motions on momentum mixing are parameterised through the use of mixing coefficients.

The coefficient K_m is obtained by appealing to a second order turbulence closure scheme (Mellor and Yamada, 1982); the coefficient is expressed in terms of turbulence kinetic energy $q^2/2$, a turbulence macro-scale l and a stability function S_M as

$$K_m = lqS_M \quad \text{(A.4)}$$

In the horizontal, all of the motions not directly resolved by the model grid are parameterised through the coefficient A_m. This coefficient is calculated from the scheme suggested by Smagorinsky (1963)

$$A_m = (C_s\Delta x\Delta y)\sqrt{(\partial u/\partial x)^2+(\partial v/\partial y)^2+0.5(\partial u/\partial y+\partial v/\partial x)^2} \quad \text{(A.5)}$$

where C_s is a constant in the range of $0.1 \le C_s \le 0.24$, and □□is the grid resolution.

At the free surface z = η(x, y) and dune surface z = - H(x, y), kinematic boundary conditions are given as

$$w = u\frac{\partial \eta}{\partial x} + v\frac{\partial \eta}{\partial y} + \frac{\partial \eta}{\partial t} \tag{A.6}$$

$$w = u\frac{\partial H}{\partial x} + v\frac{\partial H}{\partial y} \tag{A.7}$$

At the dune surface, the dynamic condition is specified as

$$\left(\tau_{bx}, \tau_{by}\right) = \rho\left[\kappa^2 / \ln^2\left(0.5\Delta h_b / z_\circ\right)\right]\sqrt{u_b^2 + v_b^2}\left(u_b, v_b\right) \tag{A.8}$$

where (u_b, v_b) are the (x, y) components of the bottom layer velocity, (τ_{bx}, τ_{by}) are the corresponding components of the bed shear stress, κ is the von Karman constant ($\kappa = 0.41$), Δh_b is the bottom layer thickness, and z_o is related to the size of the roughness elements of the dune surface.

The model equations and relationships are transformed into the σ coordinate in the vertical. The σ coordinate is defined as

$$\sigma = \frac{z - \eta}{H + \eta} \tag{A.9}$$

The advantage is that the free surface (σ = 0) and dune surface (σ = -1) become coordinate planes. The water column is divided into multiple layers. For the k'th layer, the layer-averaged velocities in x and y directions are defined as

$$\bar{u} = (\sigma_{k+1} - \sigma_k)^{-1}\int_{\sigma_k}^{\sigma_{k+1}} u d\sigma \tag{A.10}$$

$$\bar{v} = (\sigma_{k+1} - \sigma_k)^{-1}\int_{\sigma_k}^{\sigma_{k+1}} v d\sigma \tag{A.11}$$

Governing equations for the layer-averaged velocities are derived from the transformed continuity and momentum equations and are solved using the finite difference techniques of second order accuracy. For more details about model formulations, refer to HydroQual (2002).

Appendix B

Field measurement of ice-covered river flow

During the winter period of 1989 to 1990, four Water Survey Canada participated in the field data collection activities. Twenty six river sites were selected in the first year of operation (Walker and Wang, 1997). Velocity profiles were measured approximately once every three to four weeks. From 1989 to 1990, a total of 1539 vertical velocity profiles were obtained (Walker and Wang, 1997).

The flow measurements from the ice-covered river stations were the first set of measurements in Canadian hydrometric history. The instruments used for the profile measurements were conventional Water Survey Canada-style Price winter meters equipped with metallic rotors. The penta counters were removed to reduce frictional

resistance at low velocity (Walker and Wang, 1997). These meters were used in combination with winter rods or standard winter weights. The current meters were calibrated individually in a towing tank with the same suspension assembly as used in the field. The meters were heated between each vertical to ensure that the ice did not adhere to the metre, particularly the pivot (Hoque, 2009).

The measured velocity profiles are continuous, but not always differentiable at certain positions where there is a sudden change in flow velocity.